Republic of Iraq
Ministry of Higher Education and Scientific Research
University of Babylon- College of Science
Department of Physics

Influence of $BaTiO_3$ Nanoparticles on Some Physical Properties of Poly Blend for Piezoelectric and Medical Applications

A Thesis
Submitted to the Council of the College of Science, University of Babylon in Partial Fulfillment of the Requirements for the Degree of Doctorate of Philosophy of Science in Physics

By

Falah Hassoon Oraibi Abdullah

B.Sc. in Physics / 1993

M.Sc. in Physics / 2007

Supervised by

Prof. Dr.

Raheem Gaayid Kadhim Hussein

2022 A.D. **1443 A.H.**

جمهورية العراق
وزارة التعليم العالي والبحث العلمي
جامعة بابل ـ كلية العلوم
قسم الفيزياء

تأثير جسيمات $BaTiO_3$ النانوية على بعض الخواص الفيزيائية لمزيج البوليمر لتطبيقات الكهرباء الضغطية والطبية

أطروحة
مقدمة إلى مجلس كلية العلوم في جامعة بابل
وهي جزء من متطلبات نيل درجة دكتوراه فلسفة في العلوم / الفيزياء

من قبل

فلاح حسون عريبي عبد الله

بكالوريوس علوم في الفيزياء / 1993
ماجستير علوم في الفيزياء / 2007

بإشراف

الاستاذ الدكتور

رحيم كعيد كاظم حسين

1443 هـ 2022 م

﴿قَالُوْا سُبْحَانَكَ لاَ عِلْمَ لَنَا إِلاَّ مَا
عَلَّمْتَنَا إِنَّكَ أَنْتَ العَلِيْمُ الْحَكِيْمُ﴾

صدق الله العظيم

سورة البقرة (الآية ٣٢)

Contents

Contents

Contents

Examining Committee Certification

We certify that we have read this thesis entitled **(Influence of $BaTiO_3$ Nanoparticles on Some Physical Properties of Poly Blend for Piezoelectric and Medical Applications)** and in our opinion as an examining committee examined the Ph.D. student **" Falah Hassoon Oraibi Abdullah "** in the contents, it is adequate with **(Excellent)** as a thesis meets the standard for the Degree of Doctorate of Philosophy in Physics.

Signature:
Name: **Dr. Mohammed Hadi Shinen**
Title: Professor
Address: University of Babylon-College of Science-Department of Physics.
Date: / / 2022
(Chairman)

Signature:
Name: **Dr. Kareema Majeed Zaidan**
Title: Professor
Address: University of Basrah -College of Science-Department of Physics.
Date: / / 2022
(Member)

Signature:
Name: **Dr. Musa Kadhim Mohsin**
Title: Assistant Professor
Address: University of Babylon-College of Science-Department of Physics.
Date: / / 2022
(Member)

Signature:
Name: **Dr. Abdulhussain Abbas Khadayeir**
Title: Assistant Professor
Address: University of Al-Qadisiyah-College of Education-Department of Physics.
Date: / / 2022
(Member)

Signature:
Name: **Dr. Aref Saleh Baron**
Title: Assistant Professor
Address: University of Kufa -College of Science-Department of Physics.
Date: / / 2022
(Member)

Signature:
Name: **Dr. Raheem Gaayid Kadhim Hussein**
Title: Professor
Address: University of Babylon-College of Science-Department of Physics.
Date: / / 2022
(Member and Supervisor)

Approved by the College of Science Committee on Graduate Studies.

Signature:
Name: **Dr. Enas M. Al-Robayi**
Title: Professor
Address: Dean of the College of Science-University of Babylon.
Date: / / 2022

List of Abbreviations

Abbreviation	Description
eV	Electron Volt.
MPa	Mega Pascal.
PS	Polystyrene.
PMMA	Poly Methyl Methacrylate.
$BaTiO_3$	Barium Titanate.
BT	Barium Titanate.
ABO_3	Generic composition of the perovskite.
SEM	Scanning Electron Microscope.
TEM	Transmission Electron Microscope.
NPs	Nanoparticles.
FESEM	Field Emission Scanning Electron Microscope.
FTIR	Fourier Transform Infrared Spectroscopy.
XRD	X-Ray Diffraction.
FWHM	Full Width at Half Maximum.
A.C	Alternative Current.
LCR meter	Inductance, Capacitance, and Resistance of an electronic component.
WAT	Weak Absorption Tail.
VB	Valance Band.
CB	Conduction Band.
ROS	Reactive Oxygen Species.
CAC	Chemical Analysis Center.
UV	Ultraviolet Light.
Vis	Visible Light.
MHA	Mueller Hinton Agar.
CFU	Colony Forming Units.
JCPDS	Joint Committee on Powder Diffraction Standards.
(hkl)	Miller Indices.
CPS	Counts per Second.
wt.%	Weight Percent.
S. aureus	Staphylococcus aureus.
E. faecalis	Enterococcus faecalis.
E. cloacae	Enterobacter cloacae.
E. coli	Escherichia coli.
mL	Milliliter.

List of Figures

List of Figures

List of Figures

List of Figures

List of Symbols

Symbol	Description	Unit
A	Absorbance.	-
B	Proportionality constant.	-
C_p	Parallel capacitance.	F
$C_\circ$	Vacuum capacitance.	F
c	Light speed in space ($3x10^8$).	m/s
D_m	Electric displacement.	C/m^2
d	Interplaner spacing.	nm
d_{mi}^T	Matrix constant for the direct piezoelectric effect.	C/N
E_g	Band gap energy.	eV
E_k	Electric field.	$V/m\ ,N/C$
$E_\circ$	Optical band gap energy.	eV
H	Cross sectional area.	cm^2, m^2
h	Planck constant ($6.626x10^{-34}$).	$J.s$
I_A	Absorbed light intensity.	W/m^2
$I_\circ$	Incident light intensity.	W/m^2
I_T	Transmitted light intensity.	W/m^2
I_R	Reflected light intensity.	W/m^2
K	Extinction coefficient.	-
m	Matrix transposition.	-
n	Refractive index.	-
n^*	Complex refractive index.	-
R	Reflectance.	-
r	Exponent value and denotes electronic transition nature.	-
S_i	Strain.	-
T	Transmittance.	-
T_{ij}	Stress.	N/m^2
t	Thickness.	nm
v	Light speed inside the material.	m/s
Y	Electromechanical coupling factor.	-
Z	Particle size (crystallite size).	nm
Å	Angstrom.	$cm\ ,m\ ,nm\ ,pm$
θ	Incident angle.	$degree$

List of Symbols

Symbol	Description	Unit
λ	Wavelength.	nm
β	Full width at half maximum of most stronger peak (highest intensity peak).	$radians$
$\varepsilon_\circ, \epsilon_\circ$	Constant of permittivity for free space ($8.85x10^{-12}$).	F/m
$tan\delta$	Loss tangent.	-
$\sigma_{a.c}$	A.C Electrical conductivity.	$(\Omega.cm)^{-1}$
ω	Angular frequency.	rad/s
α	Absorption coefficient.	cm^{-1}
ε	Dielectric constant.	-
ε_r	Real part of the dielectric constant.	-
ε_i	Imaginary part of the dielectric constant.	-
ν	Frequency.	s^{-1}, Hz
σ_{opt}	Optical conductivity.	$(\Omega.cm)^{-1}$
ϵ_{mk}^{T}	Matrix of dielectric permittivity under conditions of constant mechanical stress.	F/m
$\hbar\omega$	Photon energy.	eV

List of Tables

Summary

In this study, (Polystyrene: Poly methyl methacrylate)/Barium titanate nanocomposite blend films have been prepared by solution casting technique. These are prepared for (30:70) weight ratio for (PS:PMMA)poly blend, then different ratios (3,6,9,12)% of $BaTiO_3$ nanoparticles were added to (PS:PMMA)poly blend. The influence of $BaTiO_3$ nanoparticles additive on structural, A.C electrical, and optical properties of (PS:PMMA)poly blend have been studied. Piezoelectric and antibacterial activity applications have been investigated.

Optical microscope and field emission scanning electron microscope images indicate that the nanoparticles additives distribution was homogeneous in the poly blend. Fourier transform infrared spectrums indicate that no change on chemical structures between the poly blend and the nanoparticles additives. X-ray diffraction patterns indicate that the poly blend film is amorphous structure, while nanocomposite blend films is polycrystalline structure.

A.C Electrical properties of the nanocomposite blend films studied in frequency range (100Hz-5MHz) at room temperature. The experimental results showed that the dielectric constant, dielectric loss, and A.C electrical conductivity of (PS:PMMA) poly blend film increases with increasing of $BaTiO_3$ nanoparticles additives weight ratio. Dielectric constant and dielectric loss of (PS:PMMA)/$BaTiO_3$ nanocomposite blend films decreases with increasing of frequency of applied electric field, while A.C electrical conductivity increases with increasing of frequency of applied electric field.

Experimental results of the optical properties for (PS:PMMA)/$BaTiO_3$ nanocomposite blend films showed that the absorbance, reflectance, absorption coefficient, extinction coefficient, refractive index, real and imaginary part of dielectric constant, and optical conductivity of (PS:PMMA) poly blend film increases with increasing of $BaTiO_3$ nanoparticles additives weight ratio, while the transmittance and energy gap

for indirect transition (allowed and forbidden) decreases with increasing of $BaTiO_3$ nanoparticles additives weight ratio.

The results of application for (PS:PMMA)/$BaTiO_3$ nanocomposite blend films as piezoelectric material showed that the electrical resistance decreases with increasing of $BaTiO_3$ nanoparticles additives weight ratio and applied load. As a result, pressure sensor have high sensitivity for mechanical stress.

The antibacterial activity for (PS:PMMA)/$BaTiO_3$ nanocomposite blend films have been tested against pathogen (Staphylococcus aureus and Enterococcus faecalis as gram positive bacteria, Enterobacter cloacae and Escherichia coli as gram negative bacteria). The results showed that the inhibition zone diameter increases with increasing of $BaTiO_3$ nanoparticles additives weight ratio, and the gram positive bacteria have greater resistance to these nanoparticles compared to gram negative bacteria.

الخلاصة

في هذه الدراسة، تم تحضير أغشية مزيج المتراكب النانوي (بولي ستايرين : بولي مثيل ميثاكريلايت)/ تيتانات الباريوم بتقنية صب المحلول. تم تحضيرها لنسبة وزن (30:70) لمزيج البوليمر (PS:PMMA)، ثم أضيفت نسب مختلفة % (3,6,9,12) من جسيمات $BaTiO_3$ النانوية الى مزيج البوليمر (PS:PMMA). تمت دراسة تأثير جسيمات $BaTiO_3$ النانوية المضافة على الخواص التركيبية، الكهربائية المتناوبة، والبصرية لمزيج البوليمر (PS:PMMA). تم بحث تطبيقات الكهروضغطية والنشاط المضاد للبكتيريا .

تشير صور المجهر الضوئي والمجهر الالكتروني الماسح انبعاث المجال الى ان توزيع الجسيمات النانوية المضافة كان متجانس في مزيج البوليمر. تشير أطياف تحويلات فورير للأشعة تحت الحمراء إلى عدم وجود تغيير على التراكيب الكيميائية بين مزيج البوليمر والجسيمات النانوية المضافة. يشير نماذج حيود الأشعة السينية إلى أن غشاء مزيج البوليمر (PS:PMMA) هو تركيب عشوائي، بينما أغشية مزيج المتراكب النانوي $(PS:PMMA)/BaTiO_3$ هو تركيب متعدد البلورات .

تمت دراسة الخواص الكهربائية المتناوبة لأغشية مزيج المتراكب النانوي في مدى تردد (100Hz–5MHz) عند درجة حرارة الغرفة. أظهرت النتائج العملية أن ثابت العزل، الفقدان العزلي، والتوصيلية الكهربائية المتناوبة لغشاء مزيج البوليمر (PS:PMMA) تتزايد مع زيادة نسبة وزن جسيمات $BaTiO_3$ النانوية المضافة. يتناقص ثابت العزل والفقدان العزلي لأغشية مزيج المتراكب النانوي $(PS:PMMA)/BaTiO_3$ مع زيادة تردد المجال الكهربائي المطبق، بينما تتزايد التوصيلية الكهربائية المتناوبة مع زيادة تردد المجال الكهربائي المطبق.

أظهرت النتائج العملية للخواص البصرية لأغشية مزيج المتراكب النانوي $(PS:PMMA)/BaTiO_3$ أن الامتصاصية، الانعكاسية، معامل الامتصاص، معامل الخمود، معامل الانكسار، الجزء الحقيقي والخيالي لثابت العزل، والتوصيلية البصرية لغشاء مزيج البوليمر (PS:PMMA) تتزايد مع زيادة نسبة وزن جسيمات $BaTiO_3$ النانوية المضافة، بينما تتناقص النفاذية وفجوة الطاقة للانتقال غير المباشر (المسموح والممنوع) مع زيادة نسبة وزن جسيمات $BaTiO_3$ النانوية المضافة.

أظهرت نتائج تطبيق أغشية مزيج المتراكب النانوي $(PS:PMMA)/BaTiO_3$ كمادة كهروضغطية أن المقاومة الكهربائية تتناقص مع زيادة نسبة وزن جسيمات $BaTiO_3$ النانوية المضافة والحمل المطبق. نتيجة لذلك ، متحسس الضغط له حساسية عالية للإجهاد الميكانيكي .

تم اختبار النشاط المضاد للبكتيريا لأغشية مزيج المتراكب النانوي $(PS:PMMA)/BaTiO_3$ ضد العوامل الممرضة (Staphylococcus aureus و Enterococcus faecalis كبكتيريا

الخلاصة

موجبة الغرام ، Enterobacter cloacae و Escherichia coli كبكتيريا سالبة الغرام) . أظهرت النتائج أن قطر منطقة التثبيط يتزايد مع زيادة نسبة وزن جسيمات $BaTiO_3$ النانوية المضافة، وأن البكتيريا موجبة الغرام لديها مقاومة أكبر لهذه الجسيمات النانوية مقارنة بالبكتيريا سالبة الغرام .

1.1 Introduction

Concept of nanoscience as their applied as antibacterial effect leads to researches have introduced momentum by providing advanced solutions in many fields as materials science, biomedical, electronics, and optics. Nanoscience is the science that deals with the measurement at the nanoscale. Nanotechnology and nanoscience are including ability to control the movement of atoms and molecules to form substances, composites, components and devices at the nanoscale.

The scientists are concluded that materials at small size, small particles and thin films can have different properties as compared with the same materials at larger size. For example, silver can be consider nontoxic, but when convert it to nanoparticles become killing viruses if contacts with them. In addition to; characterizes like color, electrical conductivity and strength various when material becomes nanosized. For example, metal can become an insulator or a semiconductor when it converts to the nanoscale level [1]. By understanding these different the infinite promises for improved structures, devices and materials.

Nanomaterial can be used for several reasons as tiny size, light weight and strong. The major important points in nanotechnology are:

1. Small size, usually equal or less than 100 of nanometers.
2. Due to small size it gets unique characterizations.
3. The structure and composition in the (nm) scale can be controlled of them hence control the properties [2].

By developing in the nanoscience and nanotechnology in materials, nanomaterials can be contain one dimension or more in nanoscale have new characterizes which different in structure and chemistry with normal materials have wide attention in the researches field [3]. Nanomaterials can be classified according to dimensions to:

1.Three dimensions as nanoparticles, nanoshells and quantum dots.

2.Two dimensions as fibers, nanotube, nanorode and nanowire.

3.One dimensions as thin films, coating and layers.

There are two types of nanomaterials, naturally and industrial nanomaterials. The naturally nanomaterials are found in environment without human intervention as viruses, proteins, DNA molecules, and nanoparticles were generated from volcanoes explosion.

The industrial nanomaterials are fabricated by human and without intention as nanoparticles were generated during diesel burning [1].

1.2 Polymers

A polymer is a large molecule, or macromolecule, composed of many repeated subunits. Because of their broad range of properties, both synthetic and natural polymers play an essential and ubiquitous role in everyday life. Polymers range from familiar synthetic plastics such as polystyrene to natural biopolymers such as DNA and proteins that are fundamental to biological structure and function. Polymers, both natural and synthetic, are created via polymerization of many small molecules, known as monomers. Their consequently large molecular mass relative to small molecule compounds produces unique physical properties, including toughness, viscoelasticity, and a tendency to form glasses and semi crystalline structures rather than crystals [4].

We can find polymers as components of many of the objects that surround us, as well as in a broad diversity of applications in daily life: clothing, shoes, personal care products, furniture, electrical and electronic appliances, packaging, utensils, automobile parts, coatings, paints, adhesives, tires, and so on. The list is endless, and these few examples should provide an idea of the importance of synthetic polymers to modern society, in terms of both their usefulness and the economic value that they represent [5].

1.3 Classification of Polymer

Polymers passes different chemical structure, physical properties, mechanical behavior, thermal characteristics etc., and on the basis of properties of polymer it is being classified in different way [6] as shown in Table (1.1).

Table (1.1): Classification of polymer [6].

No.	Basis of Classification	Polymer Type
1	Origin	Natural, Semi synthetic, Synthetic
2	Thermal Response	Thermoplastic, Thermosetting
3	Mode of formation	Addition, Condensation
4	Line structure	Linear, Branched, Crosslinked
5	Application and physical Properties	Rubber, Plastic, Fibers
6	Tacticity	Isotactic, Syndiotactic, Atactic
7	Crystallinity	Non crystalline (amorphous), Semi crystalline, Crystalline

1.4 Polystyrene (PS)

Polystyrene (PS) is a synthetic aromatic polymer made from the monomer styrene with the help of a process called polymerization. Polymerization is a process where monomers are joined with each other in order to make long molecular chains called polymer, is called polymerization [7] as shown in Figure (1.1).

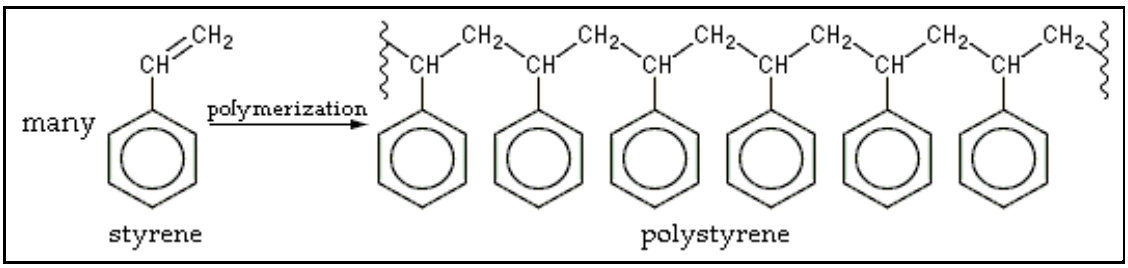

Figure (1.1): Styrene polymerization process [7].

The physical properties of PS are due to the presence of weak van der Waals forces between the chains of polymer. The forces weaken when

heated and the chains glide past one another. Because of that, PS is highly elastic and softens when heated beyond its glass transition temperature. PS is solid in normal temperature, but it turns into liquid form when heated above glass transition temperature. This liquid form can be used easily for molding [7]. The advantages and disadvantages of PS are shown in Table (1.2).

Table (1.2): Advantages and disadvantages of PS [7].

No.	Advantages	Disadvantages
1	Hard and stiff	Brittle
2	Excellent insulation properties	Poor thermal resistant
3	Inexpensive	Poor solvent resistant
4	Food contact acceptable	Flammable
5	Good processability	Subject to stress and environmental cracking
6	Light weight	
7	Water resistant	

PS is designed for applications demanding excellent mechanical and electrical properties. Because of that PS has an enormous variety of applications. It is widely used in home appliances, protective packaging, toys, food industry, construction industry, medical equipment, electronics and automobile industry etc. [7]. PS properties are shown in Table (1.3).

Table (1.3): Properties of PS [8].

No.	Property	Value
1	Band gap	4.6 eV
2	Dielectric constant (ε)	(2.49-2.55) at 1kHz
3	Resistivity	(10^{20}-10^{22}) Ω.cm
4	Density	(1.04-1.065) g/cm^3
5	Glass transition temperature (T_g)	(80-90)˚C
6	Heat capacity (C_p)	1.185 kJ/kg.K at 0˚C
7	Melting temperature (T_m)	240˚C
8	Refractive index (n_D)	(1.59-1.60) at λ = 589.3nm
9	Compressibility	220x10^{-6} MPa^{-1}
10	Solubility parameter (δ)	(8.5-10.3) (cal/cm^3)$^{1/2}$

1.5 Poly Methyl Methacrylate (PMMA)

This material was developed in 1928 in various laboratories, and was first brought to market in 1933 by Rohm and Haas company, under the trademark Plexiglas. Chemically, it is a vinyl polymer, made by free radical vinyl polymerization from the MMA monomer [9] as shown in Figure (1.2).

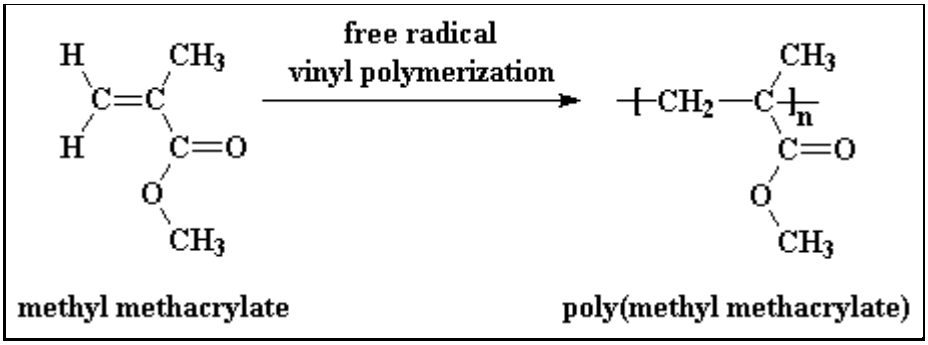

Figure (1.2): Methyl methacrylate polymerization process [9].

Acrylic plastic or poly methyl methacrylate (PMMA) is widely used in many applications because of its physical and mechanical properties such as high optical transmission (92% light transmission) in the infrared and visible ranges from 380 to 780 nm, toughness, easy thermoforming and good stability. PMMA is frequently used as a light or shatter resistant alternative to glass. The reflection angle on an internal surface is 41˚ to 42˚ which can be used for making light conductors and fiber optic filaments. Its refractive index is 1.49 which is suitable for manufacturing optical products [9]. The advantages and disadvantages of PMMA are shown in Table (1.4).

Table (1.4): Advantages and disadvantages of PMMA[10].

No.	Advantages	Disadvantages
1	High mechanical strength and hardness	Possible stress problems
2	High rigidity	Low chemical resistance
3	Excellent transparency	Low impact resistance
4	Easy to polish	Brittle
5	Good thermal stability	
6	Good insulation properties	
7	Low water absorption	
8	Excellent weather resistance	

PMMA is used in the exterior lenses of automobiles and trucks. The spectator protection shield in ice hockey stadiums is made of PMMA. The windows of many aircraft and windows of police vehicles for riot control are PMMA as are many motorcycle helmet visors. PMMA is also used in medicine. PMMA has good compatibility with human tissue and has been used for replacement of intraocular lenses in eyes. Hard contact lenses are often composed of PMMA. Bone cement containing PMMA is used to connect bond implants and remodel lost bone. PMMA has Young's modulus near that of bone, so does a good job of load sharing with the native bone. Dentures are often PMMA [11]. PMMA properties are shown in Table (1.5).

Table (1.5): Properties of PMMA[8].

No.	Property	Value
1	Band gap	4.273 eV
2	Dielectric constant (ε)	3 at 1kHz
3	Resistivity	$> 10^{15}$ Ω.cm
4	Density	1.19 g/cm^3
5	Glass transition temperature (T_g)	(104-105)˚C
6	Heat capacity (C_p)	1.255 kJ/kg.K at 0˚C
7	Melting temperature (T_m)	130˚C
8	Refractive index (n_D)	1.492 at λ = 589nm
9	Compressibility	245x10^{-6} MPa^{-1}
10	Solubility parameter (δ)	(8.5-13.3) (cal/cm^3)$^{1/2}$

1.6 Barium Titanate ($BaTiO_3$)

Barium titanate ($BaTiO_3$) adopts a tetragonal crystal structure when below the ferroelectric Curie temperature (130˚C for pure $BaTiO_3$), this structure possesses a non-centrosymmetric crystal structure and is one of the most extensively researched perovskite materials to date. It has excellent ferroelectric properties, high dielectric susceptibility and is used in a large variety of applications; the most common being multilayer ceramic capacitors. There is a demand to make thinner layers in micro-capacitors and

therefore smaller particles of $BaTiO_3$ are required. However a problem associated with the size reduction of $BaTiO_3$ is that the paraelectric cubic phase (centrosymmetric crystal structure) becomes more stable than the tetragonal phase (even below the Curie temperature) leading to inferior dielectric properties where the ferroelectric tetragonal core becomes less dominant in terms of total particle volume, and the paraelectric cubic surface shell ultimately dominates at and below a critical size. As the particle size decreases, naturally the bulk dipole interaction decreases and consequently disorder will eventually dominate the bulk [12] as shown in Figure (1.3).

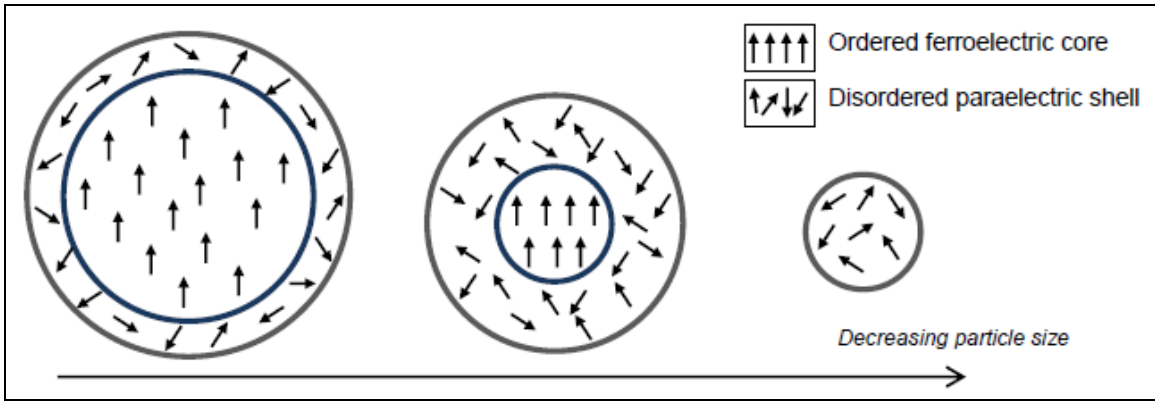

Figure (1.3): Schematic of $BaTiO_3$ NP as a function of decreasing particle size [12].

In order for a material to be ferroelectric there must be a net (electrostatic) dipole moment within the material. In the case of tetragonal $BaTiO_3$ a noncentrosymmetric crystal medium the net dipoles are formed by the titanium atom in the oxygen octahedron being displaced from the center of the unit cell [12].

A perovskite is a common class of crystalline structures for ferroelectric materials. It has a generic composition of ABO_3 ideally showing a body centered cubic structure as shown in Figure (1.4a) highlighting 8(A) cations (in the corners) a single (B) cation in the unit cell center, with oxygen (or other anions) atoms present in the center of each of the faces (ABO_3). The unit cell structure in Figure (1.4a) has the potential to be ferroelectric if, when the unit cell is repeated - there is a spontaneous net electrostatic dipole

moment within the material that can be reversed upon the application of an electric field. In the case of $BaTiO_3$ and $Ba_{1-x}Sr_xTiO_3$, the net dipoles are formed by the titanium atom being displaced in the oxygen octahedron as shown in Figure (1.4b), typically transforming to a tetragonal crystal structure [12].

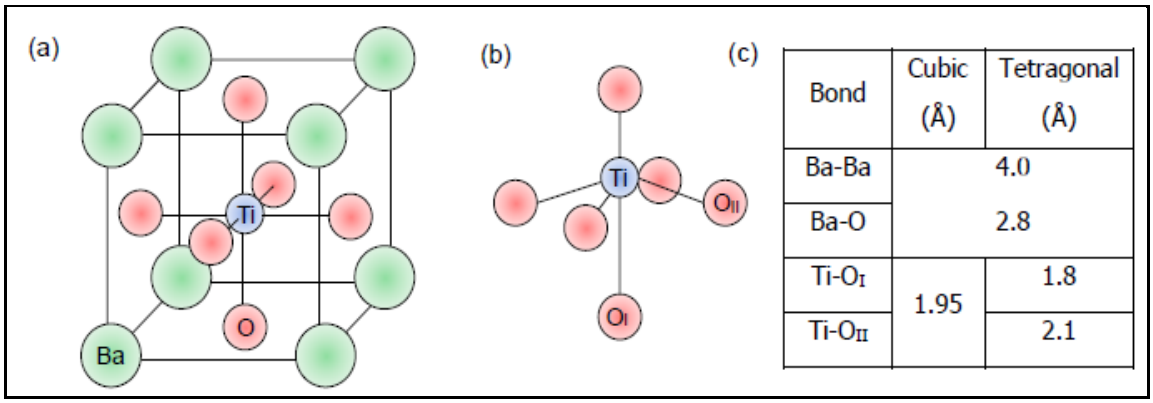

Bond	Cubic (Å)	Tetragonal (Å)
Ba-Ba	4.0	
Ba-O	2.8	
$Ti-O_I$	1.95	1.8
$Ti-O_{II}$		2.1

Figure (1.4): (a) the unit cell of an $BaTiO_3$ (b) in the case of tetragonal $BaTiO_3$ titanium atom is displaced in the oxygen octahedron, giving rise to a net polarization and a transformation in crystalline structure (c) list of bond lengths for cubic and tetragonal $BaTiO_3$ symmetry [12].

The net dipole moment forms when the material cools through the Curie temperature. The Curie temperature for $BaTiO_3$ is 130˚C, above this transition Curie temperature the perovskite unit cell is cubic and below it is typically tetragonal (although it can be orthorhombic or rhombohedral at lower temperatures) as shown in Figure (1.5). It is generally accepted that cubic unit cells are paraelectric (i.e. no net spontaneous polarization) whereas tetragonal unit cells are known to be ferroelectric [12]. $BaTiO_3$ properties are shown in Table (1.6).

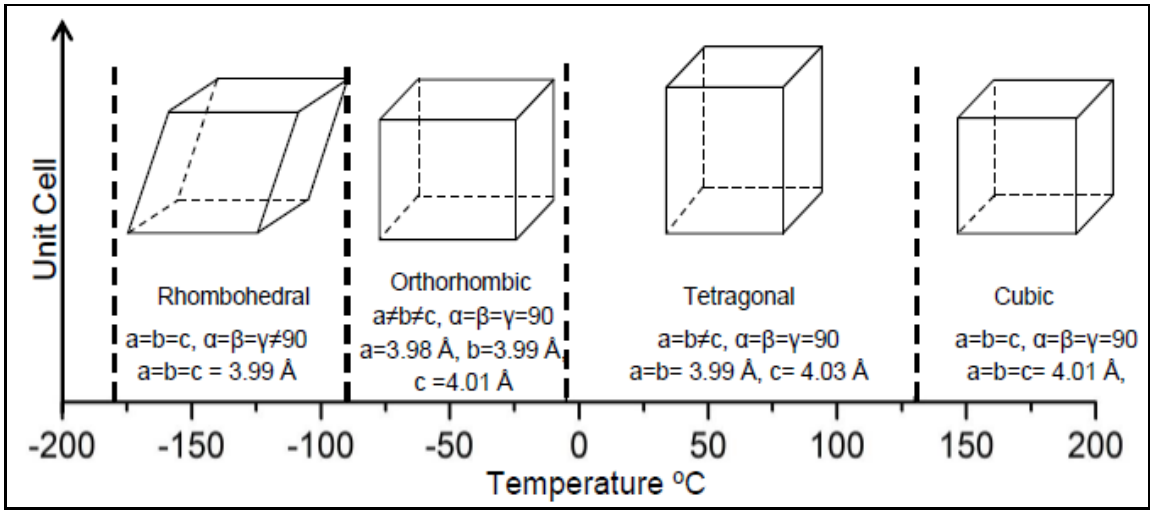

Figure (1.5): The phase transitions of $BaTiO_3$ when cooled through the Curie temperature (130˚C) [12].

Table (1.6): Properties of $BaTiO_3$ [13,14].

No.	Property	Value
1	Band gap	3.2 eV at 300 K [13]
2	Unit Cell Dimensions	Cubic (120˚C): a = 3.996Å Tetragonal (20˚C): a = 3.9920Å, c = 4.0361Å Orthorhombic (-10˚C): a = 3.990Å, b = 5.669Å, c = 5.682Å Rhombohedral (-168˚C): a = 4.001Å, α = 89˚51' [13]
3	Density	$6.02x10^3$ kg/m^3 (20˚C) [13]
4	Spontaneous Polarization (P_S)	Tetragonal (25˚C): P_S = (0.25-0.26) C/m^2 Orthorhombic (0˚C): $P_S \approx 0.21$ C/m^2 Rhombohedral(-100˚C): $P_S \approx 0.19$ C/m^2 [13]
5	Melting temperature	1625˚C [13]
6	Refractive index	2.4 [13]
7	Dielectric constant	5194 at T_C = 110˚C and 1kHz 5072 at T_C = 110˚C and 10kHz 4880 at T_C = 110˚C and 100kHz [14]

1.7 Literature Review

There are many applications for nanocomposites as medical and industrial applications. So, the structural, electrical and optical properties were studied by many researchers, to know the advantages for their applications.

In 2008, **N. Bouropoulos et al.**[15] prepared nanocomposites of polyvinyl alcohol and ZnO using the solution casting method. ZnO nanoparticles with hexagonal wurtzite structure and mean sizes of 59, 82 and 150 nm were prepared by thermal decomposition of zinc acetate dihydrate. The synthesized crystals were characterized by X-ray diffraction (XRD), and scanning electron microscopy (SEM). Optical properties of the nanocomposites were determined using UV-Visible absorption spectroscopy. The results showed that all samples appeared near band edge absorption close to the bulk value. Dielectric data provide evidence that interfacial polarization, which is present in all three nanocomposite films, shifts to higher frequencies and its intensity is decreasing as the mean nanoparticle diameter is also decreasing.

In 2011, **K. Vimala et al.**[16] fabricated chitosan-poly(vinyl alcohol)-silver (Cs-PVA-Ag) nanocomposite films in view of their increasing applications as antimicrobial packaging, wound dressing and antibacterial materials. The reduction of silver ions into silver nanoparticles (Ag NPs) is achieved in acidic solution of (Cs) and (PVA) using their functional groups (-OH,-COOH, $-NH_2$ groups). The presence of Ag NPs in the (Cs-PVA) film is confirmed by UV-Vis spectroscopy, FTIR spectroscopy and XRD analysis. SEM images illustrate the presence of embedded Ag NPs throughout the films. In addition, the formed Ag NPs have an average particle size of ~ 16.5nm as observed by transmission electron microscope (TEM). The antimicrobial and antifungal activity of the (Cs-PVA-Ag) nanocomposite films have demonstrated significant effects against

Escherichia coli (E.coli), Pseudomonas, Staphylococcus, Micrococcus, Candida albicans, and Pseudomonas aeruginosa. To improve further their therapeutic efficacy as antimicrobial agents, curcumin encapsulated (Cs-PVA-Ag) nanocomposite films are developed which showed enormous growth inhibition of E.coli compared to curcumin and (Cs-PVA-Ag) nanocomposite film alone. Therefore, the present study clearly provides novel antimicrobial films which are potentially useful in preventing/treating infections.

In 2011, **J. Q. Qi et al.**[17] synthesized large quantity of tetragonal $BaTiO_3$ nanoparticles as fine as 7 nm at room temperature. The synthesis mechanism of $BaTiO_3$ nanoparticles is believed to undergo two steps, hydrolysis of alkoxide to form titanium hydroxide and followed crystallization of $BaTiO_3$ nanoparticles by adsorption of Ba^{2+}. The synthesis efficiency improved distinctly, and the batch processing could be scaled up easily because large quantity of solvents was not necessary in the method. Both XRD and TEM results revealed that the as prepared nanoparticles had perfect crystallized perovskite phase with ultrafine grain size. Temperature dependent Raman spectrum shows that the nanoparticles prepared from our method have the normal phase transition as bulk $BaTiO_3$ materials and have tetragonal phase at room temperature even when the grain size is as small as 7 nm.

In 2014, **S. Raja et al.**[18] synthesized $BaTiO_3$ NPs at two different calcination temperatures by a simple wet chemical method using barium chloride ($BaCl_2$), titanium dioxide (TiO_2) and oxalic acid as starting materials. The XRD patterns of $BaTiO_3$ NPs calcined at 500˚C showed cubic structure whereas samples calcined at 900˚C showed tetragonal structure. Energy dispersive X-ray spectroscopy (EDX) spectrum revealed the presence of Barium, Titanium and oxide in the sample. SEM and TEM micrographs revealed the presence of spherical and rod shape structure.

Bactericidal effect of $BaTiO_3$ NPs was also tested against the human pathogenic bacteria by disc diffusion method and found to be effective to some extent.

In 2015, **R. G. Kadhim** [19] study the effect of TiO_2 nanoparticles on electrical properties of PMMA. The samples of (PMMA-TiO_2) nanocomposites prepared by using the solution casting technique. TiO_2 wt.% nanoparticles are (0,3,5,7) wt.%. The experimental results show that the dielectric constant, dielectric loss, and the A.C electrical conductivity for (PMMA-TiO_2) nanocomposites are increase with increasing the concentrations of TiO_2 nanoparticles, the dielectric constant and the dielectric loss for (PMMA-TiO_2) nanocomposites decrease with increasing the frequency of the applied electric field, but the A.C electrical conductivity increase with increasing the frequency of the applied electric field.

In 2015, **S. S. Kumbhar et al.**[20] prepared $BaTiO_3$ thin films using the spray pyrolysis method. XRD pattern confirmed the polycrystalline nature of the films with a cubic crystal structure. X-ray photoelectron spectroscopy (XPS) showed a good agreement of the thin films stoichiometry with $BaTiO_3$. A presence of Ba, Ti and O in the $BaTiO_3$ thin films was observed by EDX analysis. SEM images showed the heterogeneous distribution of cubical grains all over the substrate. The dielectric constant and dielectric loss showed the dispersion behavior as a function of frequency, measured in the frequency range (20Hz-1MHz). A.C conductivity (σ_{ac}) measurement showed the linear nature of obtained films.

In 2016, **V. N. Reddy et al.**[21] investigated the structural, optical and ferroelectric properties of $BaTiO_3$ ceramics synthesized via conventional solid state reaction method. The phase purity is evaluated from diffraction studies. The morphology is analyzed by SEM. The diffuse reflectance spectrum (DRS) attributes the direct and indirect optical band gap energies

of $BaTiO_3$. In addition, IR spectrum confirms the presence of metal oxide (M-O) bonds such as Ti-O and Ba-O.

In 2017, **M. Singh et al.**[22] prepared perovskite $BaTiO_3$ nanocomposite thin film using spin coating technique. SEM images showed the macroporous cubic structure of the film. The minimum crystallite size was evaluated as 11 nm by XRD and confirmed by TEM. Band gap of $BaTiO_3$ was evaluated as 3.9 eV. Raman Spectroscopy confirmed the formation of $BaTiO_3$ at 540 cm^{-1}.

In 2019, **G. G. Carbone et al.**[23] developed a colorimetric sensor based on nanoparticles for the detection of hydrogen peroxide. Nanoparticles were made using small sheets of PMMA and silver nitrate. (Ag NP-PMMA) solution proved to be particularly sensitive to hydrogen peroxide compared to other analytes. This sensor provided a quick, practical and easy tool to detect hydrogen peroxide.

In 2019, **D. Hassan, and A. H. Ah-yasari** [24] prepared (PS-CuO) nanocomposites for piezoelectric application. CuO nanoparticles were added to PS by different concentrations are (0,4,8,12) wt.%. The results showed that the dielectric constant and dielectric loss of (PS-CuO) nanocomposites decrease with increasing in frequency. The A.C electrical conductivity increase with increasing in frequency. The dielectric constant, dielectric loss, and A.C electrical conductivity of PS increase with increasing in CuO nanoparticles concentrations. The results of piezoelectric application showed that the electrical resistance of (PS-CuO) nanocomposites decrease with increasing in pressure.

In 2020, **M. F. H. Al-Kadhemy et al.**[25] prepared pure Polycarbonate-Polystyrene (PC-PS) blend and doped blend films with various volume of Coumarin dye by using the solution casting technique. The optical energy gaps of pure PC was 4.24 eV, pure PS was 4.39 eV, Coumarin dye was 4.08 eV, and the pure blend was 4.1 eV. After doping blend with Coumarin dye,

the energy gap was decreased by 0.06 eV in a volume of 12 ml. When the Coumarin dye added to the pure blend with different concentrations (12, 24, 36, 48) ml, the FTIR spectrum affected by the disappearance of peaks and appearance of new ones.

In 2021, **A. A. Bani-Salameh et al.**[26] prepared (PMMA-PS) thin films doped with (1, 3, 5, 7) % of cerium dioxide (CeO_2) nanoparticles. The transmittance and reflectance are measured in the spectral range (250–700) nm. High transmittance of 87% is observed in the low energy regions. The optical band gap energy of (PMMA-PS) thin film is found to be 4.03 eV. FTIR analysis is identify the major vibrational modes of the nanocomposites. The peak at 541.42 cm^{-1} is assigned to Ce-O and indicates the incorporation of CeO_2 nanoparticles into the copolymers matrices. There were drastic changes to the width and intensity of the vibrational bands of PMMA-PS upon addition of CeO_2 nanoparticles.

1.8 The Aims of The Research

The principle aims of this research are:

1.Preparation of (PS:PMMA)/$BaTiO_3$ nanocomposite blend films.

2.Studying the structural, electrical and optical properties of (PS:PMMA)/$BaTiO_3$ nanocomposite blend films.

3.Application of the (PS:PMMA)/$BaTiO_3$ nanocomposite blend films as piezoelectric sensor.

4.Application of the (PS:PMMA)/$BaTiO_3$ nanocomposite blend films as antibacterial effect.

2.1 Introduction

This chapter includes a general description of the physical concepts, scientific clarifications, relationships, laws and technique used in this research work and the structural, electrical and optical properties of the prepared nanocomposite in addition to the piezoelectric and medical applications.

2.2 Poly Blend

A poly blend is defined as a single entity of material containing within its physical boundary at least two thoroughly mixed polymers which are not linked covalently. Although in some literature sources a poly blend is described simply as a physical mixture of two or more polymers, such a broad definition is not practical. Consider mixing polystyrene powder and polyethylene powder in a Waring blender. It will not be useful to call such a mixture a poly blend because there is little one can do with it without first forming it into a single piece. Now consider the definition of alloy. A metallic alloy is not a mixture of two metals or a metal and a non-metal but rather the fusion product thereof. Thus, from these two considerations poly blend should be limited to a single entity of material in its physical state.

In the previous example of polystyrene powder mixed with polyethylene powder; the mixture is not a poly blend, according to this definition, because the whole mixture is not a single entity but a collection of many powdery particles. Within each single particle of this powdery material, the polymer is either polystyrene or polyethylene, so each particle is not a poly blend. If one dissolves the mixture in a solvent and precipitates it into a nonsolvent in a blender, the resulting powdery product is not a poly blend because again the product is not a single entity. Each single particle is a poly blend because it contains within its physical boundary two well-mixed polymers. If these

two powdery mixtures are fused separately into a single piece, each of these two single pieces of material is a poly blend.

If the glass transition temperatures of the polymeric components are known and the glass transition temperature of the poly blend is determined, one of two things can happen. If the poly blend shows two distinct transitions corresponding to the parent polymers, it is incompatible. If the poly blend shows one transition only, the system is compatible. If a poly blend shows glass transition temperatures similar to the parent components, the chains of the parent polymers must be very much within its own kind.

Poly blends can be prepared by four methods : (1) mechanical mixing on rubber mills or extruders, (2) polymerization of one monomer in the presence of another polymer, (3) evaporation or precipitation from mixture of polymer solutions, (4) coagulation of mixture of polymer lattices. Notice that the products from Methods 2, 3, and 4 are not poly blends according to the definition above. They may be in a thoroughly mixed state and not covalently linked, but they have not been formed into a single piece. The forming process, either through solution or fusion, could result in demixing of the components. Frequently, the components of a poly blend have such low affinity for each other that their fusion product will readily break on gentle handling, such as removing it from a press or mold[27].

2.3 Nanoparticle

A nanoparticle is a fundamental component in the fabrication of a nanostructure having dimensions between 1 to 100 nm. Nanoparticles are generally the final products of a series of chemical, physical and biological processes [28].

A nanomaterial (dimension <100 nm) can take many forms such as particle, wire, tubes, rod and sphere. Nanoparticle products generally include metal oxides, quantum dots, silicon dioxide, dendrimers, and some layered structures. In recent years, the development of new nanoparticles has been

growing rapidly. The categories of nanoparticles are nanomaterials, fullerenes, carbon nanotubes (CNTs), nanowires, quantum dots, metallic nanoparticles, carbon black, dendrimers, nanoclays, and nanocrystals [29].

On the basis of size the nanoparticles can be divided into three categories. First type of nanoparticles is spheres which are having all the three dimensions in the nanometer scale. Second type are generally cylindrical tubes which are having two dimensions in the nanometer scale where as one dimension in the micron meter scale. Third type of nanoparticles are having one dimension in the nanometer scale where as two dimensions in the micrometer scale these are called nanoplates [30].

2.4 Nanocomposite

In recent years, the need for new materials are necessary in most industries in our daily lives. So, polymer nanocomposites can be expressed as materials contain a tiny quantities of nanoparticles (fillers) distributed in polymers homogenously with different concentrations. In nanocomposites the distance between neighboring additives as compared with microcomposites are much smaller. Therefore, in nanocomposites the interaction of fillers with polymers is expected to be much more [31,32].

Nanocomposites are a novel fabrication materials refer to a hopeful field in the area of nanoscience. Besides these properties, they show the amazing advantages of structural, electrical, optical, biocompatibility and biodegradability in various industrial, medical, and drug release packaging applications [33].

Inside polymer blend the filler of nanoparticles interaction between them to form molecular bridges for nanocomposites. This is the origin for improved structural, electrical and optical properties of the nanocomposite as related to conventional microcomposites [34]. To control of the properties of the structure relationships of polymer nanocomposites, must understanding of polymer nanocomposites interactions. This is required to

work within the physical, chemical and biological requirements of constraints by industrial and biomedical application [35].

Polymer nanocomposites consists of three major substances are the matrix, reinforcement, and the interfacial region as shown in the Figure (2.1). The last is in charge of incorporation between the matrix and nanofiller [36].

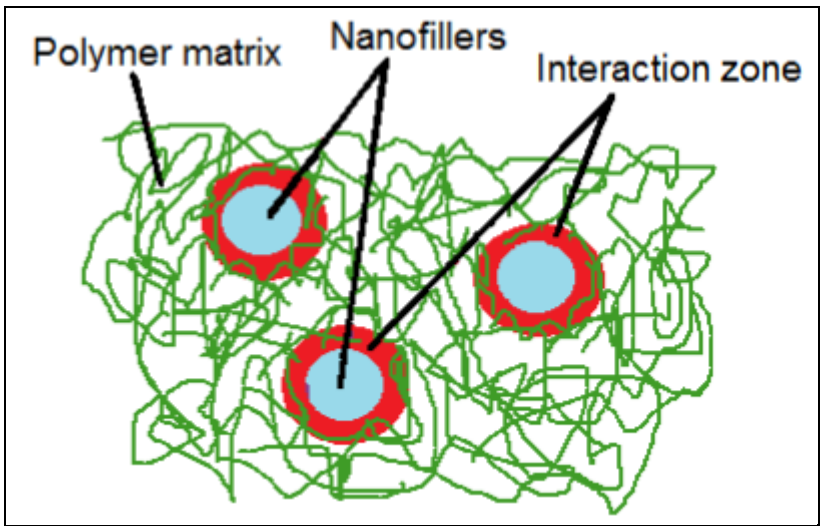

Figure (2.1): The components of polymer nanocomposites [36].

Filler of nanoparticles helps to enhance the foaming properties of polymer. The large surface with compare to volume ratios of the foaming polymer leads to increase the rate of gas and heat release in incident of fire. But with present nanoparticles as zinc oxide, the rate of burning can be mainly reduced [37].

Nanocomposites are classified according to the types of reinforcement materials and matrix materials used in their construction. According to the type of matrix material, nanocomposites are generally classified into following three classes [38]:

1. Polymer matrix nanocomposites.
2. Ceramic matrix nanocomposites.
3. Metal matrix nanocomposites.

Nanocomposites have been growing with a speedy rate so as their large number of applications. In the next 10 years, the worldwide production will exceed 600,000 tons in the following regions [39]:

1. Superior strength fibers and films
2. UV protection gels
3. Drug delivery systems
4. New fire retardant materials
5. Anti-corrosion barrier coatings
6. Lubricant and stretch paints

Nanocomposites have also attracted the field of automotive and industrial applications by doing enhancements in especially the mechanical properties. They can be used or applied in the various vehicles types like engine covers, door covers, and timing belt covers. Other applications are usage as blades for vacuum cleaners, covers for mobile phones, etc. [39].

2.5 Polarization in Materials

Macroscopic objects belong (at least, to a good approximation) to one of two large classes: conductors and insulators (or dielectrics). Conductors are substances that contain an "unlimited" supply of charges that are free to move through the material. In practice what this ordinarily means is that many of the electrons (one or two per atom in a typical metal) are not associated with any particular nucleus, but are free to roam around.

In dielectrics, by contrast, all charges are attached to specific atoms or molecules, and hence, are restricted to limited motions about the specific atoms or molecules. Such microscopic displacements are not dramatic, but their cumulative effects account for the characteristic behaviors of dielectric materials [40].

The polarization occurs in all insulator materials due to lattice defect, molecules and atoms. They contain on the positive and negative charges where in the normal state the centers of their applicable of each other. If

electrical field applied on two parallel plates (capacitor) the insulator located between of them, the positive charges pushed toward the field and negative charges pushed in the opposite direction and thus generated electrical dipoles this is mean the polarization. In other word; the phenomenon of polarization is mean the change in the arrangement of electrically charged particles of a dielectric in space or in the surface charge density in a dielectric [41,42].

Polarization in materials can be due to several mechanisms: electronic (atomic), ionic, molecular (dipole), and interfacial (space-charge) polarization[43-45]. The effect on each mechanism can be seen schematically in Figure (2.2). For a given material, the sum of contributions from each mechanism determines the net polarization, P, of the dielectric material,

$$P = P_{electronic} + P_{ionic} + P_{molecular} + P_{interfacial} \quad (2.1)$$

Electronic polarization exists in all materials and is the response of the electrons and the atomic nuclei that shift their relative positions under an applied electric field and form an electric dipole (each per atom or ion). This polarization occurs instantaneously, in response to light electromagnetic field frequency ($\sim 10^{15}$Hz), since the electrons have a very high natural frequency ($\sim 10^{16}$Hz). Ionic polarization is the displacement of negative and positive ions toward the positive and negative electrodes, respectively. Since they are much more massive than electrons, the ions cannot become polarized as rapidly. Ionic polarization is limited to maximum frequency of approximately 10^{13}Hz. Molecular polarization occurs in materials consisting of polar molecules (or unit cells) only. The maximum frequency of response varies significantly from material to material depending on the size of molecules, but is always less than that for electronic and ionic polarization and is typically less than 10^{10}Hz. Interfacial polarization is a short-range electric conduction process. Due to the nature of diffusion, space charge

polarization occurs rather slowly and the typical frequency of response is approximately 10^2Hz.

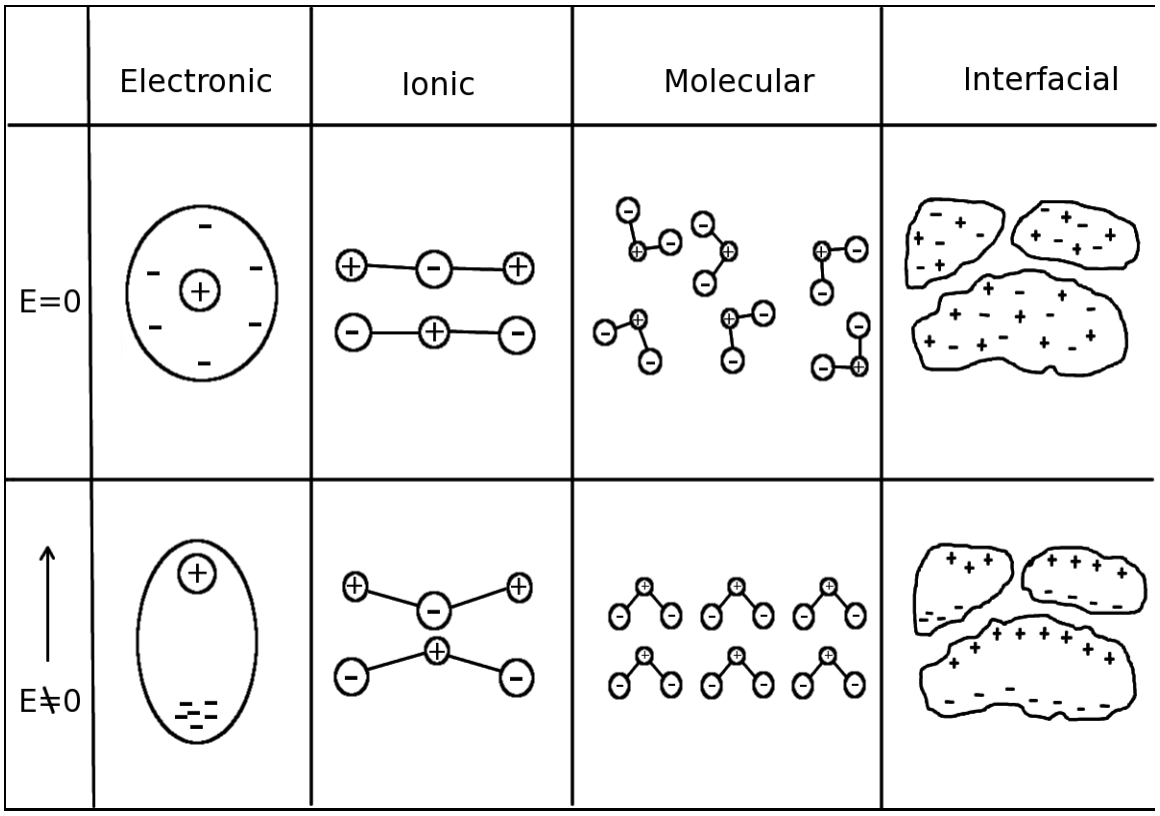

Figure (2.2): Polarization mechanisms [46].

2.6 Structural Properties

The structural properties represent important tool to study the crystallographic structure of the films.

2.6.1 Field Emission Scanning Electron Microscope (FESEM)

It is a powerful technique to study the topography, morphology and composition of the materials with much higher resolution. This is a microscope using electron beam as the probe. Its principle of operation can be understood as a modified version of scanning electron microscope, in which a field emission cathode in the electron gun is introduced. This provides a narrower probing beam at low as well as high electron energy, resulting in both improved spatial resolution and minimized sample charging and damage. When a beam of highly energetic electrons strikes the sample, the secondary electrons, X-rays and back scattered electrons are ejected

from the sample. These electrons are then collected by the detector and convert into signal that displays on a screen.

It has many advantages like it produces clearer, less electrostatically distorted images with spatial resolution 3 to 6 times better (1.5 nm) than conventional SEM [47]. Figure (2.3) shows an schematic diagram of field emission scanning electron microscope (FESEM).

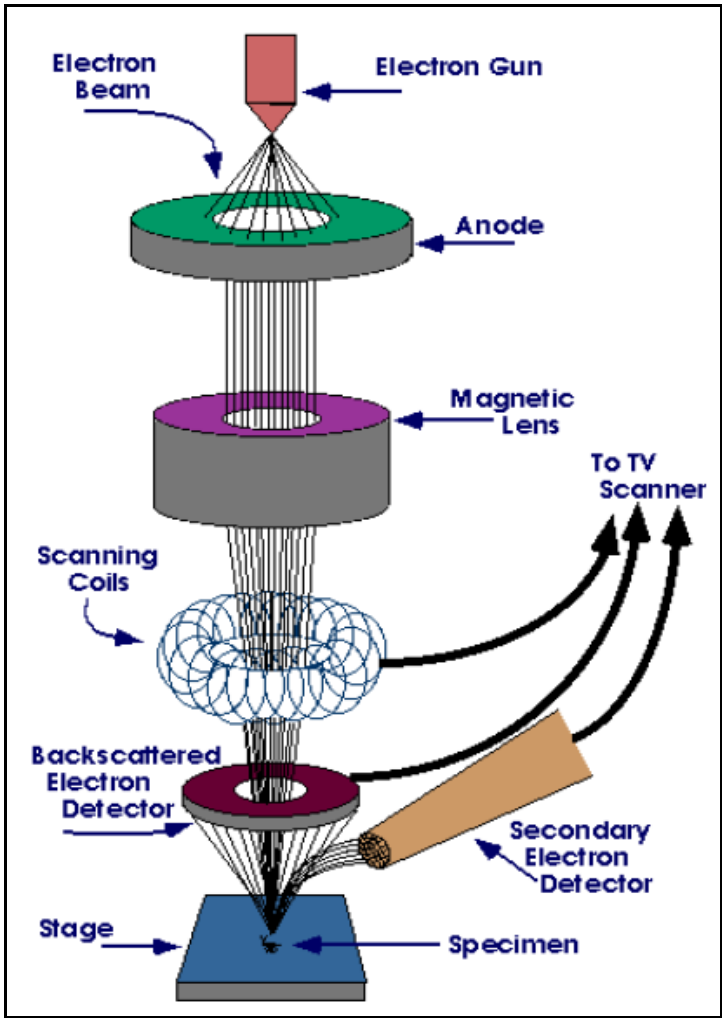

Figure (2.3): Schematic diagram of field emission scanning electron microscope (FESEM) [48].

2.6.2 Fourier Transform Infrared Spectroscopy (FTIR)

Spectroscopy is the study of molecular or atomic structure of a substance by observation of its interaction with electromagnetic radiation (here infrared (IR) radiation). The transition energy of most molecular vibrations falls within the infrared region of the electromagnetic spectrum, which can therefore be detected in an infrared spectrum [49].

Fourier transform infrared (FTIR) is one of the important analytical techniques. This type of analysis can be used for characterizing samples in the forms of liquids, solutions, pastes, powders, films, fibers, and gases. This analysis is also possible for analyzing material on the surfaces of substrate . Compared to other types of characterization analysis, FTIR is quite popular. This characterization analysis is quite rapid, good in accuracy, and relatively sensitive [50].

In the FTIR analysis procedure, samples are subjected to contact with IR radiation. The IR radiations then have impacts on the atomic vibrations of a molecule in the sample, resulting the specific absorption and/or transmission of energy. This makes the FTIR useful for determining specific molecular vibrations contained in the sample [50].

Infrared spectroscopy detects the vibration characteristics of chemical functional groups in a sample. When an infrared light interacts with the matter, chemical bonds will stretch, contract and bend. As a result, a chemical functional group tends to adsorb infrared radiation in a specific wavenumber range regardless of the structure of the rest of the molecule [51].

Modern infrared spectrophotometers analyze light of all chosen wavelengths at the same time. This is done by use of Fourier transformation, and this spectroscopy method is thus called FTIR. The key component of an FTIR instrument is the interferometer [52]. The basic construction of an interferometer is illustrated in Figure (2.4).

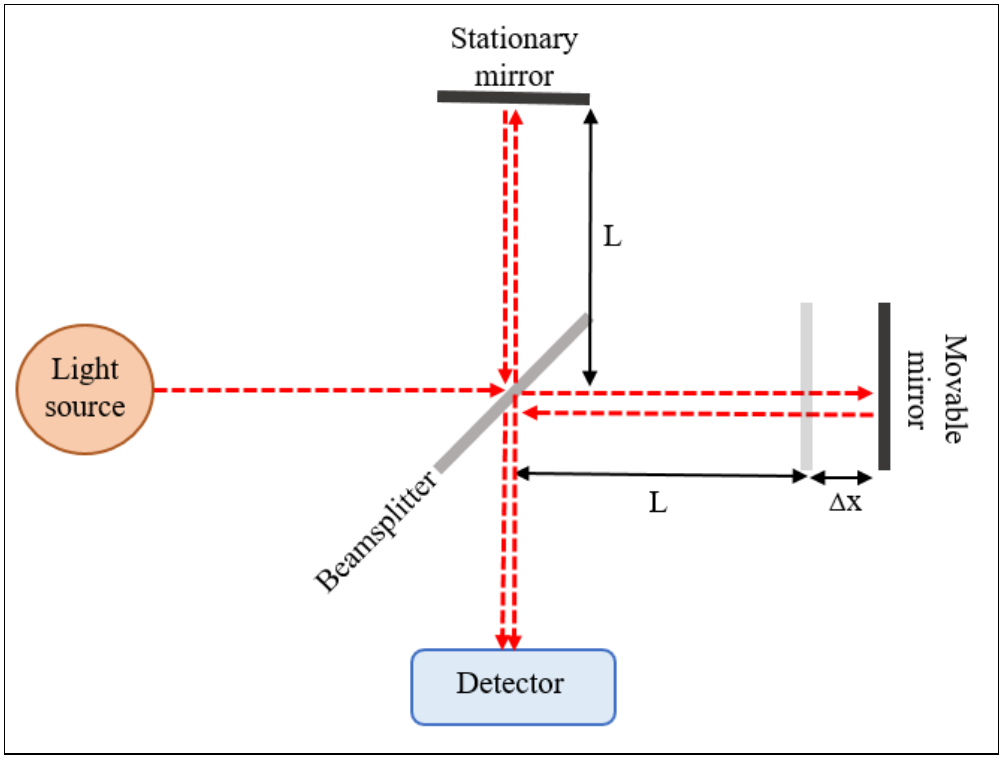

Figure (2.4): Basic construction of an interferometer [52].

In the interferometer, radiation from an infrared light source hits a beam splitter. Approximately 50% of the light is reflected towards a stationary mirror. When it hits the mirror, it will have travelled a length of L from the beam splitter. The other 50% of the light is transmitted towards a movable mirror. This beam will travel a distance of $L+\Delta x$. The difference in travelled path length between the two beams will be $2\Delta x$ when they meet in the beam splitter. This difference is called the retardation. As the mirror moves back and forth, the retardation is changing. This will lead to a pattern of constructive and destructive interference. A plot of light intensity, measured by the detector, against the retardation is called an interferogram. A computer transforms the interferogram into a plot of absorbance against wavenumber by Fourier transformation. Since light of all wavenumbers are investigated at once, the analysis only takes a few seconds [52].

The main idea gained from the FTIR analysis is to understand what the meaning of the FTIR spectrum. The spectrum can result "absorption versus wavenumber" or "transmission versus wavenumber" data [50].

The IR spectrum is divided into three wavenumber regions: far-IR spectrum (<400 cm^{-1}), mid-IR spectrum (400-4000 cm^{-1}), and near-IR spectrum (4000-13000 cm^{-1}). The mid-IR spectrum is the most widely used in the sample analysis, but far- and near-IR spectrum also contribute in providing information about the samples analyzed [50].

The mid-IR spectrum (400-4000 cm^{-1}) can roughly be divided into four ranges. The first is the high-frequency area (4000-2400 cm^{-1}) where the stretching vibrations of single bonds O-H, C-H and N-H occur. The second area (2400-1900 cm^{-1}) is where triple bonds have stretching frequencies. The double bonds (stretching) and the single bond of N-H (bending) have vibration frequencies in the third area (1900-1500 cm^{-1}). The last area (1500-400 cm^{-1}), which is called the fingerprint area, contains frequencies of most of the bending and stretching vibrations of some single bonds. The fingerprint area contains complex absorption patterns and each molecule has its own characteristic fingerprint area. The absorption peaks in the region above 1500 cm^{-1} are distinct and may be used for identification of the functional groups in the molecule [52].

2.6.3 X-Ray Diffraction (XRD)

XRD is a very valuable technique to analyze the structure of crystalline materials. It provides an effective means of identifying crystal structures and investigates lattice modifications in the implanted/annealed samples. The X-ray diffractometer uses X-rays produced from the material due to shell-shell transitions as probes for analysis. These rays are produced when high energy electrons bombard on a copper target and give out a monochromatic beam of CuK_{α} radiation. When X-rays hit a crystalline material they are diffracted by the planes of the crystal. From Bragg's law, a diffraction peak is obtained only when the distance travelled by the rays after reflection from successive crystal planes differs by an integral multiple of wavelengths, in accordance with Bragg's law [53] which is given below:

$$n\lambda = 2dsin\theta \quad (2.2)$$

Where d is interplaner spacing, θ is the incident angle, λ is the wavelength of incident X-rays, and n is the order of diffraction. The principle schematic diagram of an X-ray diffractometer is shown in Figure (2.5). A strong reflection or XRD peak is obtained by changing the angle θ so that the Bragg conditions are satisfied. Variation of angular positions with intensities of diffracted peaks produces a pattern peculiar to the material. Peak positions recorded in an XRD spectrogram are correlated with the peaks of known materials for phase analysis of the samples.

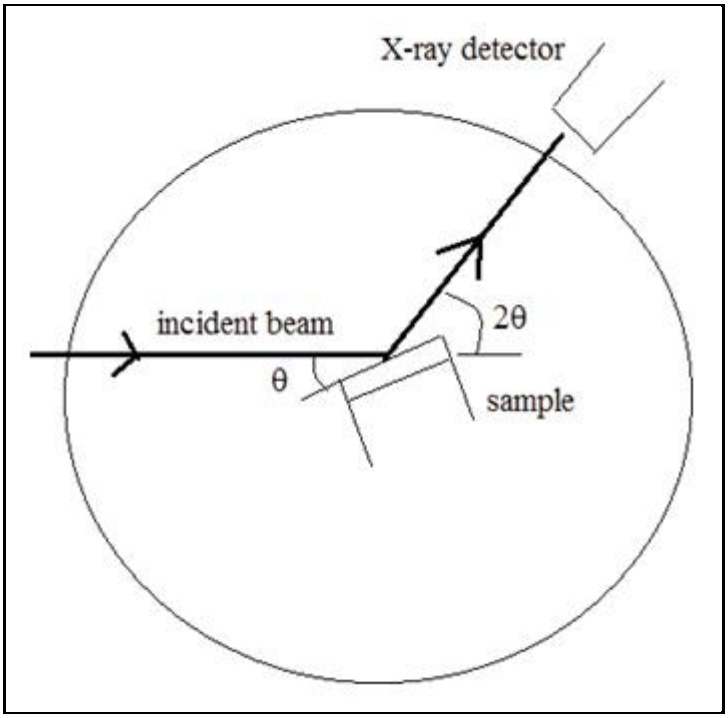

Figure (2.5): Principle and schematic diagram of diffractometer [53].

The degree of diffracted X-rays depends on arranging the material's atomic planes within the crystal lattice. Bragg's law recounts diffraction angle and lattice atomic planes spacing at specific wavelength of electromagnetic radiation. A detector is used to detect diffracted x-rays followed by processing and counting of the diffracted rays to give rise diffracted or pattern beams [54].

The particle size could be easily estimate using the Debye Scherer formula given by the following equation [55]:

$$Z = \frac{0.9\lambda}{\beta cos\theta} \quad (2.3)$$

Where, Z is the particle size (crystallite size), λ is the wavelength of the X-ray, β= FWHM of most stronger peak (highest intensity peak).

2.7 A.C Electrical Conductivity

A.C Electrical conductivity is one of the studies done on solids in order to characterize the bulk resistance of the crystalline sample. Measurement of A.C electrical conductivity can be done by different techniques. The currently used technique is the complex impedance spectroscopy which gives information on electrical properties of materials and their interface with electronically conducting electrodes. The complex impedance spectroscopy measurement of A.C electrical conductivity is based on studies made on the measurement of cell impedance/admittance over a range of temperatures and frequencies and analyzing them in complex impedance plane [56].

The dielectric constant (ε') of (PS:PMMA)/$BaTiO_3$ nanocomposite blend is calculated by the following equation [19]:

$$\varepsilon' = \frac{C_p}{C_\circ} \quad (2.4)$$

$$C_\circ = \frac{\varepsilon_\circ H}{t} \quad (2.5)$$

Where $C_p, C_\circ, \varepsilon_\circ, H,$ and t represent the parallel capacitance (in Farad), vacuum capacitance (in Farad), constant of permittivity for free space ($\varepsilon_\circ$ = 8.85x10^{-12} F/m), cross sectional area of the flat surface (in square meters), and thickness (in meters) respectively.

Hence, the dielectric constant (ε') of (PS:PMMA)/$BaTiO_3$ nanocomposite blend is calculated by the following equation:

$$\varepsilon' = \frac{C_p t}{\varepsilon_\circ H} \quad (2.6)$$

The dielectric loss (ε'') of (PS:PMMA)/$BaTiO_3$ nanocomposite blend is calculated by the following equation [19]:

$$\varepsilon'' = \varepsilon' \tan\delta \quad (2.7)$$

Where $\tan\delta$ is the loss tangent. The dielectric loss (ε'') estimates the loss of energy within the material which occurs due to the phase difference at a particular frequency.

The A.C electrical conductivity of (PS:PMMA)/$BaTiO_3$ nanocomposite blend is calculated by the equation [19]:

$$\sigma_{a.c} = \omega \varepsilon_\circ \varepsilon'' \quad (2.8)$$

Where ω is the angular frequency.

The A.C electrical conductivity ($\sigma_{a.c}$) is a measurement for the generated temperature in the insulating material resulting from the rotation of the dipoles in their positions, or the vibration of the charges as a result of the alternating of the field [57].

2.8 Optical Properties

Focusing attention on interaction of light on particles in nanometer scale, the field of nano optics has flourished greatly in the recent times. On the nanometer scale, materials including metals, semiconductors, dielectrics, and polymers exhibit interesting properties, especially optical properties. Among the various applications, innovative methods to develop thin film coatings have garnered much attention. Nanocomposite have been designed to achieve materials with tunable refractive indices and enhanced optical properties [58].

Deeper and specific focus should be laid on the interaction of light with a material. When light interacts with a material, there are three possible main effects: absorption, transmission, and reflection of light. The nanoparticles exhibit higher specific surface area, surface energy, and density compared to

bulk materials. Hence introducing nanoparticles at even lower filler loadings will have tremendous effect on the physical, thermal and mechanical properties of the matrix [59]. Nanomaterials when combined with polymers have enhanced mechanical and optical properties (e.g. refractive index and coefficient of absorption) and find applications in light emitting diodes, solar cells, polarizers, light - stable colour filters, optical sensors. The also give rise to new characteristics like light emission [60]. The optical properties of nanoparticles have been investigated for various applications like UV filters, bio imaging, photo thermal therapies, oxygen sensors etc. [61].

2.8.1 Absorbance (A)

According to the Beer-Lambert law, when light passes through a material, a certain amount of the light is absorbed . The absorbance (A) quantity that describes how much light is absorbed and can be expressed as the ratio of the absorbed light intensity (I_A) and incident light intensity ($I_\circ$), given by the following equation [62]:

$$A = \frac{I_A}{I_\circ} \tag{2.9}$$

Also we can define the absorbance (A) as the logarithm (base 10) of the reciprocal of the transmittance (T)[63]:

$$A = log_{10}(1/T) \tag{2.10}$$

2.8.2 Transmittance (T)

Transmittance (T) is the fraction of light that passes through the sample, given by the following equation [64]:

$$T = \frac{I_T}{I_\circ} \tag{2.11}$$

Where (I_T) is the light intensity after the beam of light passes through the cuvette.

2.8.3 Reflectance (R)

Reflectance is defined as fraction of light reflected at an interface,

$$R = \frac{I_R}{I_\circ} \tag{2.12}$$

Where (I_R) are the reflected beam intensity [65].

We can obtained reflectance from absorbance and transmittance spectrum in accordance to the law of conservation of energy by the relation [66]:

$$R + T + A = 1 \tag{2.13}$$

2.8.4 Absorption Coefficient (α)

Absorption coefficient can be defined; it is the ratio of decrease in radiation energy flux to the unit of distance towards the wave propagation in the material which depends on the type of absorbent material and wavelength of the incident wave [67].

The absorption coefficient at a fundamental absorption edge can be written as [68]:

$$\alpha = \frac{2.303}{t} A \tag{2.14}$$

Where: α is the absorption coefficient.

2.8.5 Extinction Coefficient (K)

The extinction coefficient represents the amount of attenuation of an electromagnetic wave that is traveling in a material, where it values depends on the density of free electrons in the material and also on the structure nature, this coefficient can be calculated by using the following equation [69]:

$$K = \frac{\alpha\lambda}{4\pi} \tag{2.15}$$

It can be noted that (K) has same behavior of absorption coefficient, absorption coefficient has a direct related with (K) as in the above equation [70].

2.8.6 Refractive Index (n)

Refractive index (n) represents the ratio of the light speed in space (c) to the light speed inside the material (v). Equation (2-16) gives the law which used to calculate the refractive index [71]:

$$n = \left(\frac{4R}{(R-1)^2} - K^2\right)^{1/2} - \frac{(R+1)}{(R-1)} \tag{2.16}$$

Complex refractive index (n^*) can be written as following:

$$n^* = n - iK \tag{2.17}$$

Where, n is the real part of refractive index. (K) it is the extinction coefficient represents the imaginary part. (n^*) it is a complex number represent the complex refractive index that depends on several characteristic factors such as crystal defect and crystal structure [72].

2.8.7 Dielectric Constant (ε)

The dielectric constant (ε) is defined as the ratio of the electric permeability of the material to the electric permeability of free space. The dielectric constant is generally a complex number which describes the interaction of a material with an electric field:

$$\varepsilon = \varepsilon_r - i\varepsilon_i \tag{2.18}$$

Where (ε_r) is a real part of the dielectric constant , (ε_i) is an imaginary part of the dielectric constant.

The real part of the complex dielectric constant (ε_r) is a measure of how much energy from an external field is stored in a material.

The imaginary part of the complex dielectric constant (ε_i) is a measure of how dissipative or lossy a material is to an external field [73].

The dielectric constant (ε) is not constant by changing either the frequency or the temperature [74].

The relation between the complex dielectric constant (ε) and the complex refractive index (n^*) is expressed by [75]:

$$\varepsilon = (n^*)^2 \quad (2.19)$$

It can be concluded that

$$\varepsilon_r - i\varepsilon_i = (n - iK)^2 \quad (2.20)$$

The real and imaginary parts of the dielectric constant thus related to (n) and (K) values and can be calculated using the following formulas [75]:

$$\varepsilon_r = n^2 - K^2 \quad (2.21)$$

And

$$\varepsilon_i = 2nK \quad (2.22)$$

2.8.8 Fundamental Absorption Edge

An absorption edge, absorption discontinuity or absorption limit is a sharp discontinuity in the absorption spectrum of a substance. These discontinuities occur at wavelengths where the energy of an absorbed photon corresponds to an electronic transition or ionization potential [76].

A typical relationship between the absorption coefficient and the photon energy observed in a crystalline semiconductor is shown in Figure (2.6), where various possible absorption processes are illustrated. The important features of the behavior of the α versus $h\nu$ can be summarized as follows:

1. Free carrier absorption due to the presence of free electrons and holes, an effect that decreases with increasing photon energy.
2. An impurity absorption band (usually narrow) due the various dopants.
3. Reststrahlen or lattice absorption in which the radiation is absorbed by vibrations of the crystal ions.
4. Exciton absorption peaks that are usually observed at low temperatures and are close the fundamental absorption edge; and
5. Band to band or fundamental absorption of photons, which excites an electron from the valence to the conduction band.

Type 5 absorption has a large absorption coefficient and occurs when the photon energy reaches the band gap energy E_g. It is probably the most important absorption effect; its characteristics for $h\nu > E_g$ [77].

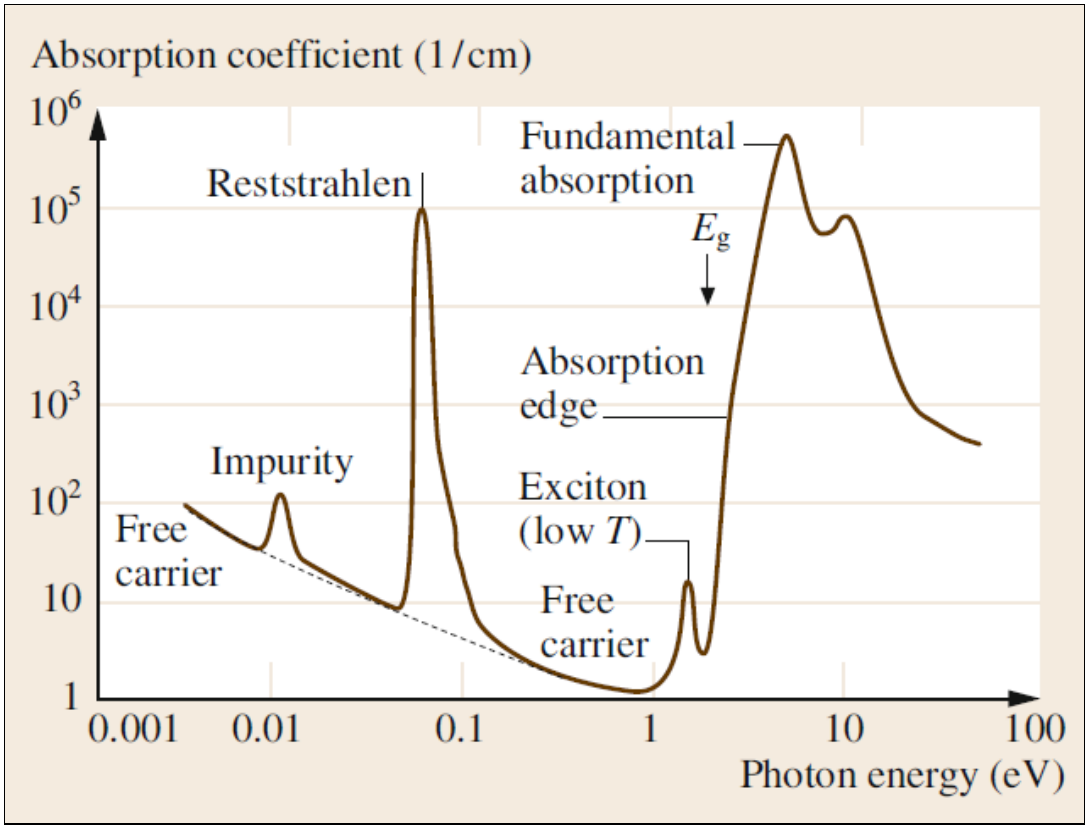

Figure (2.6): Absorption coefficient plotted as a function of the photon energy in a typical semiconductor, illustrating various possible absorption processes [77].

The optical absorption in amorphous semiconductors near the absorption edge is usually characterized by three types of optical transitions corresponding to transitions between tail and tail states, tail and extended states, and extended and extended states. The first two types correspond to $\hbar\omega \leq E_\circ$, and the third one corresponds to $\hbar\omega \geq E_\circ$ where $\hbar\omega$ is the photon energy and $E_\circ$ is the optical band gap energy. Thus, the plot of absorption coefficient versus photon energy (α versus $\hbar\omega$) has three different regions, A, B and C respectively, that correspond to these three characteristic optical transitions shown in Figure (2.7) [77].

In the small absorption coefficient range A (also called the weak absorption tail (WAT)), where $\alpha < 10^{-1}$ cm^{-1}, the absorption is controlled by

optical transitions from tail to tail states. As stated above, the localized tail states in amorphous semiconductors are contributed to by defects. To some extent, the absolute value of absorption in region A may be used to estimate the density of defects in the material. In region B, where typically $10^{-1} < \alpha < 10^{4}$ cm^{-1}, the absorption is related to transitions from the localized tail states above the valence band edge to extended states in the conduction band and/or from extended states in the valence band to localized tail states below the conduction band. The spectral dependence of α usually follows the so-called Urbach rule (Excite electrons from states below E_F in the VB, where the band is nearly parabolic, to tail states below E_c, where the density of states decreases exponentially with energy into the band gap, away from E_c. Such excitations lead to α depending exponentially on $h\nu$, a dependence that is called the Urbach rule), In region C, the absorption is controlled by transitions from extended to extended states. For many amorphous semiconductors, the α versus $\hbar\omega$ behavior follows the Tauc relation [77].

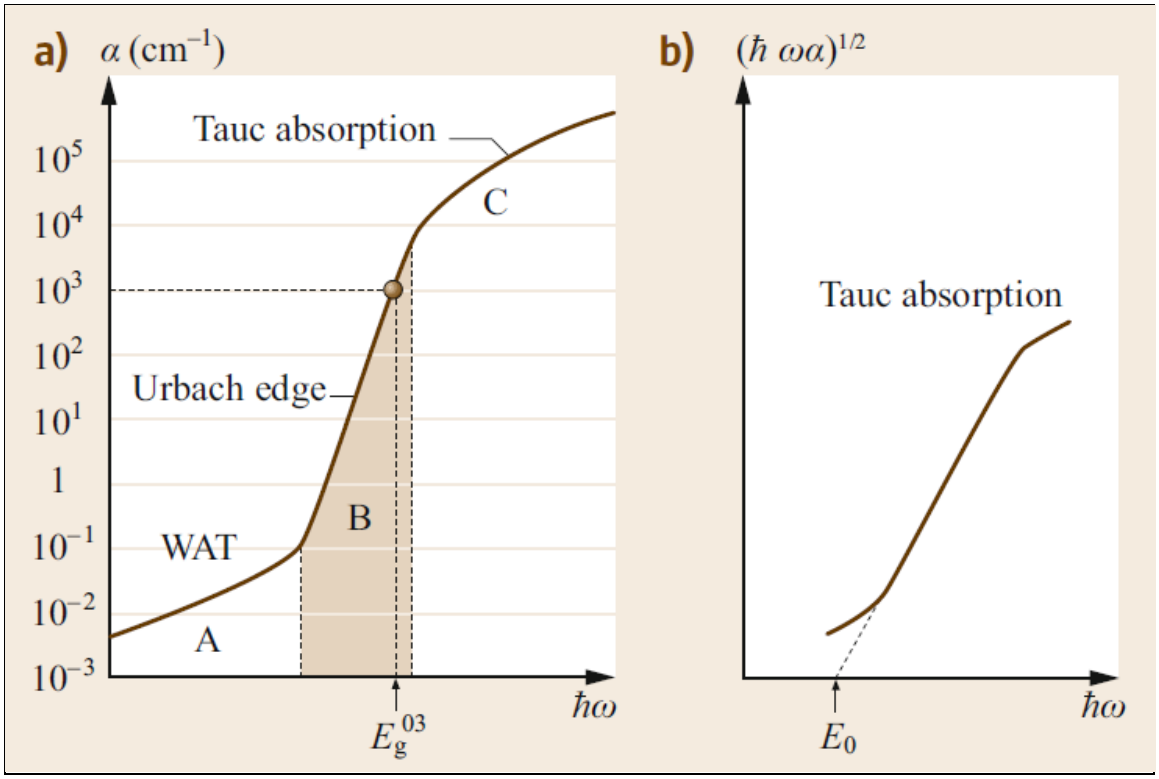

Figure (2.7): (a,b) Typical spectral dependence of the optical absorption coefficient in amorphous semiconductors [77].

2.8.9 Electronic Transitions

The optical properties are analyzed from the response of the materials due to the exposure to electromagnetic radiation, particularly visible light. From a quantum mechanical viewpoint, the electromagnetic radiation is considered as a form of energy named photons instead of waves [78].

The photon energy is quantized through Planck's law:

$$E = h\nu = hc/\lambda \quad (2.23)$$

Where, h refers to the Planck constant, and λ refers to the photon wavelength. As a fact, when a light wave propagates through materials, it experiences attenuation with distance. Photons have the capability for exciting electrons from the occupied levels in the VB to the unoccupied levels in the CB. This procedure is purely quantum mechanical in nature and is known as interband transitions [79]. The analysis of the α data in response to the wavelength in the evaluation of the optical band gap is found to be dependent on Tauc's relation [80].

$$\alpha h\nu = B(h\nu - E_{\circ})^{r} \quad (2.24)$$

Where, α is the absorption coefficient, $h\nu$ refers to the photon energy (eV), B is a proportionality constant, $E_{\circ}$ is the optical band gap energy between the valence band and the conduction band and r is the value of the exponent and denotes the nature of the electronic transition, whether allowed or forbidden and whether direct or indirect. Specifically, r can take the values 1/2, 3/2, 2 or 3 for transitions designated as direct allowed, direct forbidden, indirect allowed, and indirect forbidden respectively [78,81,82]. Figure (2.8) illustrates the different types of electronic transition that can exist between the valence band and conduction band based on Tauc's model [83].

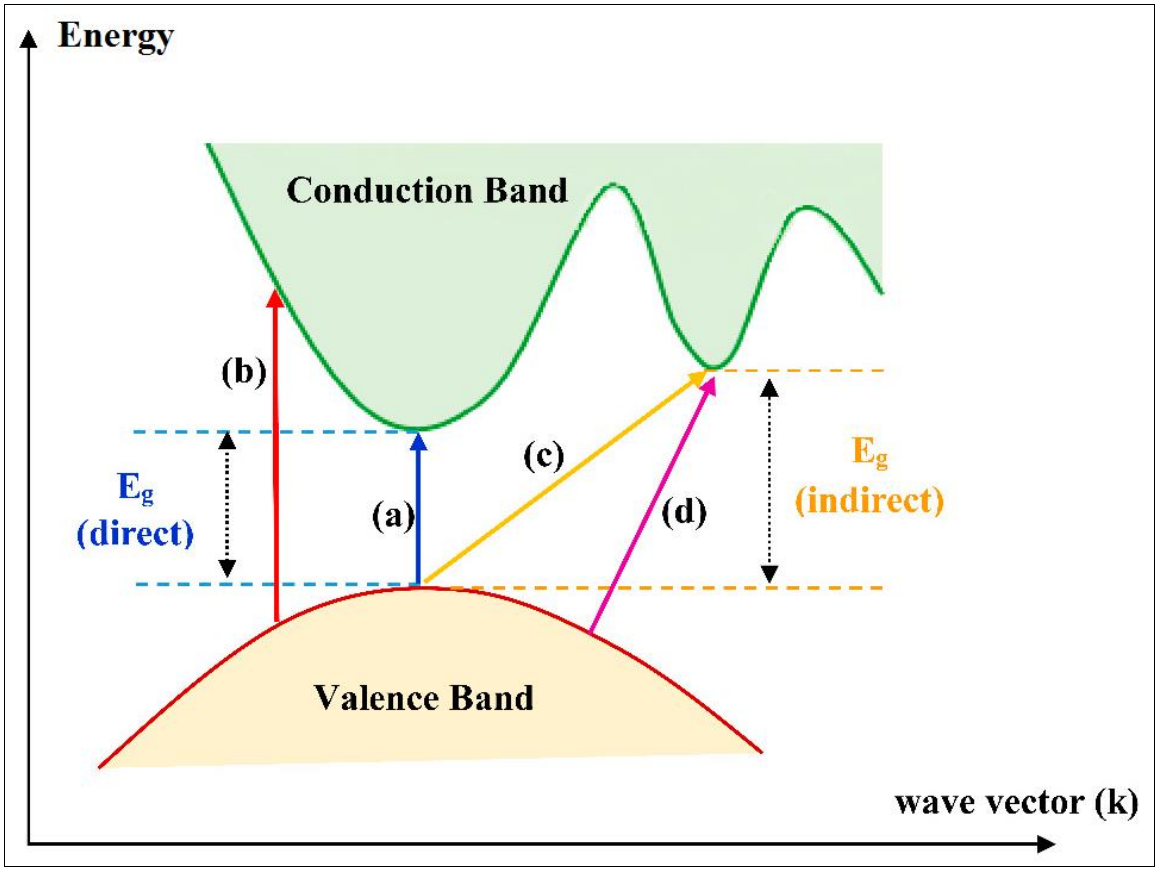

Figure (2.8): Electronic transition (a) allowed direct (b) forbidden direct (c) allowed indirect (d) forbidden indirect [83].

2.8.10 Optical Conductivity

The optical conductivity is a measure of the frequency response of the material when irradiated with light [84]:

$$\sigma_{opt} = \frac{\alpha n c}{4\pi} \qquad (2.25)$$

2.9 Piezoelectricity

Piezoelectricity comes from the Greek words "piezo" and "electricity" that the word "piezo" is a derivative of a Greek word which means "to press" and "electricity" has the same meaning as English word "electricity" [85].

Piezoelectricity is a quality of material asymmetry that leads to the conversion of electric signals into physical deformation and conversely physical deformation into electric signal [86].

Piezoelectric effect is not a completely novel idea since it has been known since the 19$^{th.}$ century with broad technological applications since the

beginning of the 20th. century. The discovery of piezoelectric effect is connected with the names of famous physicists Jacques Curie and Pierre Curie who recognized that anisotropic crystals i.e. crystals without center of symmetry can generate electric dipole when mechanically squeezed. The described effect can work in oppose way when an anisotropic crystal become deformed due to voltage imposed on it [87].

There are 32 crystal classes which are divided into the following seven groups: triclinic, monoclinic, orthorhombic, tetragonal, trigonal, hexagonal, and cubic. Only 20 of the 32 classes allow for piezoelectric properties. Ten of these classes are polar, i.e. show a spontaneous polarization without mechanical stress due to a non-vanishing electric dipole moment associated with their unit cell. The remaining 10 classes are not polar, i.e. polarization appears only after applying a mechanical load [88].

Figure (2.9) shows a simple molecular model of piezoelectric material. It explains the generating of an electric charge as the result of a force exerted on the material. Before subjecting the material to some external stress, the gravity centers of the negative and positive charges of each molecule coincide. Therefore, the external effects of the negative and positive charges are reciprocally cancelled. As a result, an electrically neutral molecule appears (Figure 2.9a). When exerting some pressure on the material, its internal reticular structure can be deformed, causing the separation of the positive and negative gravity centers of the molecules and generating little dipoles (Figure 2.9b). The facing poles inside the material are mutually cancelled and a distribution of a linked charge appears in the material's surfaces-the material is polarized (Figure 2.9c). This polarization generates an electric field and can be used to transform the mechanical energy used in the material's deformation into electrical energy [88].

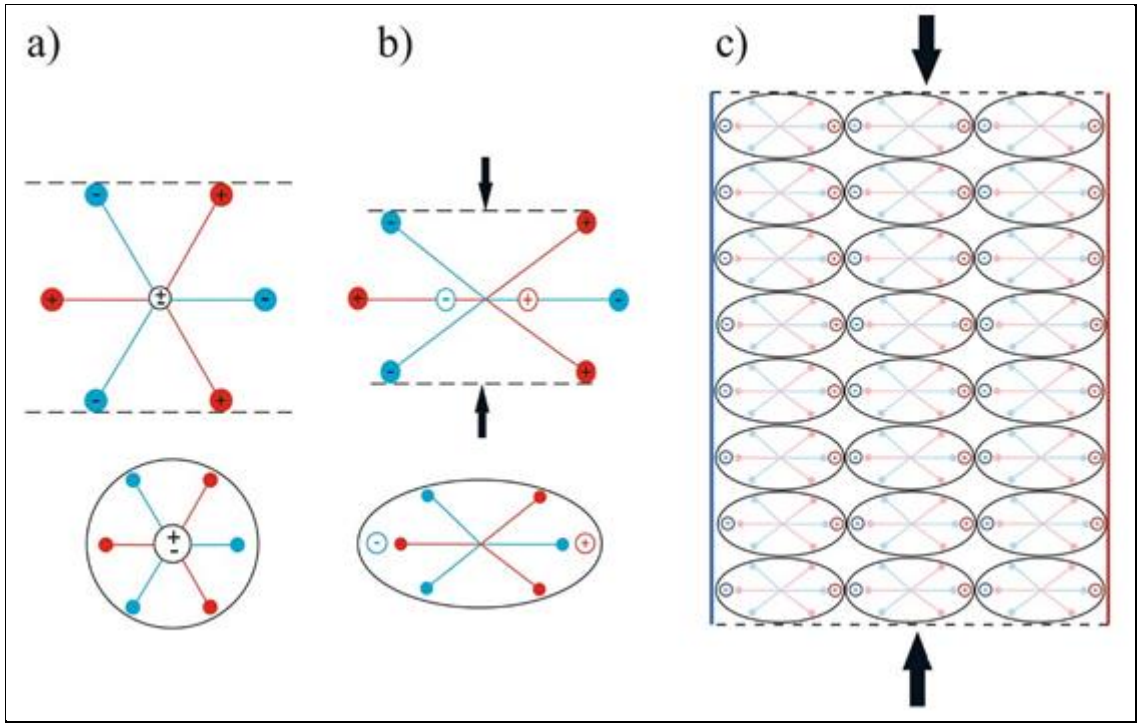

Figure (2.9): Simple molecular model of piezoelectric material: a) an electrically neutral molecule appears, b) generating little dipoles, c) the material is polarized [88].

Piezoelectric effect exists in two domains; namely, direct piezoelectric effect and converse piezoelectric effect. Direct piezoelectric effect describes the ability to convert mechanical energy to electrical energy which is also known as generator or transducer effect while the converse piezoelectric effect describes the ability of transforming electrical energy to mechanical energy which is also known as motor/actuator effect. The electrical energy generated by direct piezoelectric effect can be stored to power electronic devices and it is known as "energy/power harvesting".

According to the definition of "direct piezoelectric effect", when a mechanical strain is applied to crystals by an external stress, an electric charge occurs on the surface (s) of the crystal and the polarity of this observed electric charge on the surface (s) can be reversed by reversing the direction of the mechanical strain applied as shown in Figure (2.10) [85].

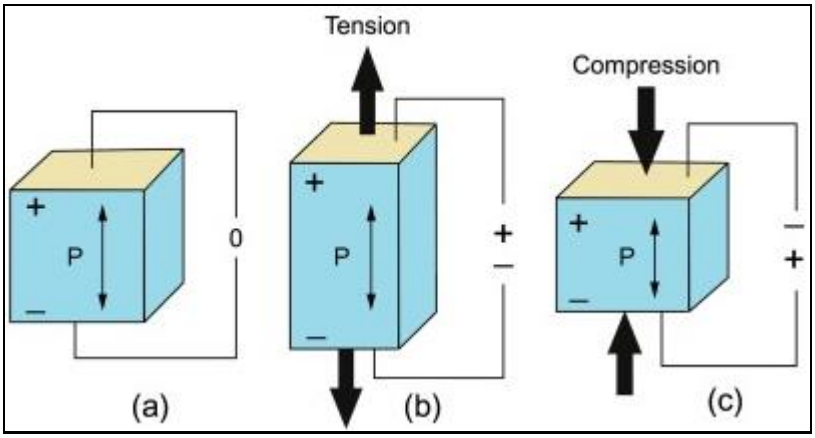

Figure (2.10): Schematic of direct piezoelectric effect; (a) piezoelectric material, (b) energy generation under tension, (c) energy generation under compression[85].

On the other hand, according to the definition of "converse piezoelectric effect", when an electric field is applied to a crystal or a crystal is subjected to an electric field, a mechanical deformation on the surface is observed which is generally seen as a change in dimensions of the crystal. The direction of the mechanical strain can also be reversed as shown in Figure (2.11), by reversing the applied electric field [85].

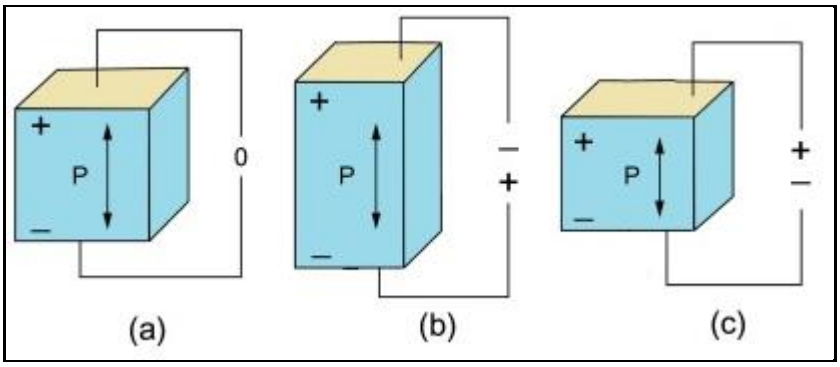

Figure (2.11): Schematic of converse piezoelectric effect; (a) piezoelectric material, (b) dimensional change when an electrical charge applied, (c) dimensional change when an opposite electrical charge applied [85].

There are around 200 piezoelectric materials used in energy harvesting applications, found in four main categories [89]:

1.Single crystals (Rochelle salt, lithium niobite, quartz crystals).

2.Ceramics (barium titanate ($BaTiO_3$), lead zirconate titanate (PZT), potassium niobate ($KNbO_3$)).

3.Polymers (polylactic acid (PLA), polyvinylidene fluoride (PVDF), copolymers, cellulose and derivatives).

4.Polymer composites or nanocomposites (polyvinylidene fluoride-zinc oxide (PVDF-ZnO), cellulose-$BaTiO_3$, polyimides-PZT).

The equations that describe the piezoelectric effect can be written as [90]:

$$D_m = d_{mi}^{T} T_{ij} + \epsilon_{mk}^{T} E_k \quad (2.26)$$

$$S_i = s_{ij}^{E,T} T_{ij} + d_m^{T} E_m \quad (2.27)$$

Where D_m is the electric displacement vector, d_{mi}^{T} is the matrix constant for the direct piezoelectric effect, T_{ij} is the stress vector, ϵ_{mk}^{T} is the matrix of dielectric permittivity under conditions of constant mechanical stress, E_k is the electric field vector, S_i is the strain vector, $s_{ij}^{E,T}$ is the matrix of compliance coefficients at constant electric field strength, and the subscript (m) denotes matrix transposition. The indices take values i , j = 1..... 6 and m = 1,2,3.

From equation (2.26) it can be observed that for $E = 0$ a displacement appears when applying a mechanical strain. This is known as the direct piezoelectric effect (equation (2.28)):

$$D_m = d_{mi}^{T} T_j \quad (2.28)$$

From equation (2.27) it is observed that for $T_{ij} = 0$ deformations can be obtained by applying an electric field. That is known as the converse piezoelectric effect (equation (2.29)):

$$S_i = d_m^{T_{ij}} E_m \quad (2.29)$$

Fundamental parameter used in electromechanical applications is the electromechanical coupling factor Y. It is a dimensionless number related to conversion of energy from a mechanical source to electrical work, or vice versa, over an idealized work cycle. It is expressed as [88]:

$$Y^2 = \frac{\text{Electrical energy converted to mechanical energy}}{\text{Input electrical energy}} \quad (2.30)$$

Or:

$$Y^2 = \frac{\text{Mechanical energy converted to electrical energy}}{\text{Input mechanical energy}} \qquad (2.31)$$

Advantages and disadvantages of piezoelectric materials in our daily life are shown in Table (2.1).

Table (2.1): Advantages and disadvantages of piezoelectric materials [91].

No.	Advantages	Disadvantages
1	Reliable, economical, eco-friendly	Capital cost is high
2	Less consumption of non-renewable energies	Replace and maintenance is difficult
3	Extremely wide dynamic range, almost free of noise	Cost of replace and maintenance is more
4	Suitable for shock measurement	
5	Imperceptible vibration	
6	Excellent linearity over their dynamic range	
7	Compact yet highly sensitive	
8	No moving parts-long service life	
9	Self-generating-no external power required	
10	Great variety of models available for nearly any purpose	

Piezoelectric materials have numerous applications in the field of engineering and medicine. The distinctive characteristic of the material, which is a bidirectional energy conversion capability, makes piezoelectric materials highly suited for the design of smart systems. Good examples of smart systems are industrial and medical robots. Piezoelectric materials found applications in this area as: piezoelectric tactile (sensitive to touch) sensors, vibration sensors and ultrasonic detectors for detection and sensing. Piezoelectric motors, benders and vibrators, graspers and precision

positioners, on the other hand, are used in robotics for motion control and handling of objects [88]. The main engineering applications of piezoelectric materials with the distinction of the piezoelectric phenomenon used are shown in Figure (2.12).

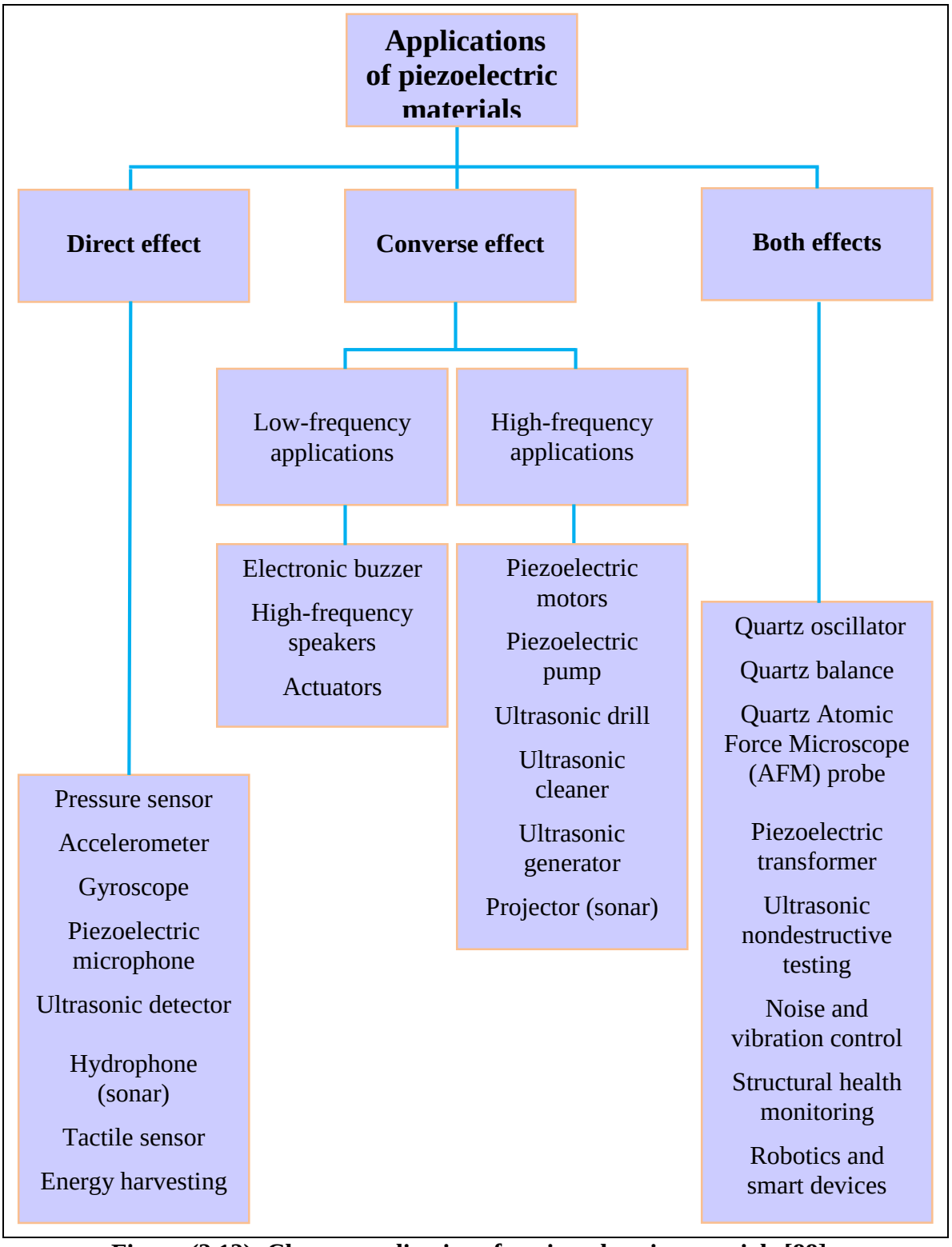

Figure (2.12): Chosen applications for piezoelectric materials [88].

2.10 Antibacterial Activity

A fundamental laboratory technique in general biology and microbiology courses is staining of bacterial cells on glass slides for visualization and characterization purposes. A common procedure, the gram stain, differentiates between bacterial species based on the chemical composition of their cell walls. The staining procedure involves applying a primary stain, crystal violet, followed by gram's iodine, which acts as a mordant, decolorizing with an organic solvent such as ethanol, and counterstaining with safranin. Following the procedure, gram positive bacteria, which are more resistant to decolorization, appear purple in color while gram negative bacteria, which are more sensitive to decolorization, appear pink [92] as shown in Figure (2.13) [93].

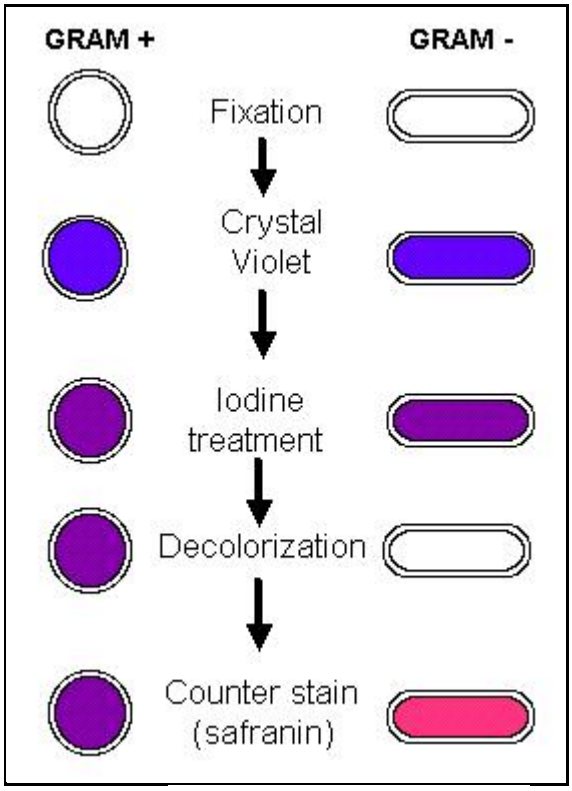

Figure (2.13): The steps in gram staining [93].

Gram stain interpretation gives information about the presence or absence of bacterial disease and can guide the initial antibiotic treatment.

Gram stain also provides additional information about the host immune response and quality of the specimen. A well prepared sample can show the organism color, size, shape, and arrangement, allowing cellular morphology to further separate bacteria into four major groups. Cocci are spherical or oval, bacilli are rod like or cylindrical, vibrios are comma shaped or curved like and spirochetes are flexible [94].

In both gram positive and gram negative bacteria, the cell wall is constructed from the polymer peptidoglycan, a composite of long strands of glycans crosslinked by stretchable peptides. The resulting elastic network protects the cell from lysis. Initially, glycans are polymerized as strands of up to 100 disaccharide subunits. The steady-state length distribution of glycan strands in Escherichia coli is extremely broad, with a mean of ≈20–30 disaccharide units depending on strain, conditions, and growth phase, and some strand lengths ranging upwards of 80 units. Each disaccharide unit in a glycan strand is synthesized with a covalently linked peptide that can be crosslinked to a peptide emanating from another glycan strand [95].

Figure (2.14) presents the well-established structural differences between gram positive and gram negative bacteria.

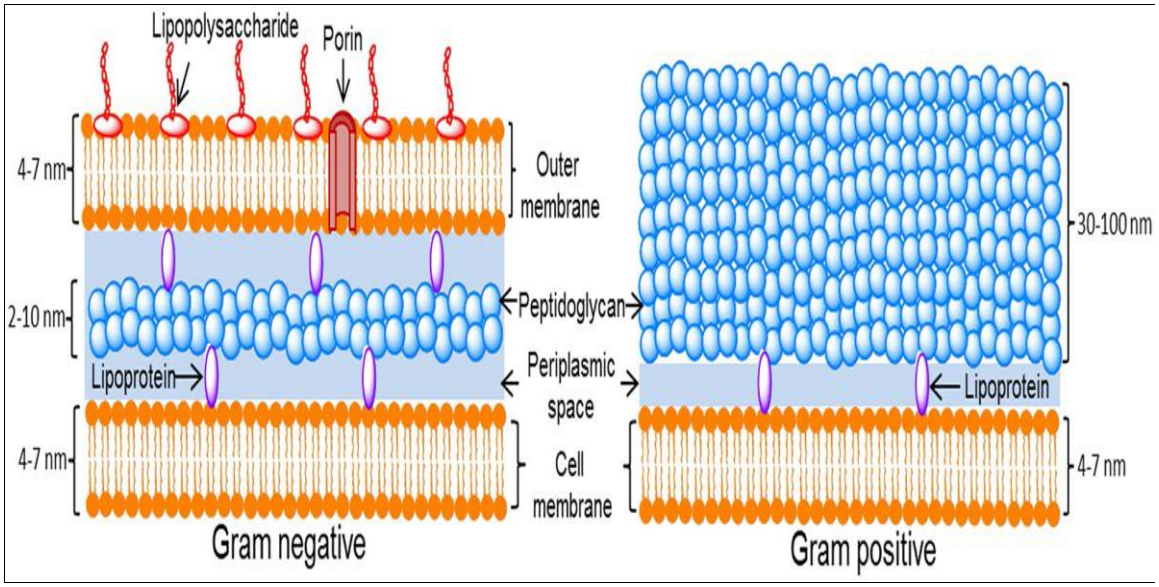

Figure (2.14): Cell wall structure for gram positive and gram negative bacteria[96].

Table (2.2) illustrates comparison between gram positive and gram negative bacteria.

Table (2.2): Comparison between gram positive and gram negative bacteria[97].

Characteristic	Gram positive	Gram negative
Gram reaction	Retain crystal violet dye and stain dark violet or purple	Can be decolorized to accept counter stain (safranin) and stain red
Peptidoglycan layer	Thick (multilayered)	Thin (single-layered)
Teichoic acid	Present in many	Absent
Periplasmic space	Absent	Present
Outer membrane	Absent	Present
Lipopolysaccharide (LPS) content	Virtually none	High
Lipid and lipoprotein content	Low (acid fast bacteria have lipids linked to peptidoglycan)	High (due to presence of outer membrane)
Flagellar structure	2 rings in basal bodies	4 rings in basal bodies
Toxins produced	Primarily exotoxins	Primarily endotoxins
Resistance to physical disruption	High	Low
Cell wall disruption by lysozyme	High	Low
Resistance to drying	High	Low
Inhibition by basic dyes	High	Low
Susceptibility to anionic detergents	High	Low

Nanoparticles are particles with a size not greater than 100 nm, with spherical, cubic and needle-shaped forms. They are formed from different materials, either metallic or polymeric and their active surface area,

chemical reactivity and biological activity, are often radically different from larger size particles. These features allow the nanoparticles interact closely with microbial membranes and, therefore, their antimicrobial effect is not due exclusively to the release of metal ions [98].

An inverse relationship between the size of the nanoparticles and antimicrobial activity has been clearly demonstrated, where particles in the range of (1-10) nm in size have demonstrated greater killing activity against bacteria compared to larger particles. It is reported that in gram negative bacteria nanoparticles acted mainly in the range of (1-10) nm. In addition, by adhering to the surface of the cell membrane, they drastically disrupt its functions, such as permeability and cellular respiration. They are able to penetrate into the bacteria and cause further damage by possible interactions with sulfur and phosphorus containing compounds such as DNA. They release ions, which will make an additional contribution to the bactericidal effect of nanoparticles. However, in the case of silver nanoparticles, it has been shown that smaller nanoparticles are more toxic than larger particles, even when they are oxidized [98].

Metal nanoparticles are used in insecticide and bactericide for many years. Metal nanoparticles exhibit different antibacterial properties according to the surface to volume ratio. Gram positive bacteria exhibit greater resistance to metal nanoparticles compared to gram negative bacteria, this could be related to the structure of the cell wall [99].

Bacterial cell size is in the micrometer range, while its outer cellular membranes have pores in the nanometer range. Nanoparticles which are smaller in size than bacterial pores will have a unique ability of crossing the cell membrane [18].

Nanoparticles in particular have demonstrated broad spectrum antibacterial properties against both gram positive and gram negative bacteria. For example, ZnO NPs were found to inhibit Staphylococcus

aureus, and Ag NPs exhibit concentration dependent antimicrobial activity against Escherichia coli and Pseudomonas aeruginosa. However, the detailed antibacterial mechanisms of NPs have not been thoroughly explained, and the same types of NPs often present contrasting effects [100].

NPs need to be in contact with bacterial cells to achieve their antibacterial function. The accepted forms of contact include electrostatic attraction, van der Waals forces, and receptor–ligand and hydrophobic interactions. NPs then cross the bacterial membrane and gather along the metabolic pathway, influencing the shape and function of the cell membrane. Thereafter, NPs interact with the bacterial cell's basic components, such as DNA, lysosomes, ribosomes, and enzymes, leading to oxidative stress, heterogeneous alterations, changes in cell membrane permeability, electrolyte balance disorders, enzyme inhibition, protein deactivation, and changes in gene expression [100].

The antimicrobial mechanism of action of NPs is generally described as adhering to one of three models: oxidative stress induction, metal ion release, or non-oxidative mechanisms. These three types of mechanisms can occur simultaneously. Certain studies have proposed that Ag NPs prompt neutralization of the surface electric charge of the bacterial membrane and change its penetrability, ultimately leading to bacterial death. Moreover, the generation of reactive oxygen species (ROS) inhibits the antioxidant defense system and causes mechanical damage to the cell membrane. According to existing research, the major processes underlying the antibacterial effects of NPs are as follows: (1)Disruption of the bacterial cell membrane; (2)Generation of ROS; (3)Penetration of the bacterial cell membrane; and (4)Induction of intracellular antibacterial effects, including interactions with DNA and proteins [100].

3.1 Introduction

This chapter deals with the preparation (PS:PMMA) poly blend and (PS:PMMA)/$BaTiO_3$ nanocomposite blend films by utilizing solution casting technique. The right procedures from the substrates cleaning, required specifications and optimal conditions of preparation which are used in this research work in order to prepare well-formed and homogeneous films onto substrates (glassy Petri dishes) with very low surface roughness. This chapter involves the description of all instruments that were employed in this research work. Details of the experimental set up made for testing and studying the performance of the piezoelectric and medical applications is also presented in this chapter. Figure (3.1) explain the main steps for the procedure.

3.2 The Materials Used in This Work

3.2.1 Polymers

Two polymers are used in this work:

A) Polystyrene (PS)

Used as granular form and could be obtained from Tuttlingen German company with high purity (99%).

B) Poly Methyl Methacrylate (PMMA)

It was obtained as granular form and could be obtained from Tuttlingen German company with high purity (99%).

3.2.2 Barium Titanate Nanoparticles ($BaTiO_3$)

It was obtained as powder and could be obtained from ThermoFisher German company with particle size (20nm) and high purity (99%). Nanomaterial ($BaTiO_3$) is tested by using Bettersize2000 laser particle size analyzer. This instrument is present in Department of Electro-chemical, College of Material Engineering, University of Babylon.

3.3 Substrates Cleaning

The cleaning of substrates is very important process because the influences like oil or dust influence on the properties of the films. It can be summarized the glass substrate cleaning as follows:

1. The substrates (glassy Petri dishes) were washed several times using hot distilled water and detergent (Ethyl Alcohol).
2. After this, substrates were exposed to ultrasonic waves using ultrasonic cleaner for 15 minutes in a solution of distilled water and detergent.
3. Finally, the substrates were washed with distilled water and detergent separately, then dried in an oven.

3.4 Solution Casting Technique

Solvent casting is a conventional and rapid technique for the fabrication of free standing films. Here the nanoparticles are either suspended or dissolved in a solution of polymers in a volatile solvent, like water or chloroform. Additionally plasticizers can also be added based on the specific requirement. The solution is then poured into glass petri dish or flat plate. Then the sample is kept for drying in oven or at room temperature (25˚C). The dried films are then peeled off from the glass plate and stored in vacuum sealed covers. The typical process of solution casting technique of nanocomposite material is schematically shown in Figure (3.1).

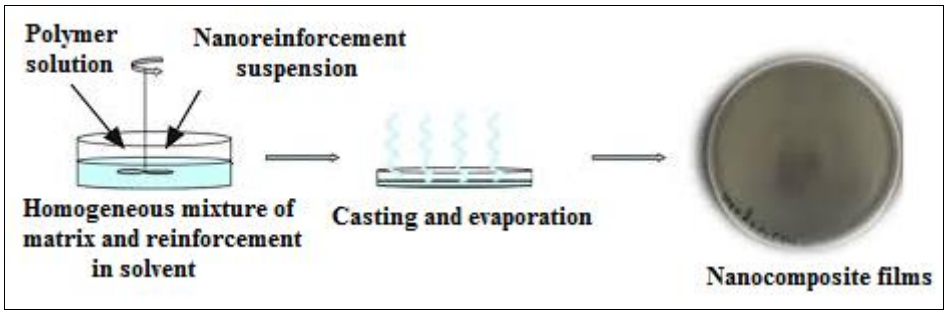

Figure (3.1): Schematic representation of a typical solution casting technique.

3.5 Preparation of (PS:PMMA)/$BaTiO_3$ Nanocomposite Blend

The (PS:PMMA)/$BaTiO_3$ nanocomposite blend have been prepared as shown in Figure (3.2) by the following steps:

1. Solve (0.6g) of polystyrene (PS) granules in (30mL) of 1,2-Dichloroethane ($C_2H_4Cl_2$) solvent using magnetic stirrer until PS granules completely dispersion then add (1.4g) of poly methyl methacrylate (PMMA) granules until PMMA granules completely dispersion.
2. The homogeneous mixture of (PS:PMMA) poly blend poured carefully into a clean dry glassy petri dish placed on a flat surface by solution casting technique.
3. Cover the mixture with a petri dish lid and leave it for several days until 1,2-Dichloroethane solvent completely evaporate at room temperature.
4. Repeat the step (1) for the other weights of PS, PMMA, $BaTiO_3$ mentioned in Table (3.1).
5. Put the beaker which contain (PS:PMMA)/$BaTiO_3$ nanocomposite blend in an ultrasonic bath (40kHz ultrasonic agitation for 30 minute to ensure uniform dispersion of $BaTiO_3$ nanoparticles in (PS:PMMA) poly blend, via the method which is called indirect ultrasonication, in an ultrasonic bath filled with water (Ultrasonic Cleaner instrument has the following characteristics: Model: FSF-020S, Capacity: 3L, Tank Size: 240x135x100mm, Ultrasonic Power: 120W, Heating Power: 100W, Ultrasonic Frequency: 40kHz, Voltage: AC220-240V, Timer: 0-30 min).
6. After the ultrasonication procedure, repeat the step (2) and the step (3) for the homogeneous solution of (PS:PMMA)/$BaTiO_3$ nanocomposite blend.
7. Finally, peel the poly blend and nanocomposite blend films from the glassy petri dish using a doctor blade, these poly blend and nanocomposite blend films having thickness (0.25mm). For further characterization, these films were preserved in a desiccator.
8. The weight of the solved materials in preparation each film was (2g).

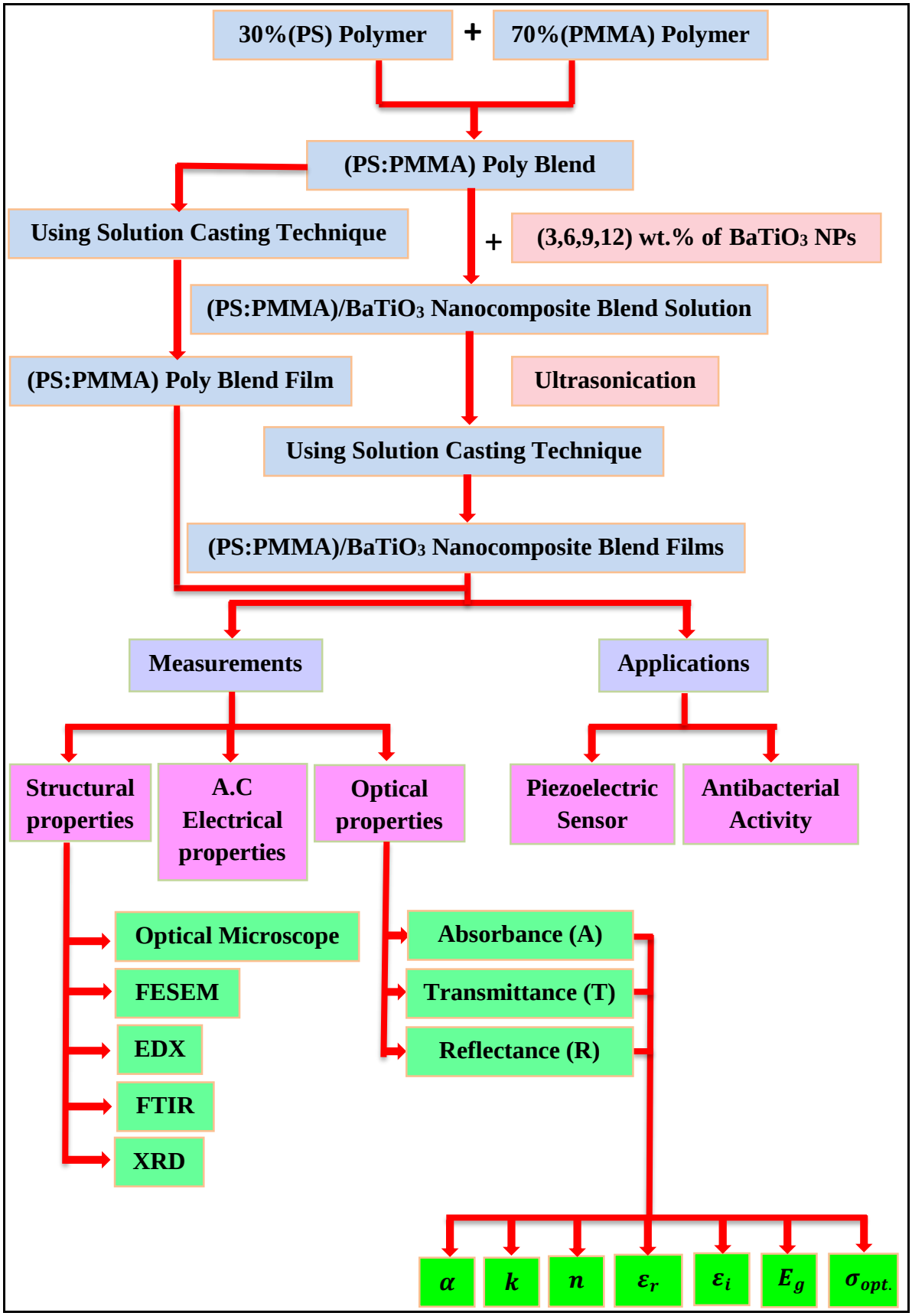

Figure (3.2): Schematic of the main steps for experimental part.

Table (3.1): Weights of materials used for preparing films.

Sample No.	30% PS (g)	70% PMMA (g)	$BaTiO_3$ (g)	$BaTiO_3$ wt.%
1	0.6	1.4	0	0
2	0.582	1.358	0.06	3
3	0.564	1.316	0.12	6
4	0.546	1.274	0.18	9
5	0.528	1.232	0.24	12

3.6 Structural Properties Measurements

The structural properties of the prepared films were studied by optical microscope, Field emission scanning electron microscope (FESEM), Energy dispersive X-ray spectroscopy (EDX), Fourier transform infrared spectroscopy (FTIR), and X-ray diffraction (XRD).

3.6.1 Optical Microscope

(PS:PMMA)/$BaTiO_3$ nanocomposite blend films have been examined by using the optical microscope, which is supplied from Olympus type Nikon - 73346 and equipped with light intensity automatic controlled camera. This instrument is present in University of Babylon, College of Materials Engineering, Ceramics department, XRD Laboratory with magnification power (10X) and (20X).

3.6.2 Field Emission Scanning Electron Microscope (FESEM)

The surface morphology of the prepared films was examined by using field emission scanning electron microscope (Zeiss Ultra-60 FESEM). FESEM system utilized for this work can perform other characterization work like energy dispersive X-ray spectroscopy (EDX) analysis. This instrument is present in Chemical Analysis Center (CAC) / Iran country.

3.6.3 Fourier Transform Infrared Spectroscopy (FTIR)

FTIR spectrum for prepared films were obtained by using FTIR-8400S, SHIMADZU. FTIR spectroscopy in wavenumber range (450-4000) cm^{-1}.

This instrument is present in Chemical Analysis Center (CAC) / Iran country.

3.6.4 X-Ray Diffraction (XRD)

X-ray diffraction (XRD) analysis is used to recognize the crystalline structure of films. When incident beam of X-ray diffracts from a mono wavelength on film surface this will exhibit peaks on limit angles for each material because of Bragg's reflection on parallel crystalline surface. The instrument utilized is X-ray diffractometer type (Shimadzu 6000) made in Japan, the source of radiation is CuK_{α} X-ray emissions at wavelength λ=1.54060 Å. The tube operated at filament current 20 mA and accelerating voltage 30 KV. The scanning angle 2θ is varied in the range (5-80) degree with a speed of (7) deg/min. This instrument is present in the Chemical Analysis Center (CAC) / Najaf Governorate - Iraq country.

3.7 A.C Electrical Conductivity Measurements

In this work, the A.C electrical properties for (PS:PMMA)/$BaTiO_3$ nanocomposite blend films have been calculated by measuring the parallel capacitance (C_p) and loss tangent ($tan\delta$) as a function of frequency of the electric field by using LCR meter type (HIOKI 3532-50 LCR HI TESTER) in the frequency range (100Hz–5MHz) at room temperature as shown in Figure (3.3). This instrument is present in the films laboratory of Physics Department, College of Education for Pure Sciences, University of Babylon.

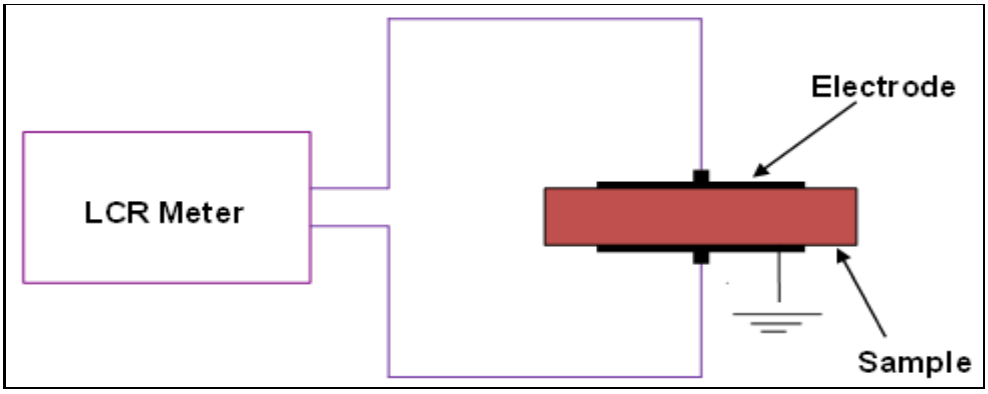

Figure (3.3): Schematic diagram for A.C electrical properties measurement.

3.8 Optical Properties Measurements

Figure (3.4) displays a schematic of optical circuit of an UV-Vis spectrophotometer with a dual-beam function. The broad range radiation absorption spectra were recorded by using UV/1800/Shimadzu spectrophotometer in range of wavelength (200-800) nm. This instrument is present in the Polymer laboratory of Physics Department, College of Science, University of Babylon.

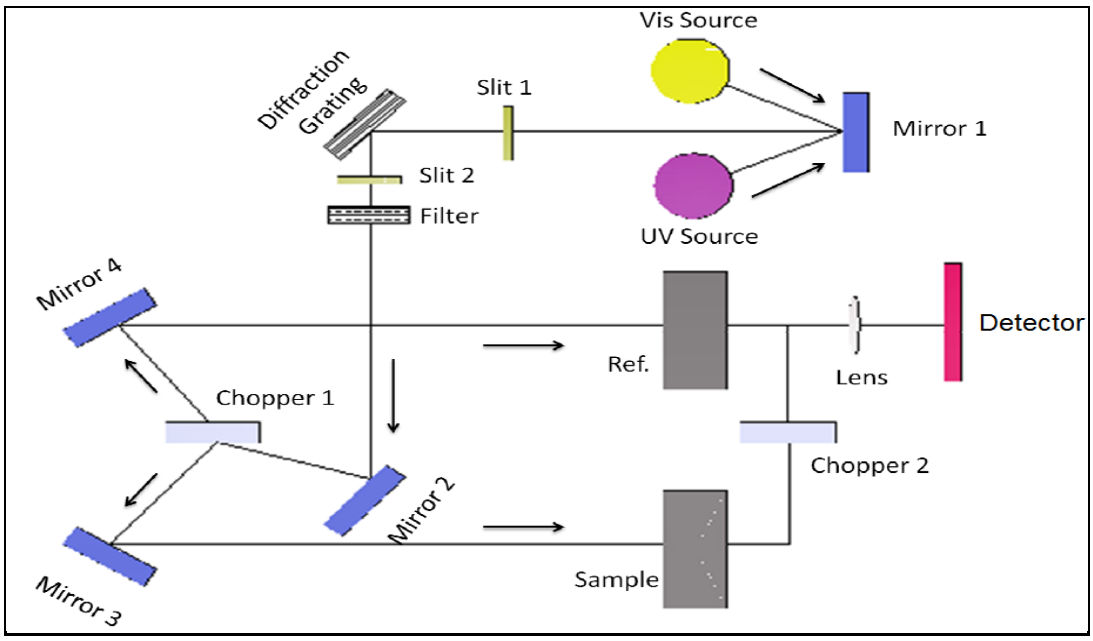

Figure (3.4): Schematic of an optical circuit for an UV-Vis spectrophotometer (dual-beam function).

3.9 Piezoelectric Sensor Application Measurements

In this application, the sample (film) was placed between two copper plate and applied load on the two plate. The electrical resistance for different applied load in the range (80-160) bar was measured by using Keithley electrometer type 2400 as in the Figure (3.5) which shows the schematic diagram of piezoelectric sensor measurement system which locally manufactured. This instrument is present in the Physics Department, College of Education for Pure Sciences, University of Babylon.

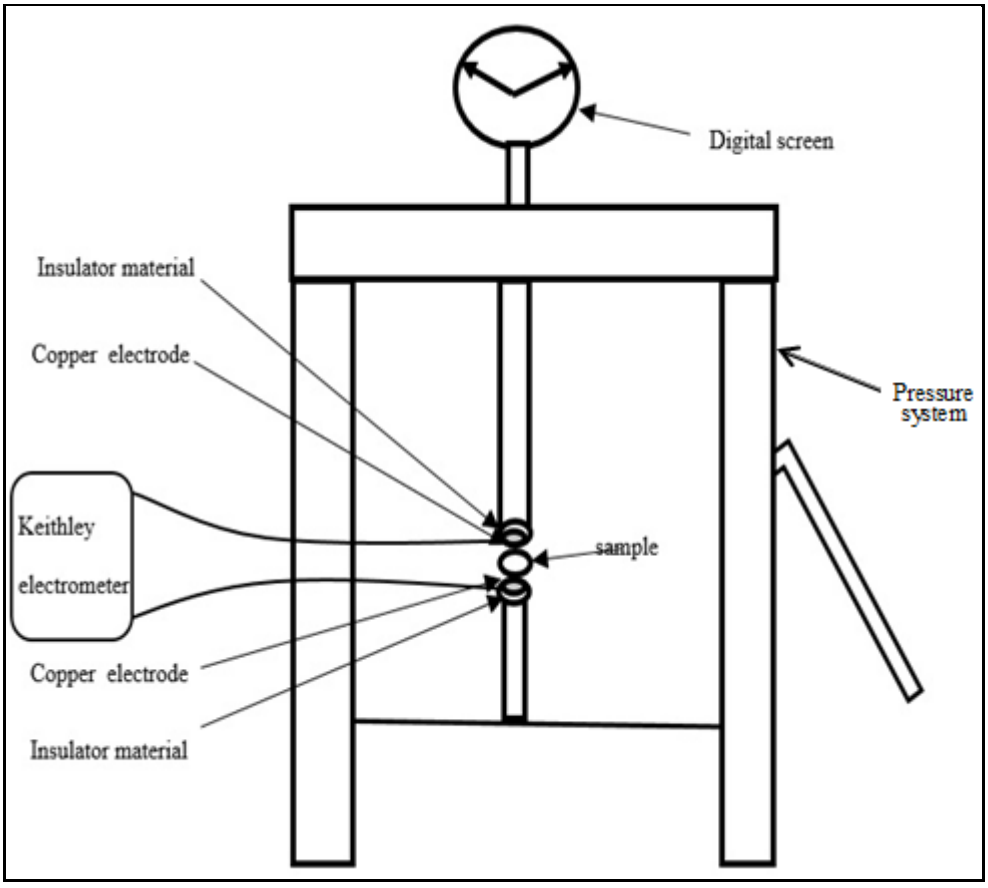

Figure (3.5): Schematic diagram of locally designed piezoelectric sensor measurement system.

3.10 Antibacterial Activity Application Measurements

3.10.1 Preparation of Media

Mueller Hinton agar (MHA) media were prepared in distilled water and all components were dissolved by the microwave oven to dissolve fully. The medium were sterilized at 121˚C for 15 minutes and then stored under a sterile environment at room temperature for subsequent use.

3.10.2 Preparation of Bacteria

The first step of the present work was obtaining different microorganism and testing the resistance of (PS:PMMA)/$BaTiO_3$ nanocomposite blend films against four microorganisms namely; Staphylococcus aureus and Enterococcus faecalis as gram positive bacteria, Enterobacter cloacae and Escherichia coli as gram negative bacteria. Figure (3.6) shows images for the tested bacteria types.

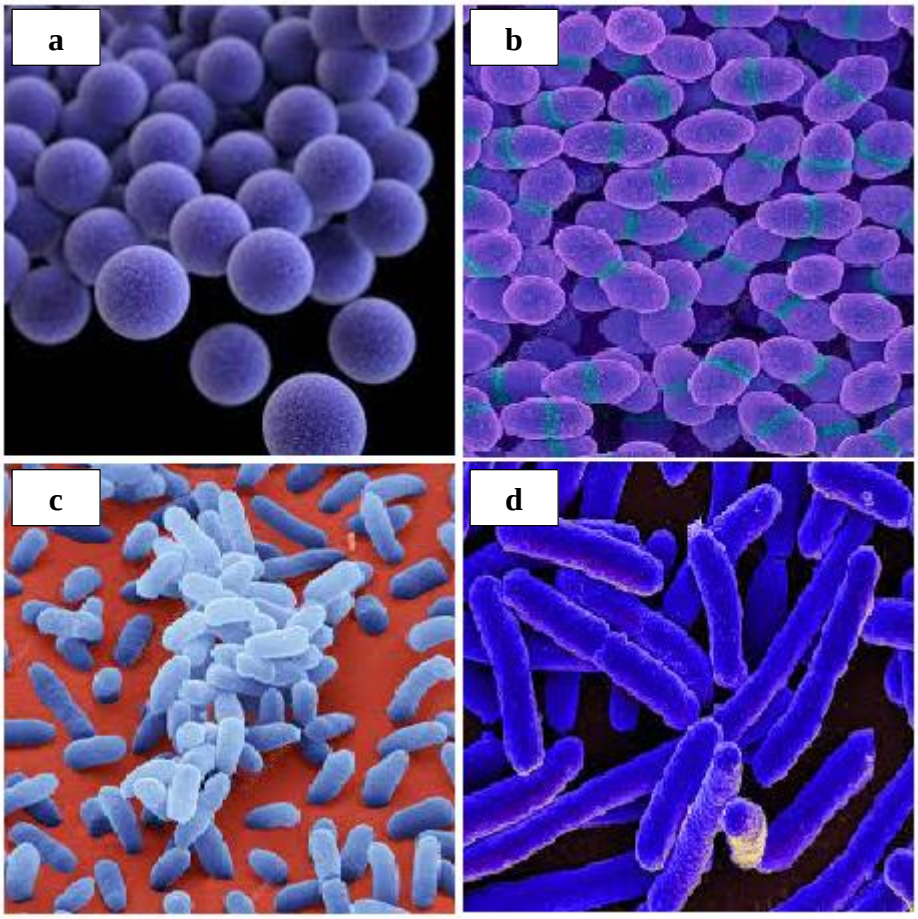

Figure (3.6): Images for (a) Staphylococcus aureus (b) Enterococcus faecalis (c) Enterobacter cloacae (d) Escherichia coli.

3.10.3 Preparation of McFarland 0.5 Standard

The (PS:PMMA)/$BaTiO_3$ nanocomposite blend films were tested to evaluate their antibacterial activity against four different types of clinical bacteria; Staphylococcus aureus and Enterococcus faecalis as gram positive bacteria, Enterobacter cloacae and Escherichia coli as gram negative bacteria by using well diffusion method. Standardized suspension of each tested bacteria ($5x10^8$ CFU/mL) by Dense Check standard (0.5) (Figure (3.7)) (Turbidity levels of bacterial suspension were equated in accordance with the turbidity of 0.5 McFarland turbidity standards) was swabbed separately onto MHA plates using sterile cotton swabs. The accuracy of bacterial suspension was confirmed using a spectrophotometer. Sterile MHA was used and measured at a wavelength of 625 nm as a blank solution for

comparison. Absorbance values were used in the range of 0.08 to 0.10, which were associated with 10^7 to 10^8 number of bacteria per mL of MHA.

Figure (3.7): Dense check.

The sterile discs approximately 15mm in diameter was then placed over the swabbed MHA plates. Incubation occurred at 37˚C for 24 hour so as to grow the bacteria. Antibacterial activity has been recorded through the measurement of the inhibition zone diameter (mm). This work done in Al-Ameen Center for Researches and Advanced Biotechnologies / Najaf Governorate - Iraq country.

4.1 Introduction

This chapter involves the results of structural, A.C electrical, and optical measurements for (PS:PMMA) poly blend and (PS:PMMA)/$BaTiO_3$ nanocomposite blend and discussions. Beside that discuss each of the piezoelectric sensor and antibacterial activity applications for (PS:PMMA)/$BaTiO_3$ nanocomposite blend.

4.2 Structural Properties

Several characterization techniques have been employed to investigate, observe, and confirm the morphology, composition, crystalline phase, and lattice parameters of the prepared films. The morphological properties and particles distribution study was carried out using FESEM. The purity and the surface functionality of the prepared films has been evaluated by FTIR. Crystalline structure of the prepared films were studied by XRD which provided a macroscopic analysis of the phase of crystalline products.

4.2.1 Optical Microscope

Figures (4.1) and (4.2) shows the cross sectional photomicrographs of (PS:PMMA) poly blend and (PS:PMMA)/$BaTiO_3$ nanocomposite blend at magnification power (10X) and (20X). It can be found that the (PS:PMMA) poly blend and the $BaTiO_3$ nanoparticles can be clearly distinct in the nanocomposites. The $BaTiO_3$ nanoparticles shows an annularly interconnected network in the (PS:PMMA) poly blend matrix, which is due to the fillers sponge shape, and it can be deduced that $BaTiO_3$ nanoparticles has a regular three dimensional filling fashion in the poly blend matrix. From the detailed photomicrographs in the Figures (4.1b-e) and (4.2b-e), good contacts between the $BaTiO_3$ nanoparticles structure and poly blend matrix without evident cracks and pores are observed, which indicates that liquid (PS:PMMA) poly blend has filled completely the interspace of $BaTiO_3$ nanoparticles sponges. These results are in agreement with [101].

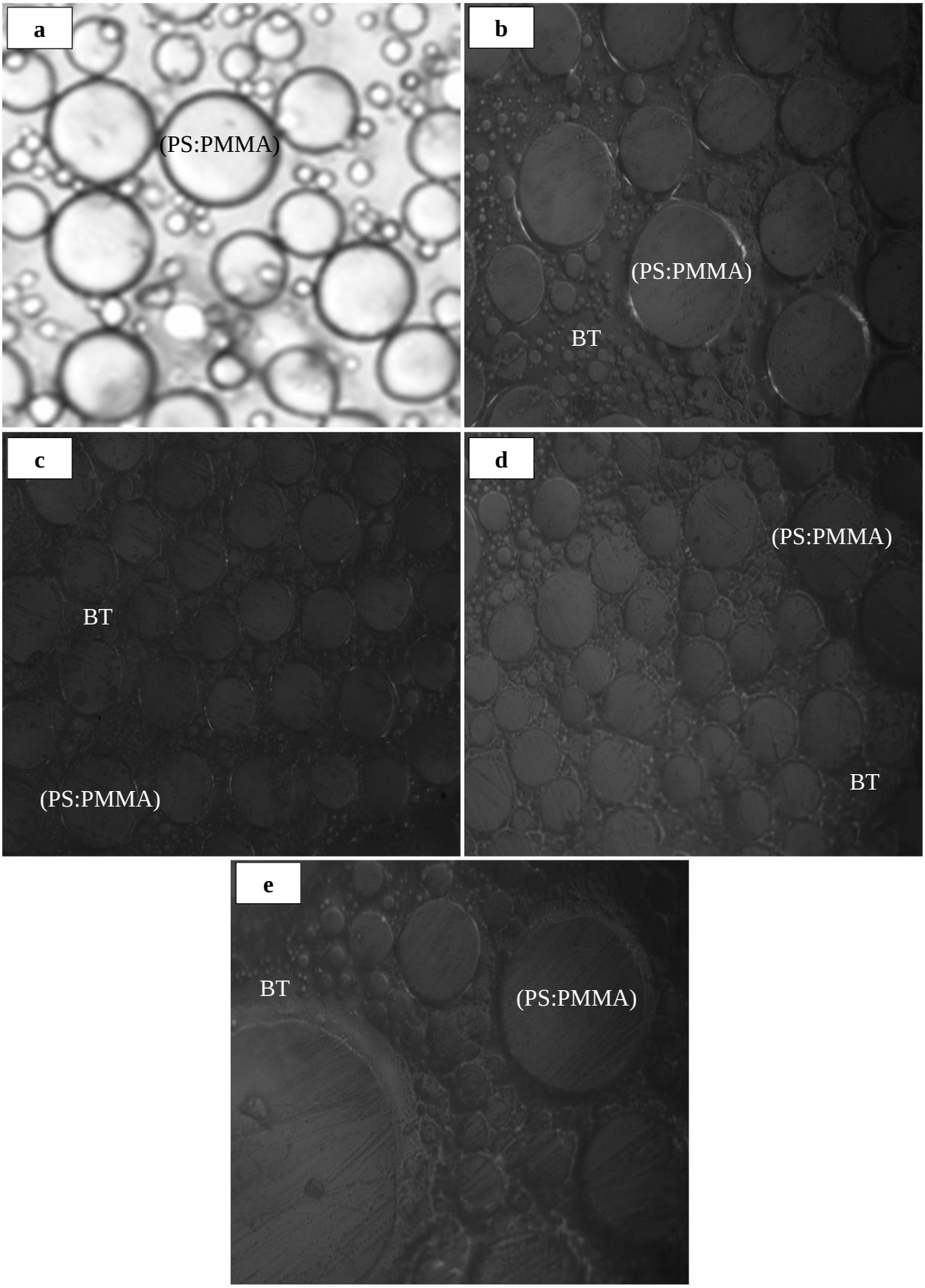

Figure (4.1): Photomicrographs for (PS:PMMA)/$BaTiO_3$ nanocomposite blend at (10X): (a) for pure (b) for 3wt.% $BaTiO_3$ NPs (c) for 6wt.% $BaTiO_3$ NPs (d) for 9wt.% $BaTiO_3$ NPs (e) for 12wt.% $BaTiO_3$ NPs.

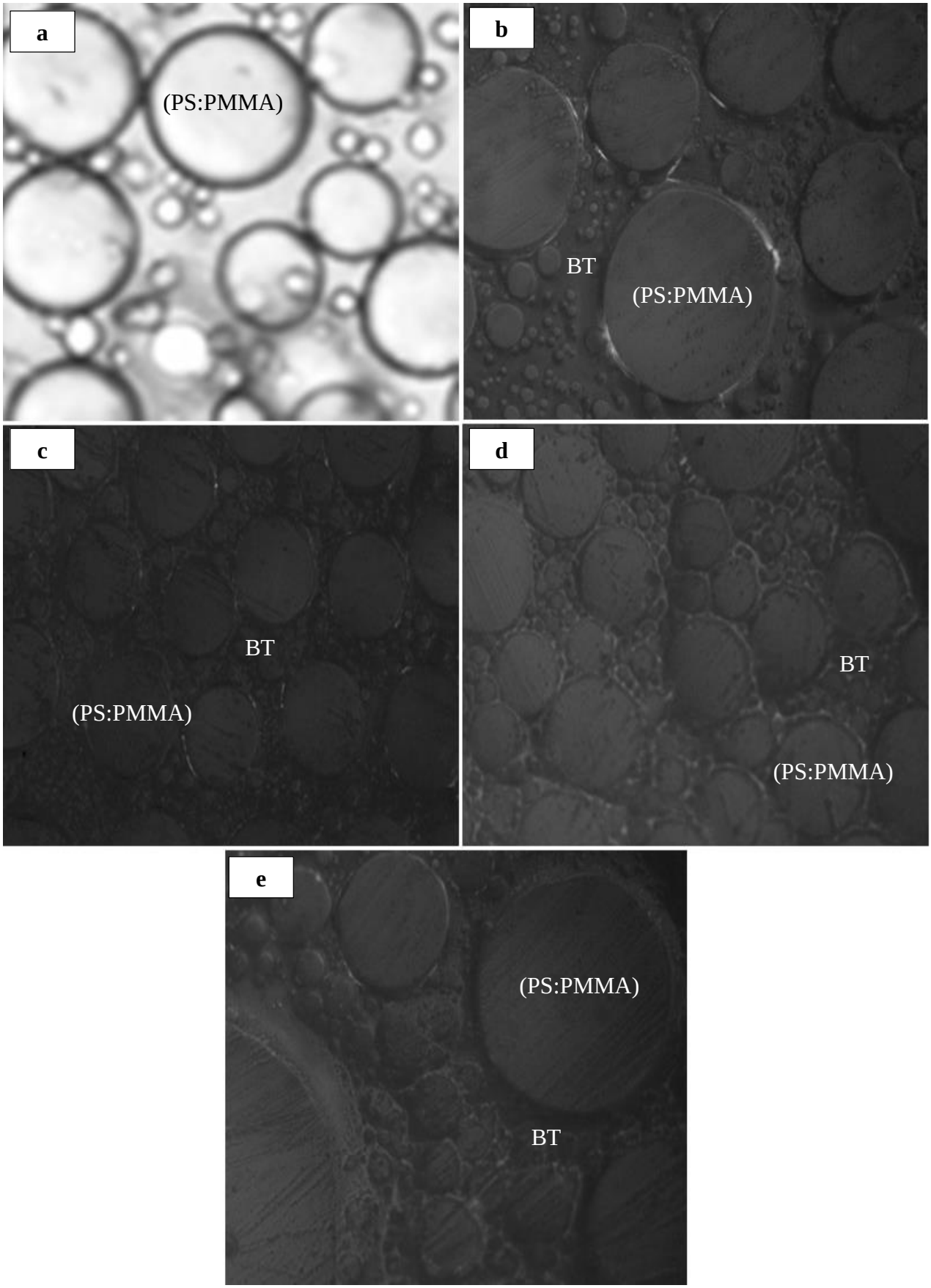

Figure (4.2): Photomicrographs for (PS:PMMA)/$BaTiO_3$ nanocomposite blend at (20X): (a) for pure (b) for 3wt.% $BaTiO_3$ NPs (c) for 6wt.% $BaTiO_3$ NPs (d) for 9wt.% $BaTiO_3$ NPs (e) for 12wt.% $BaTiO_3$ NPs.

4.2.2 Field Emission Scanning Electron Microscope (FESEM) Analysis

The morphological and microstructural properties for (PS:PMMA)/$BaTiO_3$ nanocomposite blend for pure and different weight ratios of $BaTiO_3$ nanoparticles were examined by FESEM as shown in Figure (4.3) which exhibited different morphologies. For (PS:PMMA) poly blend for pure and low weight ratio (3,6)% of $BaTiO_3$ nanoparticles in (PS:PMMA)/$BaTiO_3$ nanocomposite blend, the specimens consisted of plate-like grains with a random orientation of plate faces because of their highly anisotropic crystal structure, where they were aggregated and formed predominantly dense and irregular sharped plates. In addition, the microstructure showed a round stick shape where the $BaTiO_3$ nanoparticles were approximately spherical. But at high weight ratio (9,12)% of $BaTiO_3$ nanoparticles in (PS:PMMA)/$BaTiO_3$ nanocomposite blend, these nanoparticles forms as interconnected network of nanofibrilar morphology and these nanofibers well dispersed inside the (PS:PMMA) poly blend. This network has paths where charge carriers are allowed to pass through the paths that have low electrical resistance. These results are in agreement with [102,103].

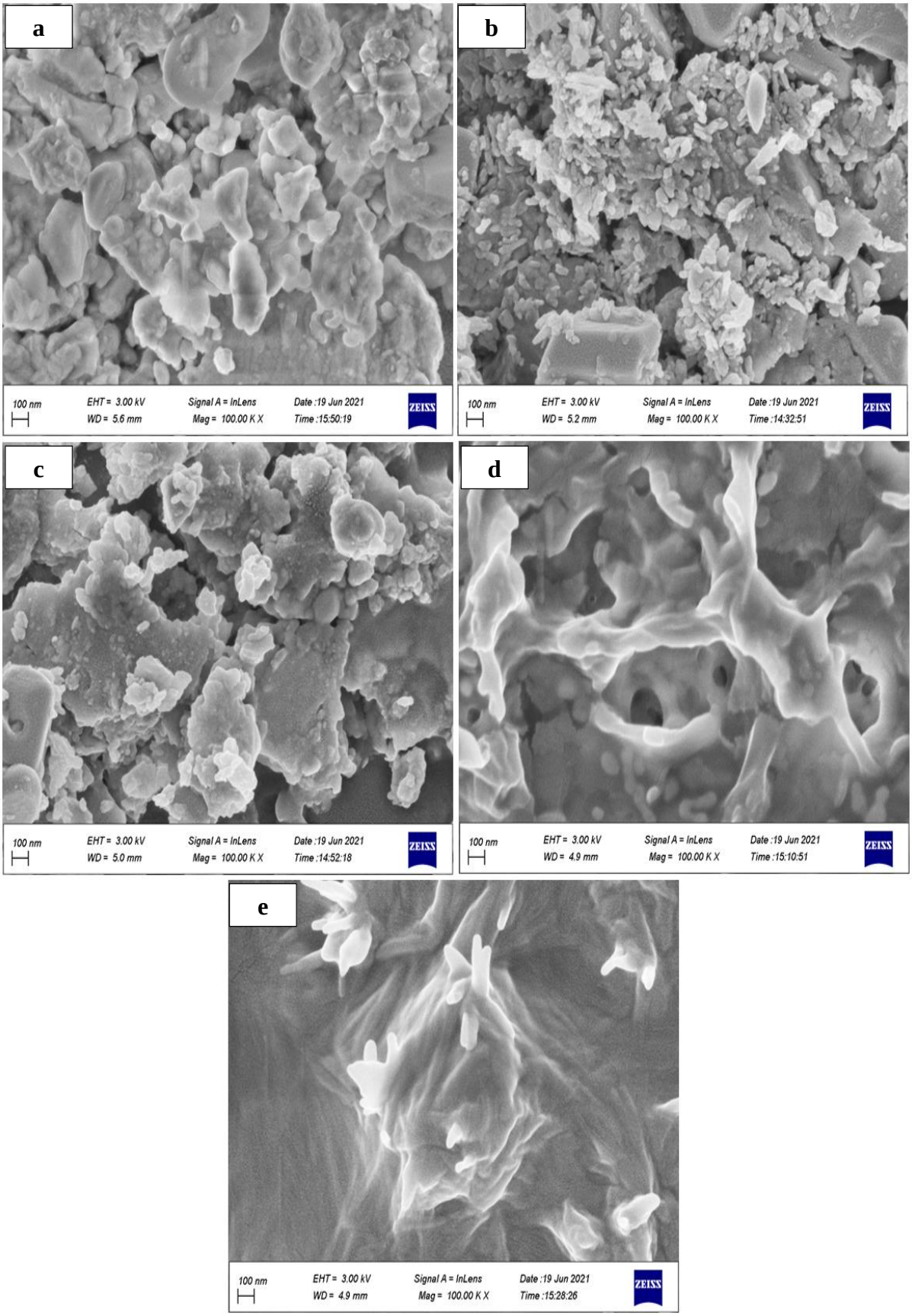

Figure (4.3): FESEM images for (PS:PMMA)/$BaTiO_3$ nanocomposite blend at (100KX): (a) for pure (b) for 3wt.% $BaTiO_3$ NPs (c) for 6wt.% $BaTiO_3$ NPs (d) for 9wt.% $BaTiO_3$ NPs (e) for 12wt.% $BaTiO_3$ NPs.

4.2.3 Fourier Transform Infrared Spectroscopy (FTIR) Analysis

FTIR is employed to explore and identify the vibrational bands for prepared films. FTIR spectrum analysis was performed to investigate the structure and functional groups of the materials, as shown in Figure (4.4) which shows FTIR spectrum for (PS:PMMA)poly blend, and Figures (4.5-4.8) which shows FTIR spectrum for (PS:PMMA)/$BaTiO_3$ nanocomposite blend for weight ratios (3,6,9,12)% of $BaTiO_3$ nanoparticles respectively.

For all prepared films, the vibrational bands associated with bending of C-H bonds are registered in the (700-1000) cm^{-1} spectral range. The vibrational bands located in the (1000-1300) cm^{-1} range are assigned to C-O stretching. The vibrational bands recorded at 1457 cm^{-1} could be ascribed to the -CH_2 bending. Band at 1582 cm^{-1} could be ascribed to the C=C bonds. The bands appearing between (1600-1800) cm^{-1} are associated with C=O bond of the ester carbonyl group for PS and PMMA. Bands identified between (2800-3200) cm^{-1} are allocated to the C-H stretching. These results are in agreement with [26].

The peaks at 760 and 842 cm^{-1} are attributed to the puckering vibrations and deformation vibrations of O-C-O in PMMA, respectively. These results are in agreement with [104].

The broad peak ranging from 1029 to 1234cm^{-1} can be explained owing to the C-O (ester bond) stretching vibration. These results are in agreement with [105].

The peaks at 2956 cm^{-1} and 2846 cm^{-1}, respectively emanate from the presence of CH_2 asymmetric and symmetric stretching vibrations of the methylene group. These results are in agreement with [106].

The wide spectral range identifies the locations of different IR bands in the nanocomposite films. Finally, the peak appearing at 494.75cm^{-1} characterizes the stretching vibration of Ti-O bond suggesting homogenous

incorporation of $BaTiO_3$ nanoparticles into the copolymer's matrices. These results are in agreement with [107].

The two main factors that influence the intensity of an IR absorption band are the intermolecular bonding between (PS:PMMA) poly blend and $BaTiO_3$ nanoparticles as well as the dipole moment changes due to the vibrations of atoms [26].

Furthermore, significant changes observed in width and intensity of the vibrational bands of (PS:PMMA) poly blend upon addition of $BaTiO_3$ nanoparticles indicate the strong influence of $BaTiO_3$ nanoparticles on the spectroscopy of the blended polymer [26]. Table (4.1) presents the peak positions of all major vibrational bands of (PS:PMMA) poly blend doped by $BaTiO_3$ nanoparticles.

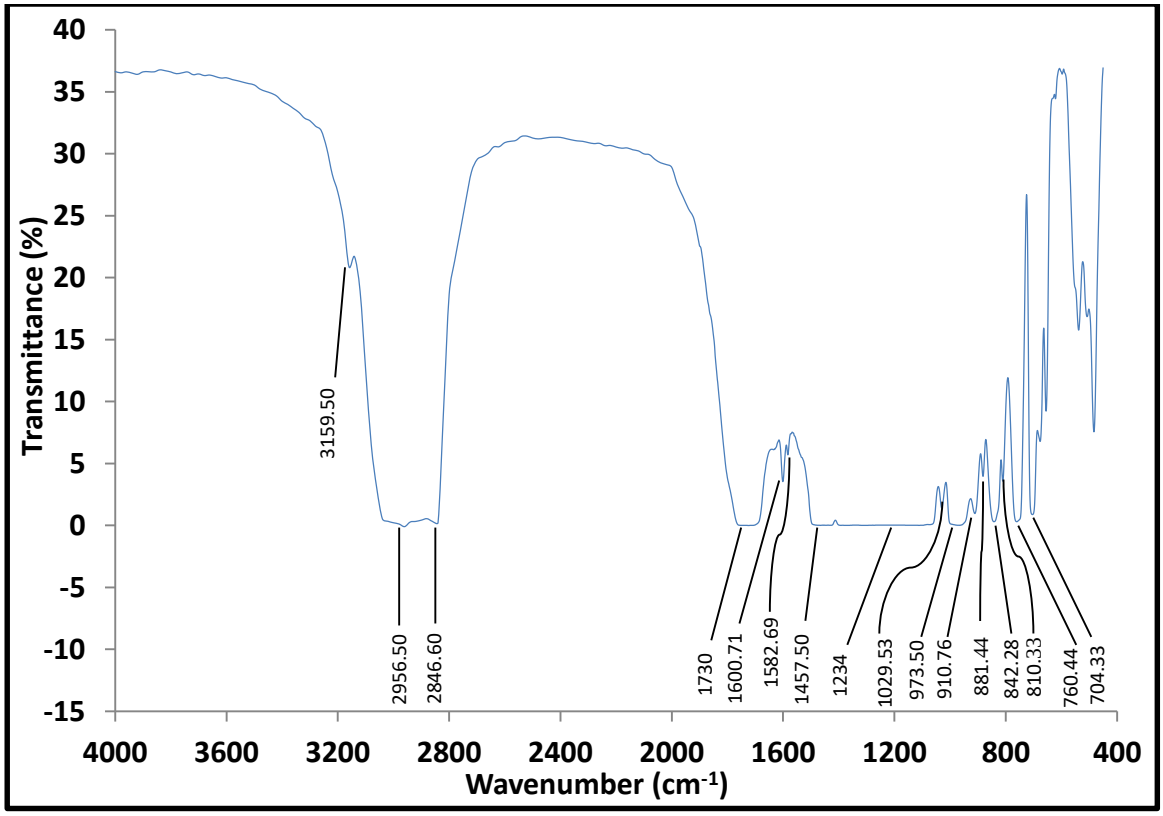

Figure (4.4): FTIR spectrum for (PS:PMMA) poly blend.

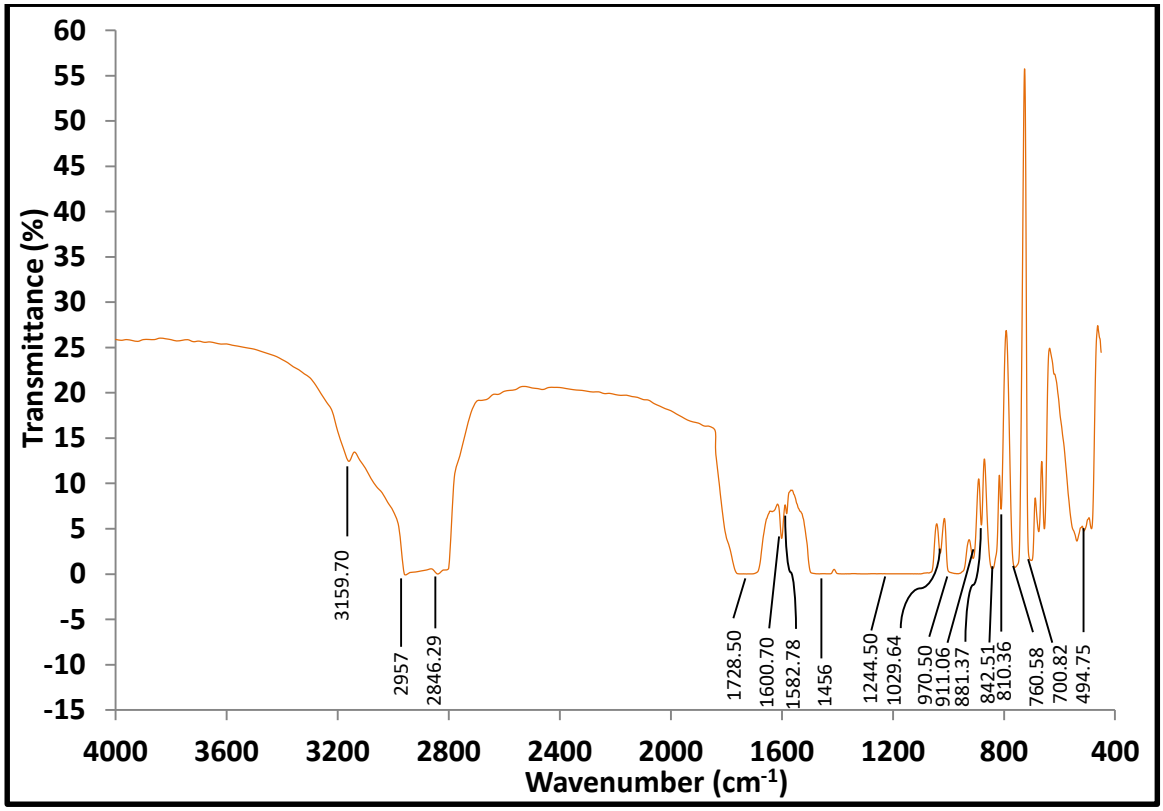

Figure (4.5): FTIR spectrum for (PS:PMMA)/$BaTiO_3$ nanocomposite blend for 3wt.% of $BaTiO_3$ NPs.

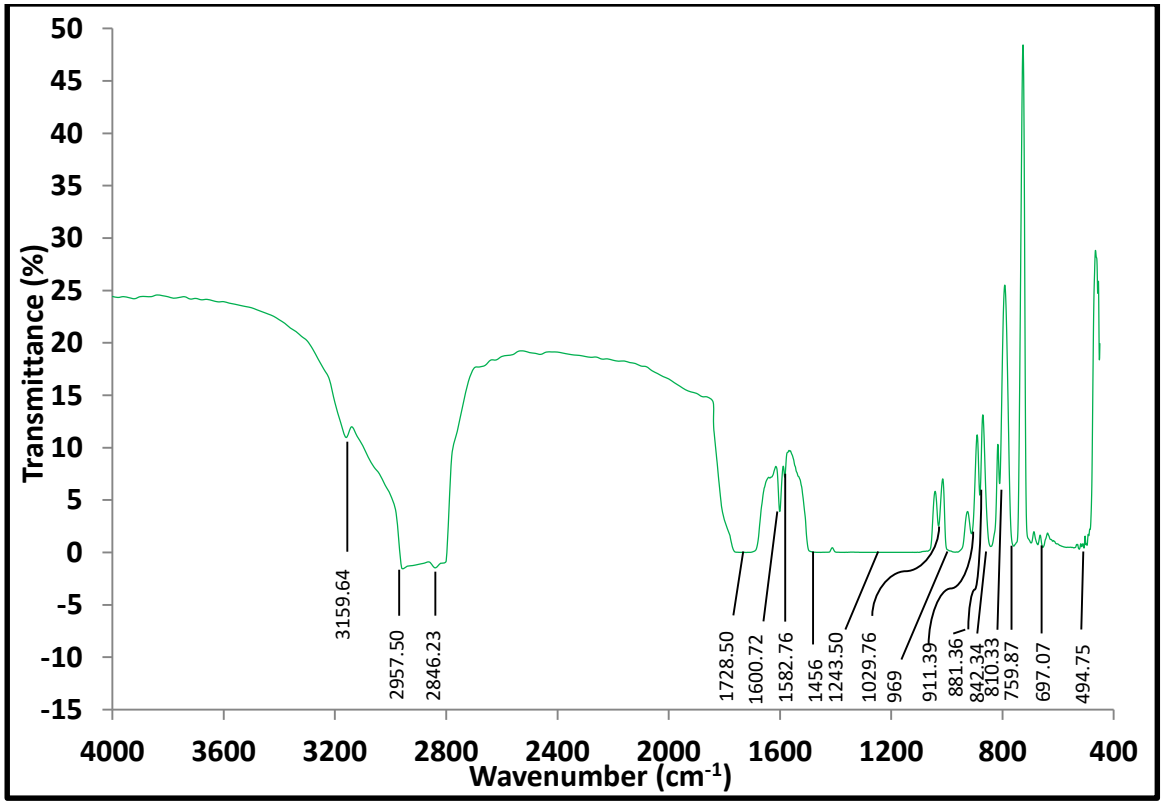

Figure (4.6): FTIR spectrum for (PS:PMMA)/$BaTiO_3$ nanocomposite blend for 6wt.% of $BaTiO_3$ NPs.

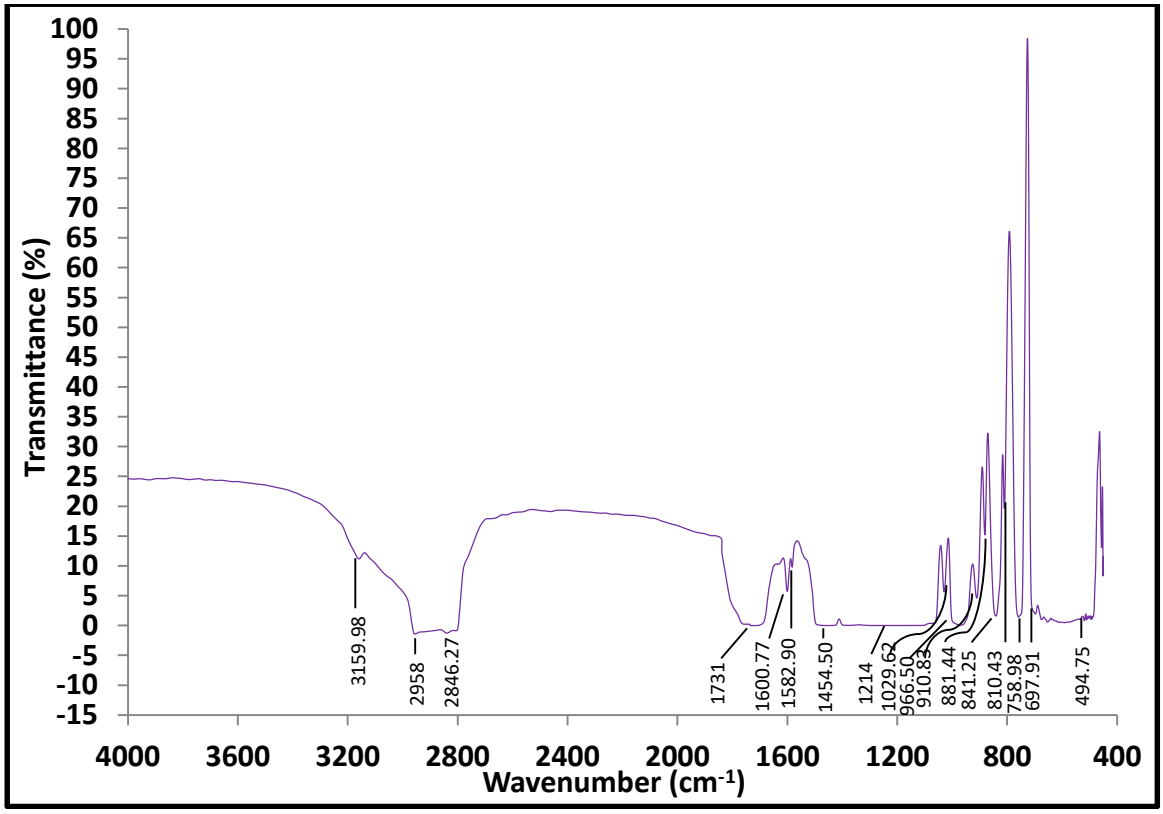

Figure (4.7): FTIR spectrum for (PS:PMMA)/$BaTiO_3$ nanocomposite blend for 9wt.% of $BaTiO_3$ NPs.

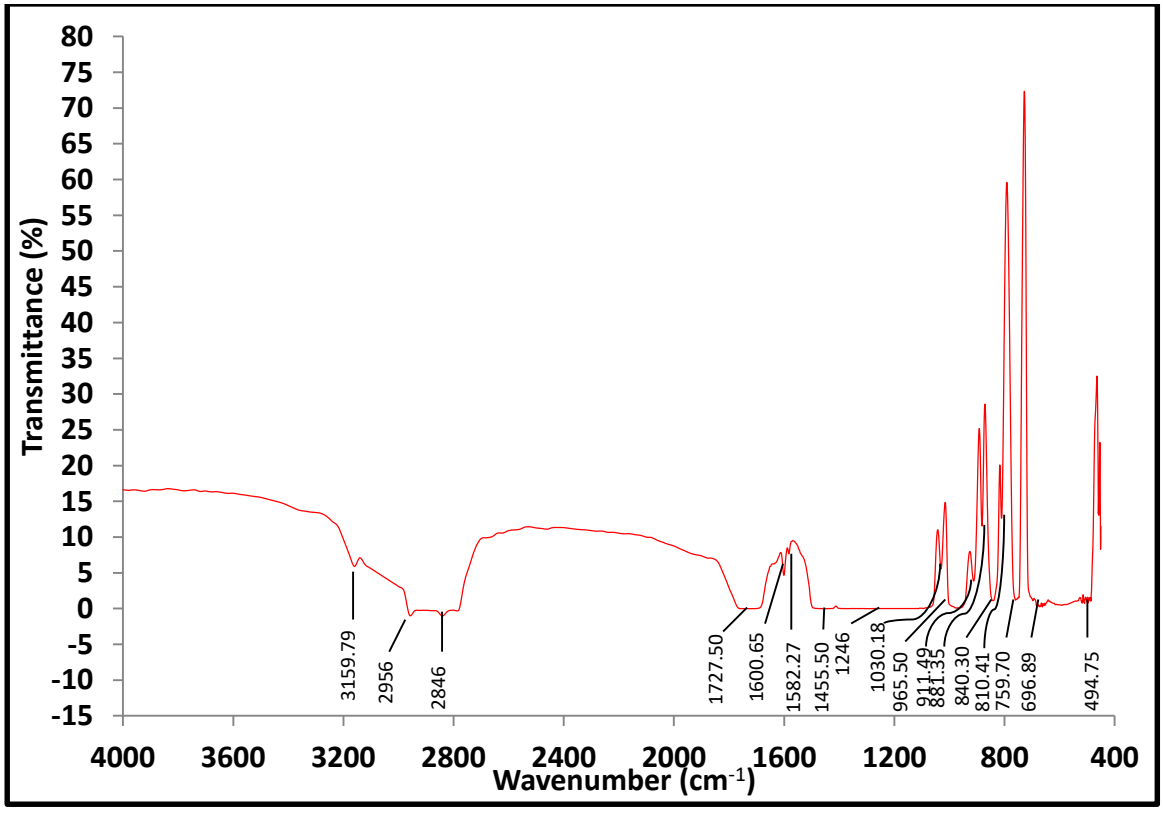

Figure (4.8): FTIR spectrum for (PS:PMMA)/$BaTiO_3$ nanocomposite blend for 12wt.% of $BaTiO_3$ NPs.

Table (4.1): The peak positions of all vibrational bands for the prepared films.

Vibrational Band	PS:PMMA	PS:PMMA/ $BaTiO_3$ 3wt.%	PS:PMMA/ $BaTiO_3$ 6wt.%	PS:PMMA/ $BaTiO_3$ 9wt.%	PS:PMMA/ $BaTiO_3$ 12wt.%
Ti-O stretching	-	494.75	494.75	494.75	494.75
C-H bending	704.33 760.44 810.33 842.28 881.44 910.76 973.50	700.82 760.58 810.36 842.51 881.37 911.06 970.50	697.07 759.87 810.33 842.34 881.36 911.39 969	697.91 758.98 810.43 841.25 881.44 910.83 966.50	696.89 759.70 810.41 840.30 881.35 911.49 965.50
C-O stretching	1029.53 1234	1029.64 1244.50	1029.76 1243.50	1029.62 1214	1030.18 1246
$-CH_2$ bending	1457.50	1456	1456	1454.50	1455.50
C=C stretching	1582.69	1582.78	1582.76	1582.90	1582.27
C=O Stretching	1600.71 1730	1600.70 1728.50	1600.72 1728.50	1600.77 1731	1600.65 1727.50
C-H stretching	2846.60 2956.50 3159.50	2846.29 2957 3159.70	2846.23 2957.50 3159.64	2846.27 2958 3159.98	2846 2956 3159.79

4.2.4 X-Ray Diffraction (XRD) Analysis

The structure and phase purity of the prepared films were confirmed by analyzing the observed X-ray diffraction patterns. XRD pattern for (PS:PMMA) poly blend shown in Figure (4.9) exhibits a characteristic broad amorphous hump observed around $2\theta = 28.866^{\circ}$ corresponding to the (011) crystallographic plane which indicated that the (PS:PMMA) poly blend have amorphous structure validated by the lack of sharp peaks and the occurrence of broad peak. These results are in agreement with [108].

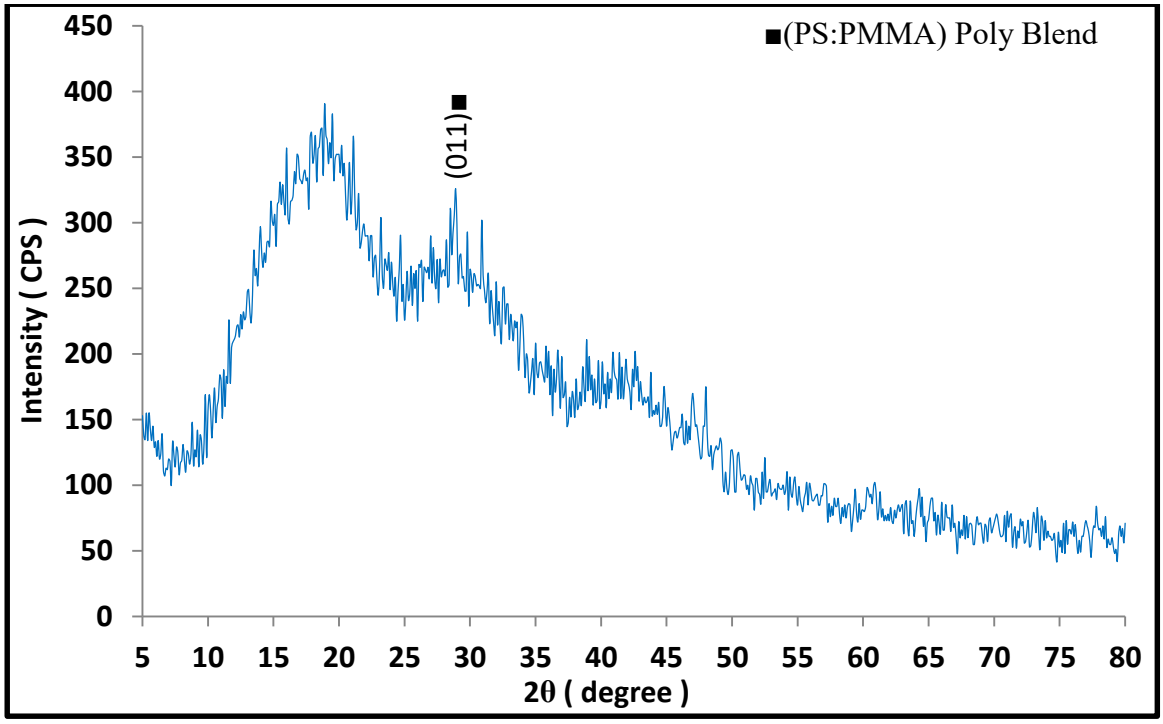

Figure (4.9): XRD pattern for (PS:PMMA) poly blend.

From the Figures (4.10-4.13) which shows XRD patterns for (PS:PMMA)/$BaTiO_3$ nanocomposite blend for weight ratios (3,6,9,12)% of $BaTiO_3$ nanoparticles respectively we can understood that the formed single crystalline phase belong to cubic perovskite structure of $BaTiO_3$. This phase are in consistent with standard (JCPDS card No.31-174) for cubic $BaTiO_3$ nanoparticles with unit cell parameters $a = 4.031$Å and $\alpha = 90^{\circ}$. This phase are indexed with miller indices (hkl) and compared with standard JCPDS data as shown in the mentioned Figures where we notice that there is small shift have been happened to the diffraction patterns after increasing the weight ratio of $BaTiO_3$ nanoparticles, this shift due to the change in the *d* spacing value of the corresponding planes, also the intensity of diffracted X-ray photons from nanocomposite films has been increase with the increasing of the weight ratio of $BaTiO_3$ nanoparticles and this due to increasing the number of $BaTiO_3$ nanoparticles layers after doping process.

The diffraction patterns refers that the nanocomposites is polycrystalline structures, sharp and strong peaks indicate that the nanocomposites has crystallized well. These results are in agreement with [109-111].

By calculating (θ) values for each diffraction peak, we can calculate d-spacing using Bragg's law (equation (2.2)) as shown in Table (4.2). The crystallite size (Z) is calculated using the Debye Scherer formula (equation (2.3)).

It can be conclude that the values of 2θ =28.866˚,29.161˚, 28.923˚ in Figures (4.9-4.11) for (PS:PMMA) poly blend for pure and weight ratio (3,6)% of $BaTiO_3$ nanoparticles respectively refers to the (PS:PMMA) poly blend and these values are vanished at weight ratio (9,12)% of $BaTiO_3$ nanoparticles in Figures (4.12,4.13) due to the change in crystallinity with presence of $BaTiO_3$ nanoparticles additive (i.e. $BaTiO_3$ have crystal structure) where $BaTiO_3$ nanoparticles is the dominate is the dominate on the (PS:PMMA) poly blend in the XRD patterns at the high weight ratio from it.

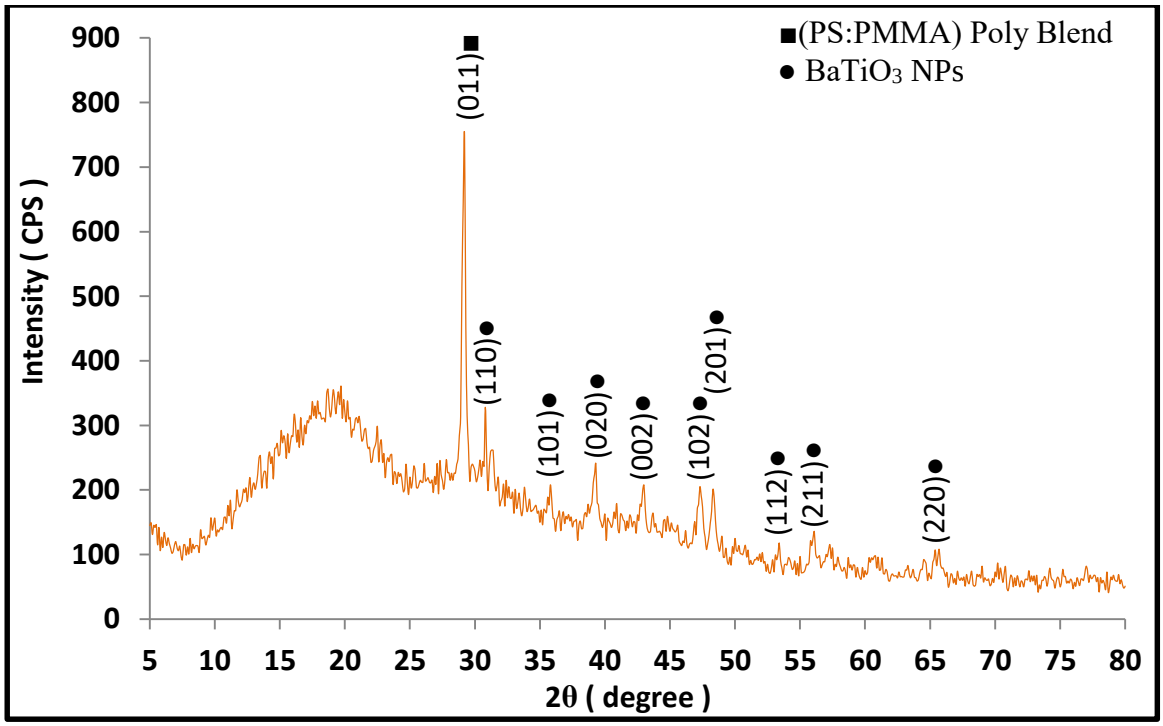

Figure (4.10): XRD pattern for (PS:PMMA)/$BaTiO_3$ nanocomposite blend for 3wt.% of $BaTiO_3$ NPs.

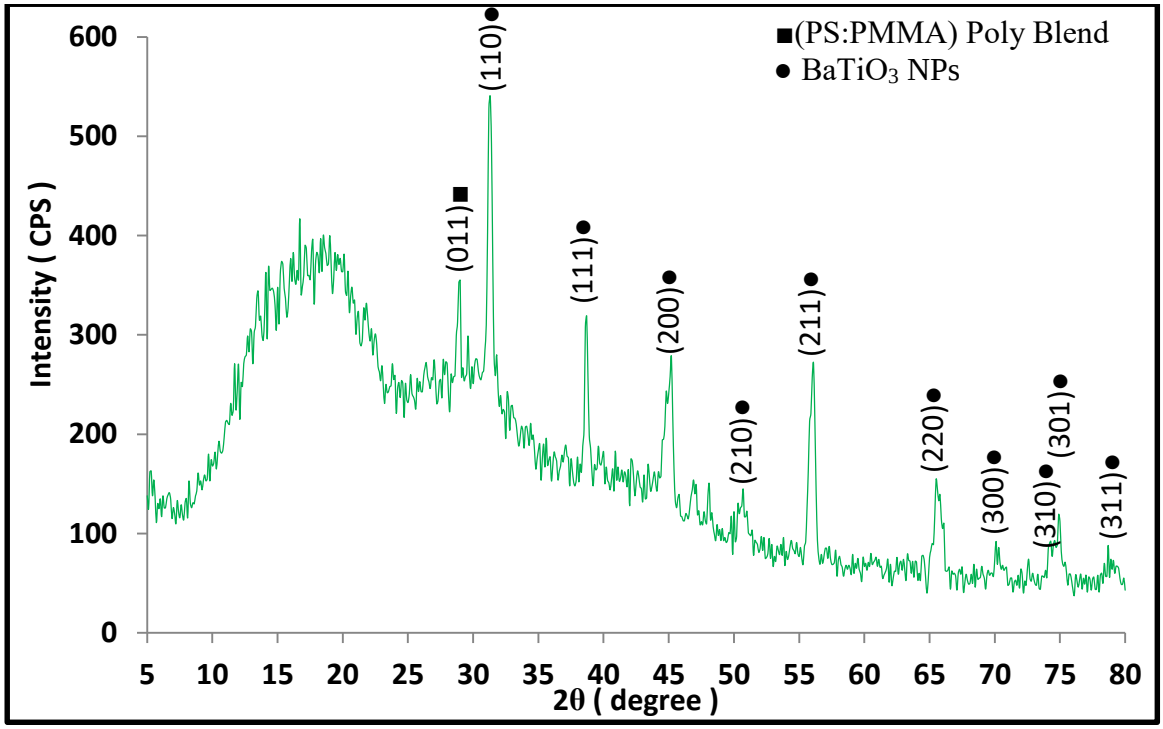

Figure (4.11): XRD pattern for (PS:PMMA)/$BaTiO_3$ nanocomposite blend for 6wt.% of $BaTiO_3$ NPs.

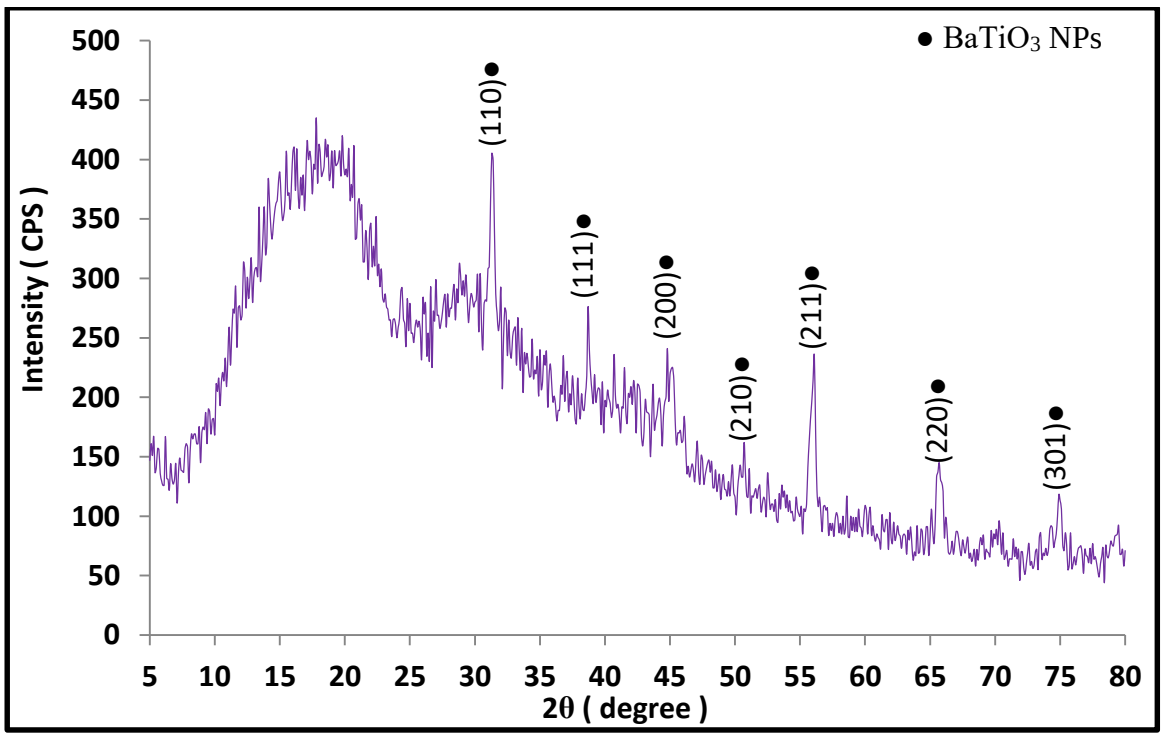

Figure (4.12): XRD pattern for (PS:PMMA)/$BaTiO_3$ nanocomposite blend for 9wt.% of $BaTiO_3$ NPs.

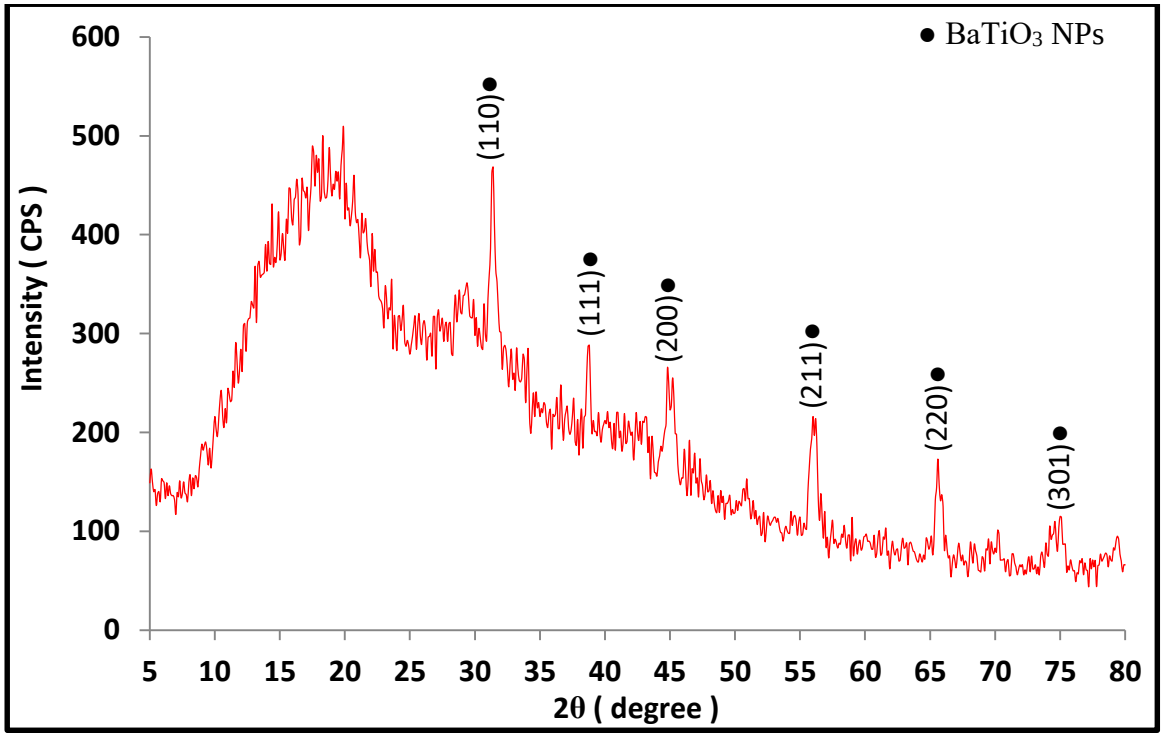

Figure (4.13): XRD pattern for (PS:PMMA)/$BaTiO_3$ nanocomposite blend for 12wt.% of $BaTiO_3$ NPs.

Table (4.2): XRD parameters for the prepared films.

$BaTiO_3$ wt.%	(hkl)	2θ (deg.)	θ (deg.)	$d_{Exp.}$ (nm)	d_{JCPDS} (nm)	FWHM (rad)	*Z* (nm)
0	(011)	28.866	14.433	0.30904	0.30905	0.004224	33.89954
3	(011)	29.161	14.5805	0.30598	0.30599	0.004869	29.42218
	(110)	30.787	15.3935	0.29018	0.29019	0.004887	29.42867
	(101)	35.762	17.881	0.25087	0.25087	0.00288	50.59178
	(020)	39.263	19.6315	0.22927	0.22927	0.006981	21.08677
	(002)	42.949	21.4745	0.21041	0.21041	0.003473	42.8998
	(102)	47.303	23.6515	0.19201	0.19201	0.005253	28.81371
	(201)	48.321	24.1605	0.1882	0.18820	0.004695	32.36857
	(112)	53.358	26.679	0.17156	0.17156	0.003334	46.5497
	(211)	56.049	28.0245	0.16394	0.16394	0.005323	29.50709
	(220)	65.687	32.8435	0.14203	0.14203	0.005742	28.74134
6	(011)	28.923	14.4615	0.30844	0.30845	0.004084	35.06142
	(110)	31.294	15.647	0.2856	0.28560	0.006545	22.00043
	(111)	38.685	19.3425	0.23256	0.23256	0.004433	33.14829
	(200)	45.164	22.582	0.20059	0.20059	0.008918	16.83775
	(210)	50.684	25.342	0.17996	0.17996	0.006894	22.25398
	(211)	56.071	28.0355	0.16388	0.16388	0.007068	22.22366
	(220)	65.536	32.768	0.14232	0.14232	0.009233	17.85987
	(300)	70.157	35.0785	0.13403	0.13403	0.005463	31.01492
	(310)	74.29	37.145	0.12757	0.12756	0.014207	12.2439
	(301)	74.909	37.4545	0.12666	0.12666	0.010227	17.07787
	(311)	78.743	39.3715	0.12143	0.12143	0.00726	24.70369
9	(110)	31.322	15.661	0.28535	0.28535	0.005725	25.15465
	(111)	38.731	19.3655	0.2323	0.23230	0.003648	40.29116
	(200)	44.839	22.4195	0.20197	0.20197	0.004485	33.43964
	(210)	50.682	25.341	0.17997	0.17997	0.002827	54.26081
	(211)	56.056	28.028	0.16392	0.16392	0.007226	21.73902
	(220)	65.695	32.8475	0.14201	0.14201	0.007348	22.46158
	(301)	74.932	37.466	0.12663	0.12663	0.007749	22.54317
12	(110)	31.388	15.694	0.28477	0.28476	0.00761	18.92257
	(111)	38.737	19.3685	0.23226	0.23226	0.005061	29.03796
	(200)	45.189	22.5945	0.20049	0.20049	0.010507	14.29381
	(211)	56.014	28.007	0.16404	0.16404	0.010262	15.30306
	(220)	65.602	32.801	0.14219	0.14219	0.008447	19.52764
	(301)	75.031	37.5155	0.12649	0.12649	0.008255	21.17506

4.3 A.C Electrical Properties

A.C Electrical properties for (PS:PMMA)/$BaTiO_3$ nanocomposite blend are involved dielectric constant, dielectric loss, and A.C electrical conductivity were studied in the frequency range (100Hz–5MHz) at room temperature.

4.3.1 Dielectric Constant

The dielectric constant can be calculated by the equation (2.4). Figure (4.14) shows the variation of dielectric constant for (PS:PMMA) poly blend and (PS:PMMA)/$BaTiO_3$ nanocomposite blend for weight ratios (3,6,9,12)% of $BaTiO_3$ nanoparticles respectively versus frequency at room temperature. At low frequencies, (PS:PMMA)/$BaTiO_3$ nanocomposite blend exhibited high dielectric constant which decrease with increasing in frequency. This shows different polarization mechanisms in the low and high frequency ranges. In dielectric analysis, dielectric constant at high frequencies is associated with dipolar relaxation and at low frequencies, the dielectric constant is associated with interfacial polarization and DC conductivity [112]. The increase in the dielectric constant at low frequencies reveals that system exhibits strong interfacial polymerization. Interfacial polarization occurs when there is an accumulation of charge between the two conductive and insulating regions within the material when electric field is applied [113]. This interfacial polarization is particularly dominant at low frequencies and in conjugated polymers. At high frequencies, the variation in the field is very rapid for the dipoles to align themselves hence results in less dielectric constant. These results are in agreement with [114-119].

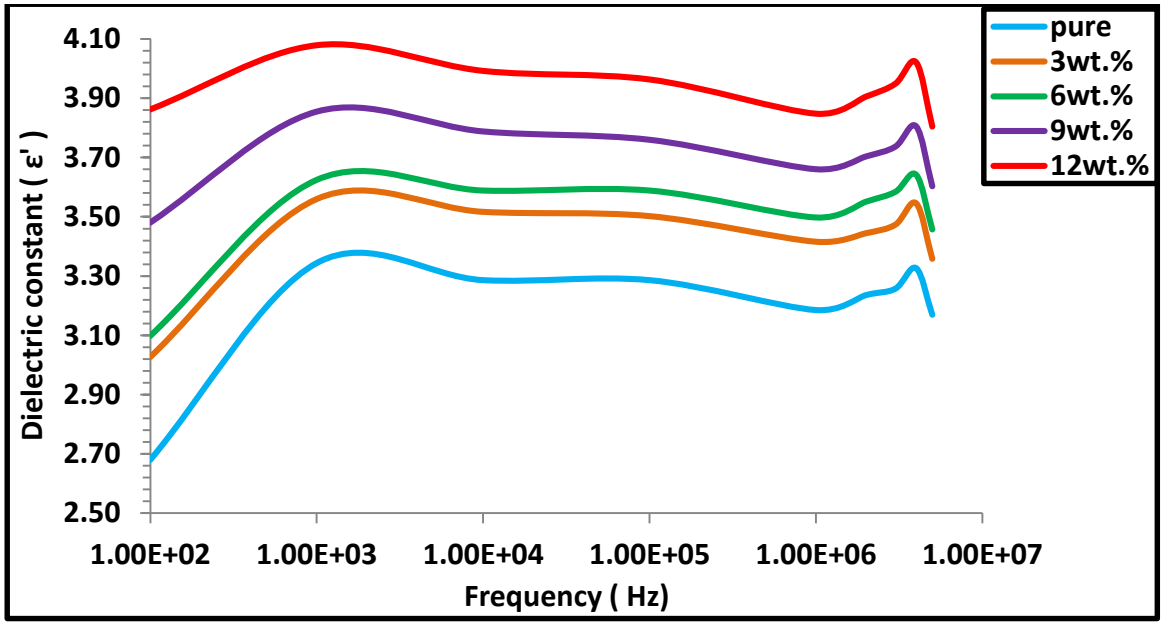

Figure (4.14): Dielectric constant variation for (PS:PMMA)/$BaTiO_3$ nanocomposite blend with frequency at room temperature.

Influence of weight ratio of $BaTiO_3$ nanoparticles versus the dielectric constant for (PS:PMMA) poly blend at frequency 1000Hz are shown in Figure (4.15). The increase of $BaTiO_3$ nanoparticles weight ratio lead to the increasing in the dielectric constant for (PS:PMMA)/$BaTiO_3$ nanocomposite blend as shown in Table (4.3). This is not only due to the atomic, ionic, and electronic influence but also due to the space charge influence [120]. These results are in agreement with [117,118].

Table (4.3): Dielectric constant values for (PS:PMMA)/$BaTiO_3$ nanocomposite blend at frequency 1000 Hz.

$BaTiO_3$ wt.%	Electrical dielectric constant
0	3.343
3	3.559
6	3.624
9	3.855
12	4.078

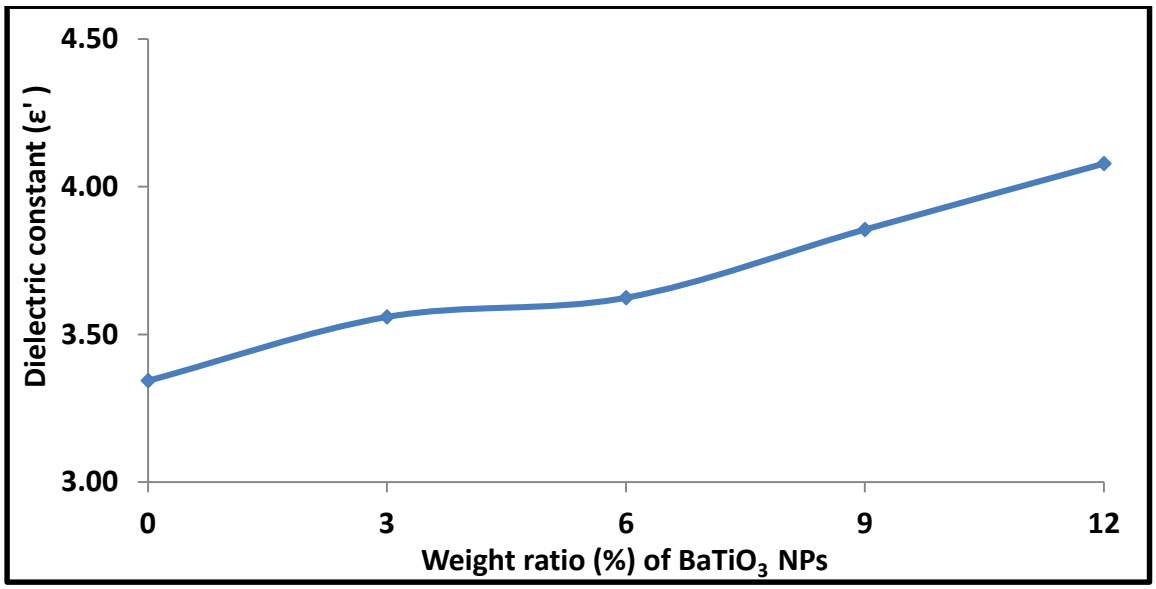

Figure (4.15): Influence of $BaTiO_3$ NPs weight ratio on dielectric constant for (PS:PMMA) poly blend at frequency 1000Hz.

4.3.2 Dielectric Loss

The dielectric loss can be calculated by the equation (2.7). Figure (4.16) shows the variation of dielectric loss for (PS:PMMA)/$BaTiO_3$ nanocomposite blend versus frequency at room temperature. For all prepared films of nanocomposite the dielectric loss decrease with the increasing of the frequency of applied electric field, this behavior attributed to the decrease of the space charge polarization contribution and associated to the inability of dipoles to rotate quickly leading to a gap between frequency of oscillating dipole and that of the applied field. But the dielectric loss becomes very large for (PS:PMMA)/$BaTiO_3$ nanocomposite blend at lower frequencies, due to free charge motion within the material in addition to the enough time for electric dipoles to align with applied electric field before it variation electric dipoles direction; so the dielectric loss of this nanocomposite is high [117]. These results are in agreement with [114-116,118].

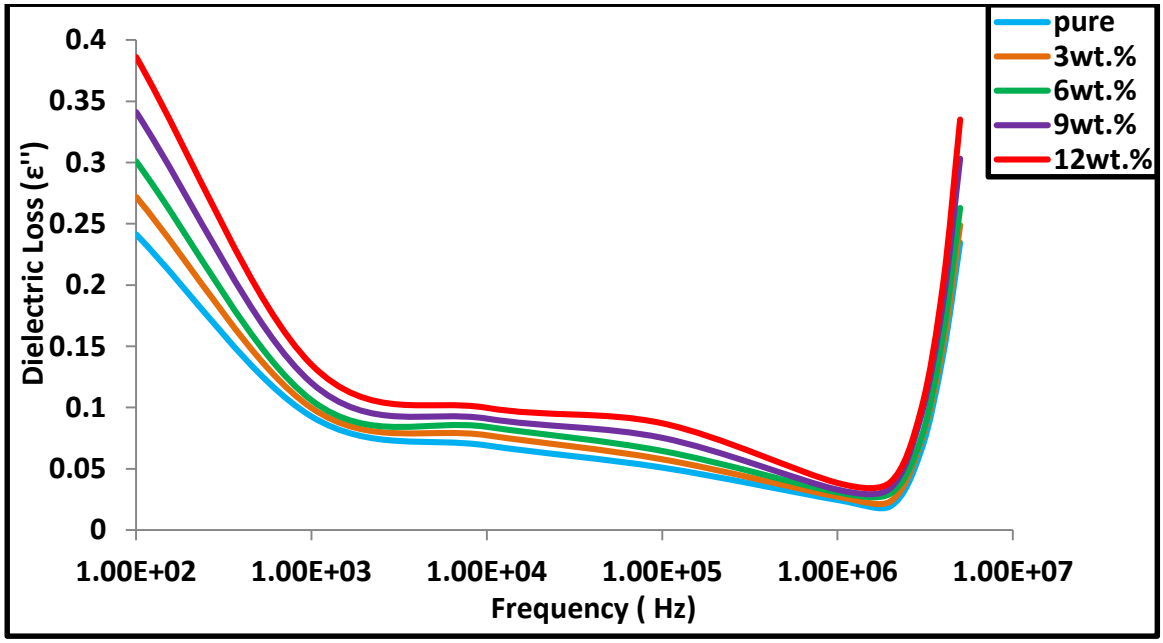

Figure (4.16): Dielectric loss variation for (PS:PMMA)/$BaTiO_3$ nanocomposite blend with frequency at room temperature.

Influence of weight ratio of $BaTiO_3$ nanoparticles versus the dielectric loss for (PS:PMMA) poly blend at frequency 1000Hz are shown in Figure (4.17). Increasing $BaTiO_3$ nanoparticles weight ratio lead to the increase in dielectric loss for (PS:PMMA)/$BaTiO_3$ nanocomposite blend as shown in Table (4.4). These increase due to the increasing of the charge carriers number for (PS:PMMA)/$BaTiO_3$ nanocomposite blend [117]. These results are in agreement with [118].

Table (4.4): Dielectric loss values for (PS:PMMA)/$BaTiO_3$ nanocomposite blend at frequency 1000 Hz.

$BaTiO_3$ wt.%	Electrical dielectric loss
0	0.092
3	0.099
6	0.106
9	0.120
12	0.135

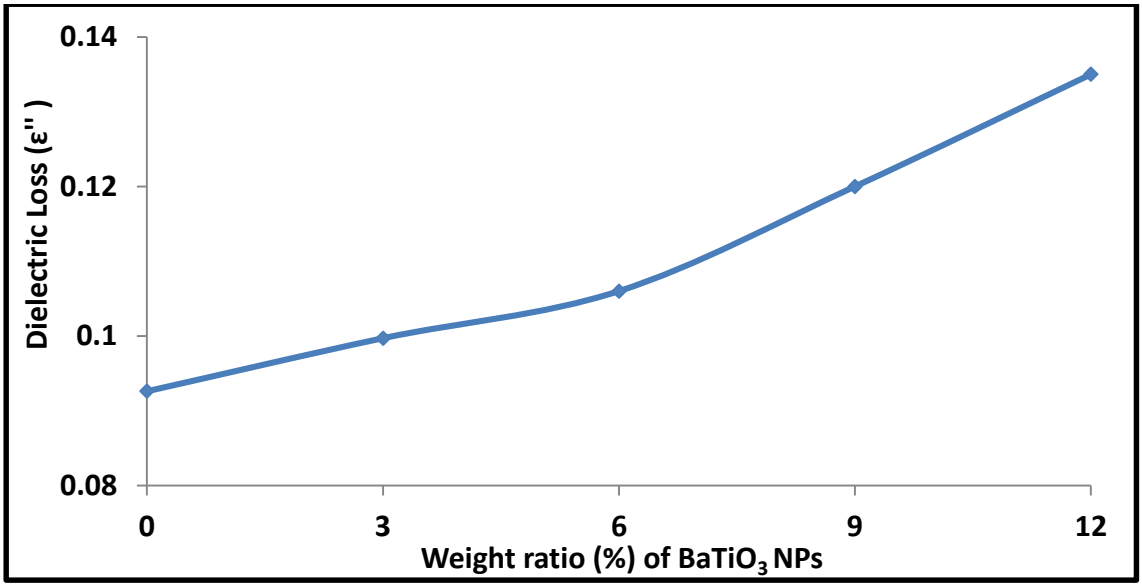

Figure (4.17): Influence of $BaTiO_3$ NPs weight ratio on dielectric loss for (PS:PMMA) poly blend at frequency 1000Hz.

4.3.3 A.C Electrical Conductivity

A.C Electrical conductivity can be calculated by the equation (2.8). Figure (4.18) shows the variation of A.C electrical conductivity for (PS:PMMA)/$BaTiO_3$ nanocomposite blend versus frequency at room temperature. The A.C electrical conductivity increase with increasing of the frequency of electric field for all prepared films of nanocomposite, where the frequency acts as a pumping force, pushing the charge carriers between the different conduction states. This means the mobility of charge carriers and the hopping of ions from the cluster. In the low frequency, more charge accumulation occurred at the electrode and electrolyte interface, leading to a decrease in the number of the ionization processes for $BaTiO_3$ nanoparticles and oxygen vacancy for (PS:PMMA) poly blend. The mobility of charge carriers was higher in the high frequency region; hence the electrical conductivity increase with frequency for (PS:PMMA)/$BaTiO_3$ nanocomposite blend [117]. These results are in agreement with [114-116,118].

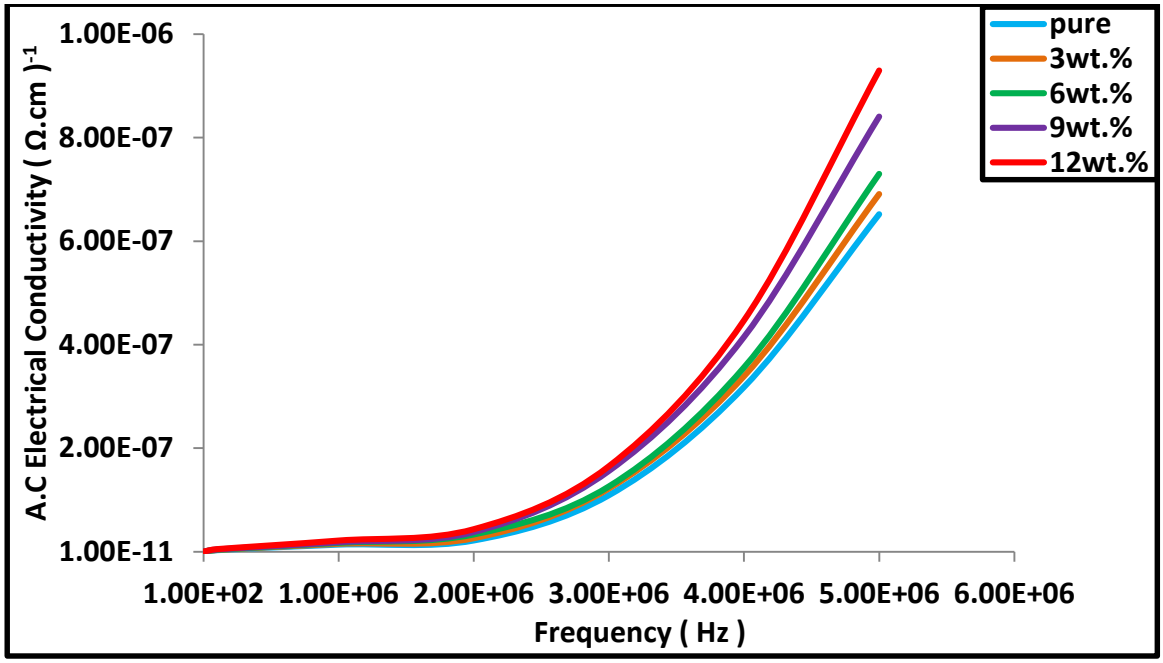

Figure (4.18): Variation of A.C electrical conductivity for (PS:PMMA)/$BaTiO_3$ nanocomposite blend with frequency at room temperature.

Influence of weight ratio of $BaTiO_3$ nanoparticles versus the A.C electrical conductivity for (PS:PMMA) poly blend at frequency 1000Hz are shown in Figure (4.19). Increasing $BaTiO_3$ nanoparticles weight ratio lead to the increase in A.C electrical conductivity for (PS:PMMA)/$BaTiO_3$ nanocomposite blend as shown in Table (4.5). This is increase of the conductivity attributed to the increasing of the charge carriers number due to dopant nanoparticles composition which reduces the resistance of the nanocomposite gradually and increase the A.C electrical conductivity [121,122]. These results are in agreement with [117,118].

Table (4.5): A.C Electrical conductivity values for (PS:PMMA)/$BaTiO_3$ nanocomposite blend at frequency 1000 Hz.

$BaTiO_3$ wt.%	A.C Electrical conductivity
0	5.15E-11
3	5.54E-11
6	5.88E-11
9	6.64E-11
12	7.48E-11

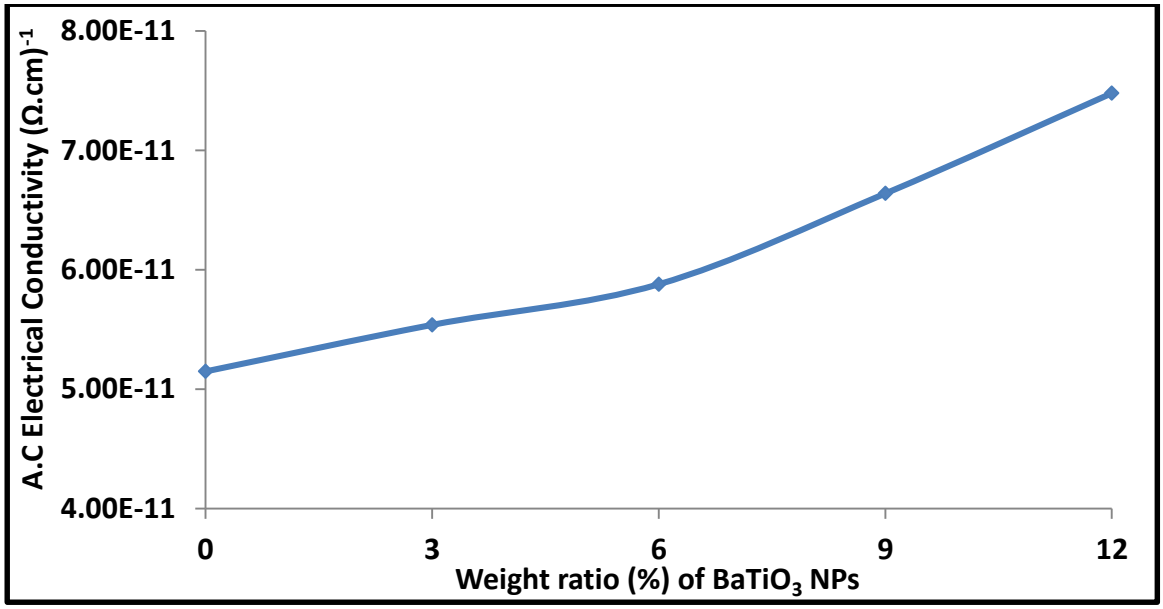

Figure (4.19): Influence of $BaTiO_3$ NPs weight ratio on A.C electrical conductivity for (PS:PMMA) poly blend at frequency 1000Hz.

4.4 Optical Properties

The main purpose of optical properties study for (PS:PMMA)/$BaTiO_3$ nanocomposite blend to know the influence of $BaTiO_3$ nanoparticles additive on the optical properties for (PS:PMMA) poly blend. The absorbance and transmittance have been recorded for (PS:PMMA) poly blend with different weight ratios of $BaTiO_3$ nanoparticles.

4.4.1 Absorbance Spectrum

The absorbance spectrum for (PS:PMMA)/$BaTiO_3$ nanocomposite blend are shown in Figure (4.20). As indicated in Figure (4.20), $BaTiO_3$ nanoparticles enhances the absorbance of the (PS:PMMA) poly blend. The UV-Visible absorption spectrum of (PS:PMMA) poly blend and (PS:PMMA)/$BaTiO_3$ nanocomposite blend are carried out at room temperature. The UV optical absorption pattern of (PS:PMMA) poly blend exhibits an absorption band like shoulder at about λ = 260 nm. This band is attributed to the carbonyl group [123]. It is observed that the wavelength corresponding to the absorption band like shoulder increase with increasing in $BaTiO_3$ nanoparticles content; this increase has been attributed to the minor structural inhomogeneities present in (PS:PMMA) poly blend [124]

which are due to growth of $BaTiO_3$ nanoparticles inside the polymeric matrix. As the nanocomposite films show a red shift behavior, these shifts indicate the complexation between the $BaTiO_3$ nanoparticles and the (PS:PMMA) poly blend and may also be due to change in crystallinity with presence of additive [125]. These results were confirmed by XRD results. Formation of new peaks for the prepared films and also broadening of those peaks with increasing $BaTiO_3$ nanoparticles indicate a considerable interaction between additive and host (PS:PMMA) poly blend [126]. Also Figure (4.20) shows that the absorbance increase by adding different weight ratios of $BaTiO_3$ nanoparticles; this is related to absorbance of $BaTiO_3$ nanoparticles or, in other words, the absorbance increase with weight ratios of absorbed particles [127]. The absorption at any wavelength depends on the number of particles along the path of the incident light (i.e., it depends on weight ratio of $BaTiO_3$ nanoparticles) and on the length of the optical path passing through[128]. These results are in agreement with [116,124,129-131].

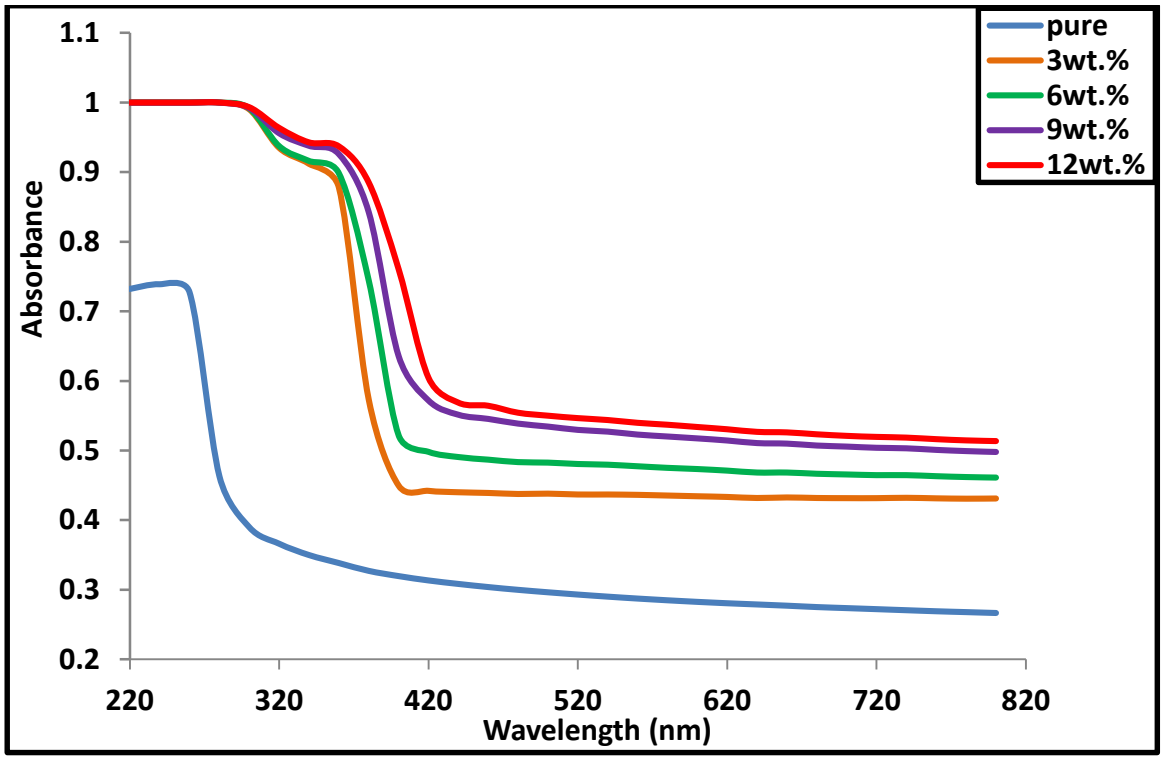

Figure (4.20): Absorbance variation for (PS:PMMA)/$BaTiO_3$ nanocomposite blend with wavelength.

4.4.2 Transmittance Spectrum

Figure (4.21) shows an optical transmittance spectrum as a function of incident wavelength on $BaTiO_3$ doped (PS:PMMA)poly blend. The transmittance decrease with increasing filler weight ratio; this is because of layer of covalent bonds formed between polymer chains and additives that decrease the transmitting of the incident light especially at the shortest wavelengths. The electrons in the outer orbits have travelled to the higher energy levels and have occupied vacant positions of energy bands. Thus, part of incident light does not penetrate through it. However, the undoped (PS:PMMA) poly blend has no free electron and the conduction band needs photon with high energy, after which it has high transmittance [132]. These results are in agreement with [75,130,131].

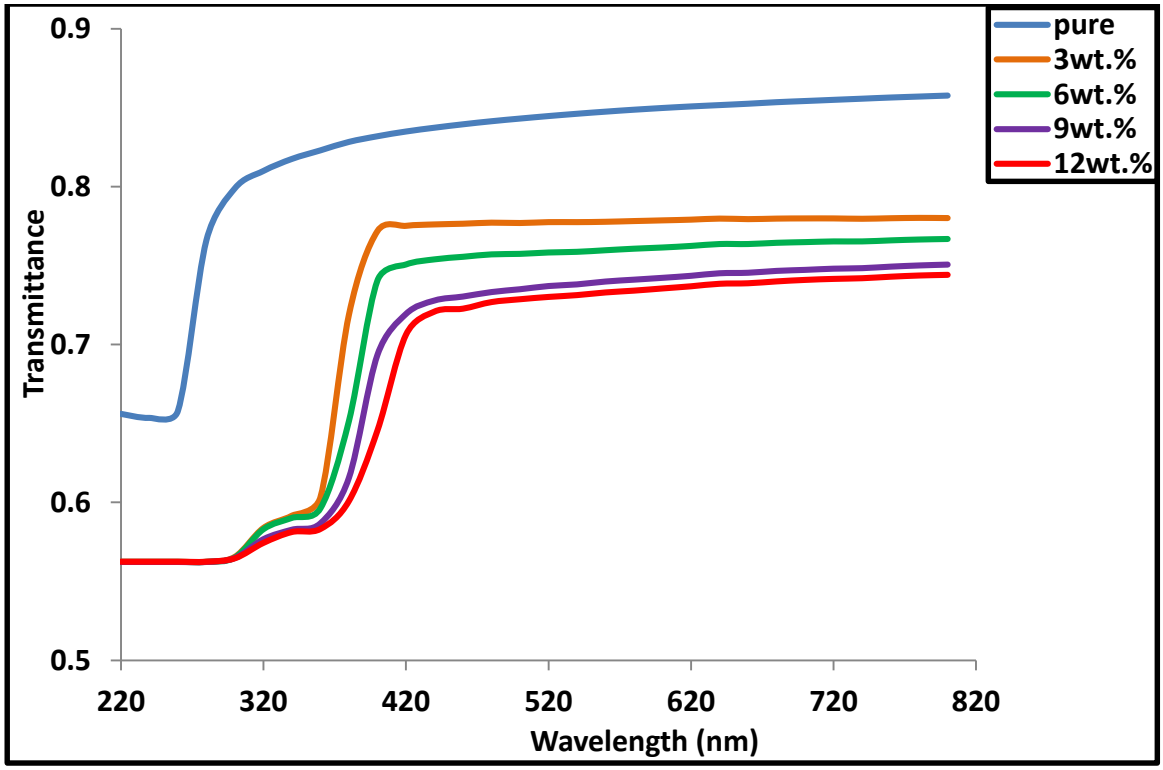

Figure (4.21): Transmittance variation for (PS:PMMA)/$BaTiO_3$ nanocomposite blend with wavelength.

4.4.3 Reflectance Spectrum

Figure (4.22) shows the reflectance versus wavelength of the incident light on the (PS:PMMA)/$BaTiO_3$ nanocomposite blend. The reflectance increase with increasing the weight ratio of $BaTiO_3$ nanoparticles and increase (reflectance) with the decreasing the incident photon wavelength of all films and reach the maximum reflectance value at the wavelength corresponding to the film energy gap and it can be an indicator to the material absorption edge. These results are in agreement with [131].

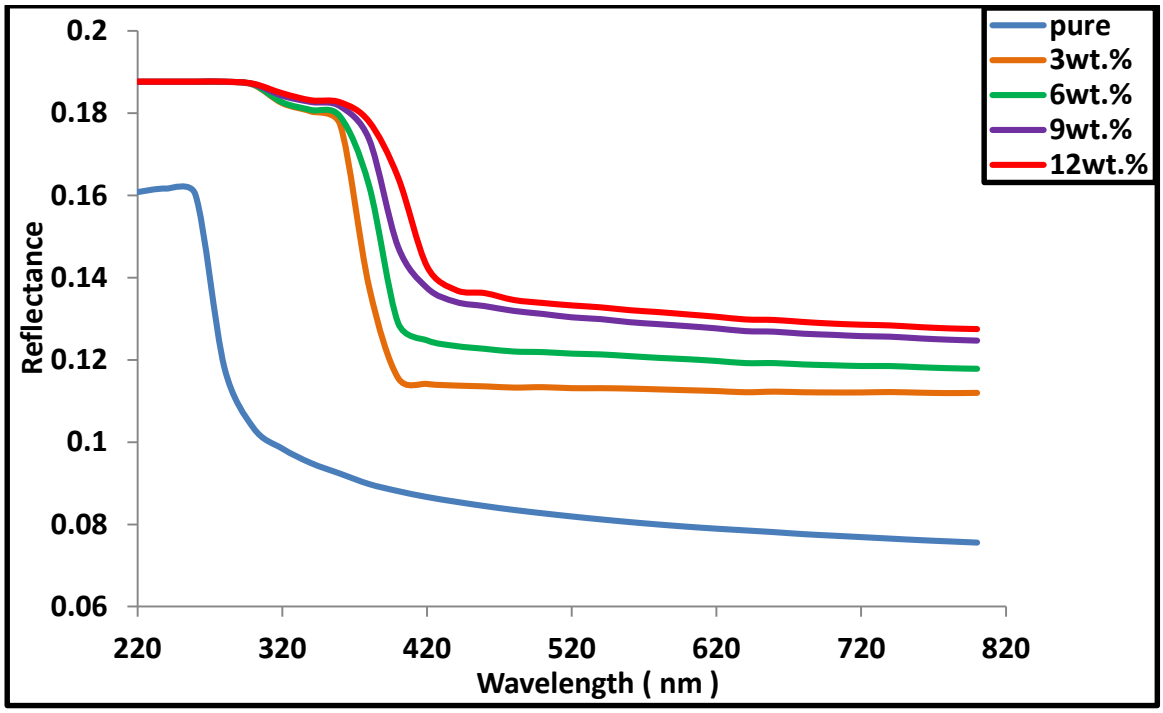

Figure (4.22): Reflectance variation for (PS:PMMA)/$BaTiO_3$ nanocomposite blend with wavelength.

4.4.4 Absorption Coefficient (α)

Absorption coefficient calculated by using the equation (2.14). Figure (4.23) shows the absorption coefficient against incident photon energy for (PS:PMMA) poly blend with different weight ratio of $BaTiO_3$ nanoparticles. It is clear that the absorption coefficient is increase with increasing the weight ratio of $BaTiO_3$ nanoparticles; this may be attributed to increase in the absorbance [133]. Figure (4.23) also shows the dependence of absorption coefficient on incident photon energy, indicated from the low value of

absorption coefficient with low value of photon energy and vice versa which means that the possibility of electron transition is increasing with photon energy. These results are in agreement with [75,116,129-131].

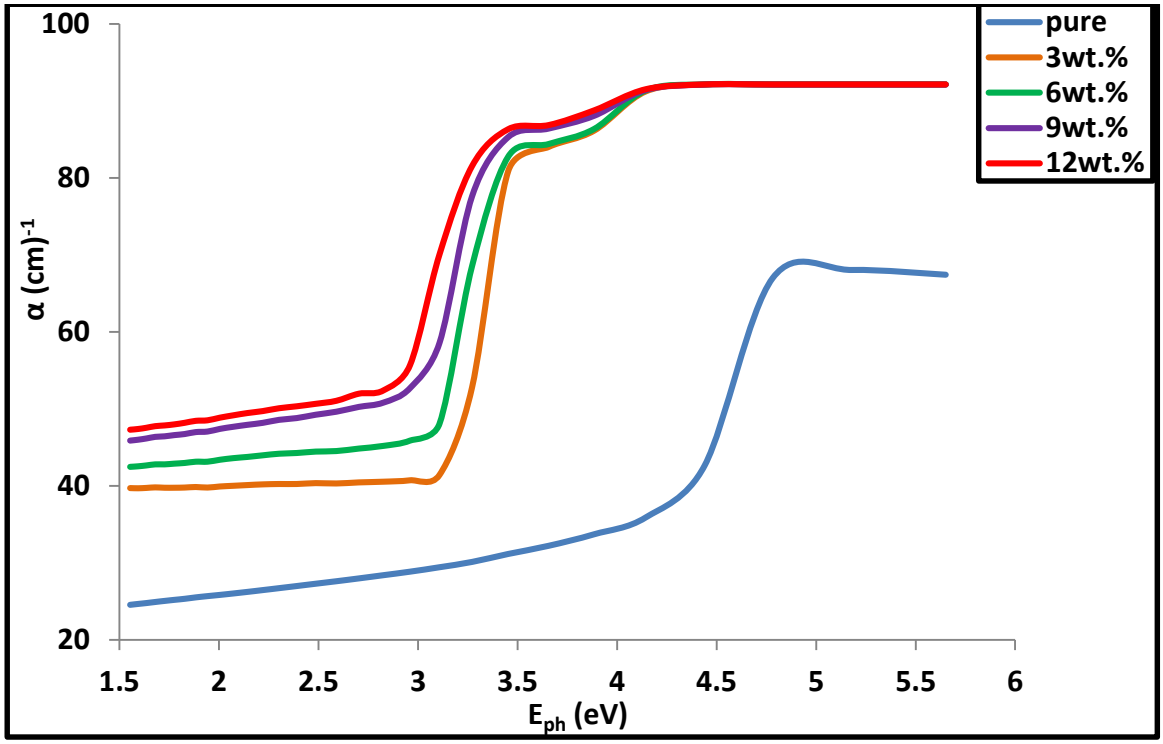

Figure (4.23): Absorption coefficient variation for (PS:PMMA)/$BaTiO_3$ nanocomposite blend with photon energy.

4.4.5 Extinction Coefficient (*K*)

Extinction coefficient calculated by using the equation (2.15). Figure (4.24) shows the variations of extinction coefficient as a function of wavelength for (PS:PMMA)/$BaTiO_3$ nanocomposite blend. It shows by increasing of $BaTiO_3$ nanoparticles for (PS:PMMA) poly blend the extinction coefficient is increase due to high absorption coefficient for (PS:PMMA)/$BaTiO_3$ nanocomposite blend. Where $BaTiO_3$ nanoparticles will modify the structure of the host (PS:PMMA) poly blend [134]. These results are in agreement with [75,116,129-131,135,136].

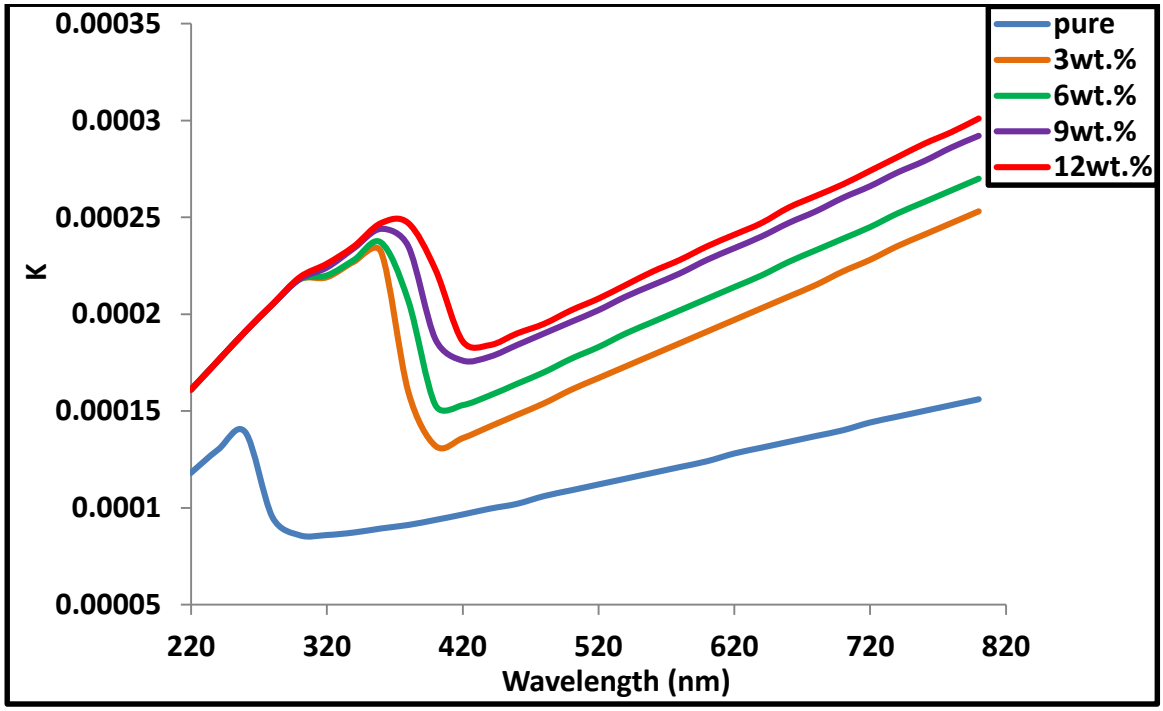

Figure (4.24): Extinction coefficient variation for (PS:PMMA)/$BaTiO_3$ nanocomposite blend with wavelength.

4.4.6 Refractive Index (*n*)

Refractive index calculated by using the equation (2.16). Refractive index must be studied to describe the propagation of the electromagnetic waves in the medium. Figure (4.25) illustrates the variations of refractive index with wavelength for (PS:PMMA)/$BaTiO_3$ nanocomposite blend. Figure (4.25) indicates that the refractive index decrease with increasing wavelength. The Figure shows that the refractive index increase as a result of increasing in the weight ratio of $BaTiO_3$ nanoparticles which is due to the increasing of the density of composites film as a result of $BaTiO_3$ nanoparticles content. Increase in refractive index with weight ratio of $BaTiO_3$ nanoparticles is a result of increasing number of atomic refractions due to the increase of the linear polarizability which agree with Lorentz-Lorenz formula [133]. These results are in agreement with [75,116,129-131].

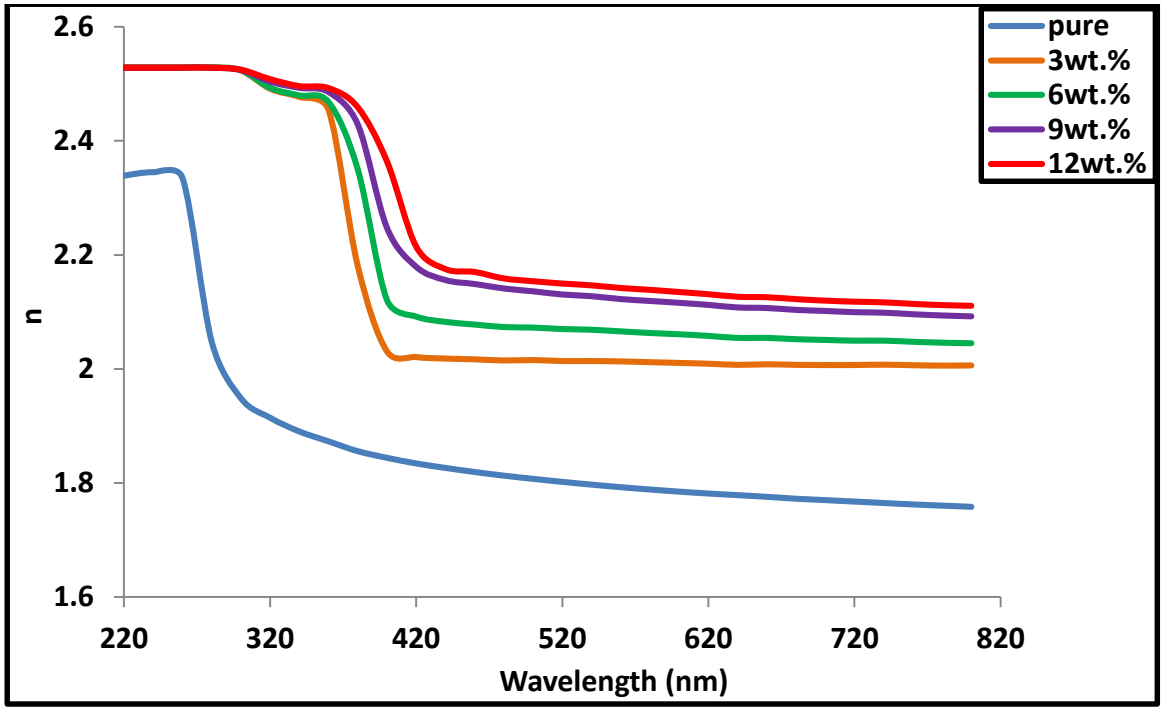

Figure (4.25): Refractive index variation for (PS:PMMA)/$BaTiO_3$ nanocomposite blend with wavelength.

4.4.7 Real and Imaginary Part of Dielectric Constant $(\varepsilon_r, \varepsilon_i)$

Figure (4.26) shows the variations of real part of dielectric constant (ε_r) versus wavelength for (PS:PMMA)/$BaTiO_3$ nanocomposite blend. It can be indicated that the real part of dielectric constant mainly proportional to the square of refractive index as shown in the equation (2.21). So, it is increase with increasing of $BaTiO_3$ nanoparticles additive.

Figure (4.27) shows the variations of imaginary part of dielectric constant (ε_i) versus wavelength for (PS:PMMA)/$BaTiO_3$ nanocomposite blend. Its proportional to the extinction coefficient as shown in the equation (2.22) and its increase with the increasing of $BaTiO_3$ nanoparticles additive [117]. These results are in agreement with [75,116,129,131].

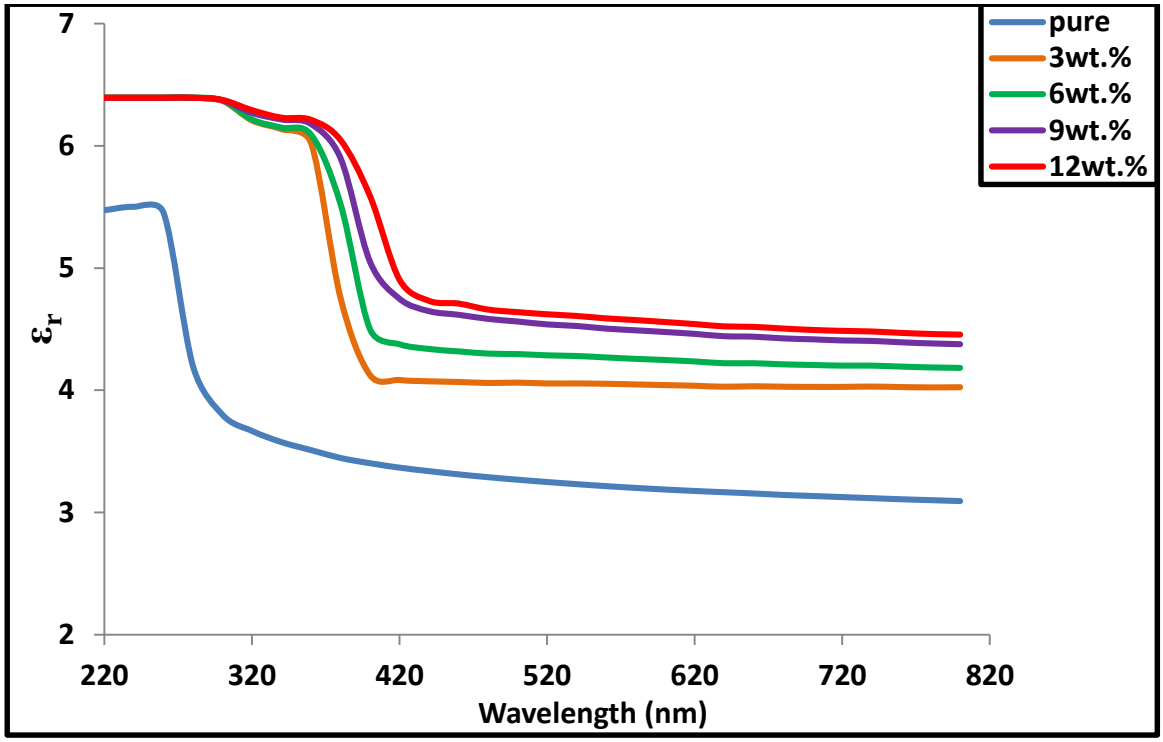

Figure (4.26): Real part of dielectric constant variation for (PS:PMMA)/$BaTiO_3$ nanocomposite blend with wavelength.

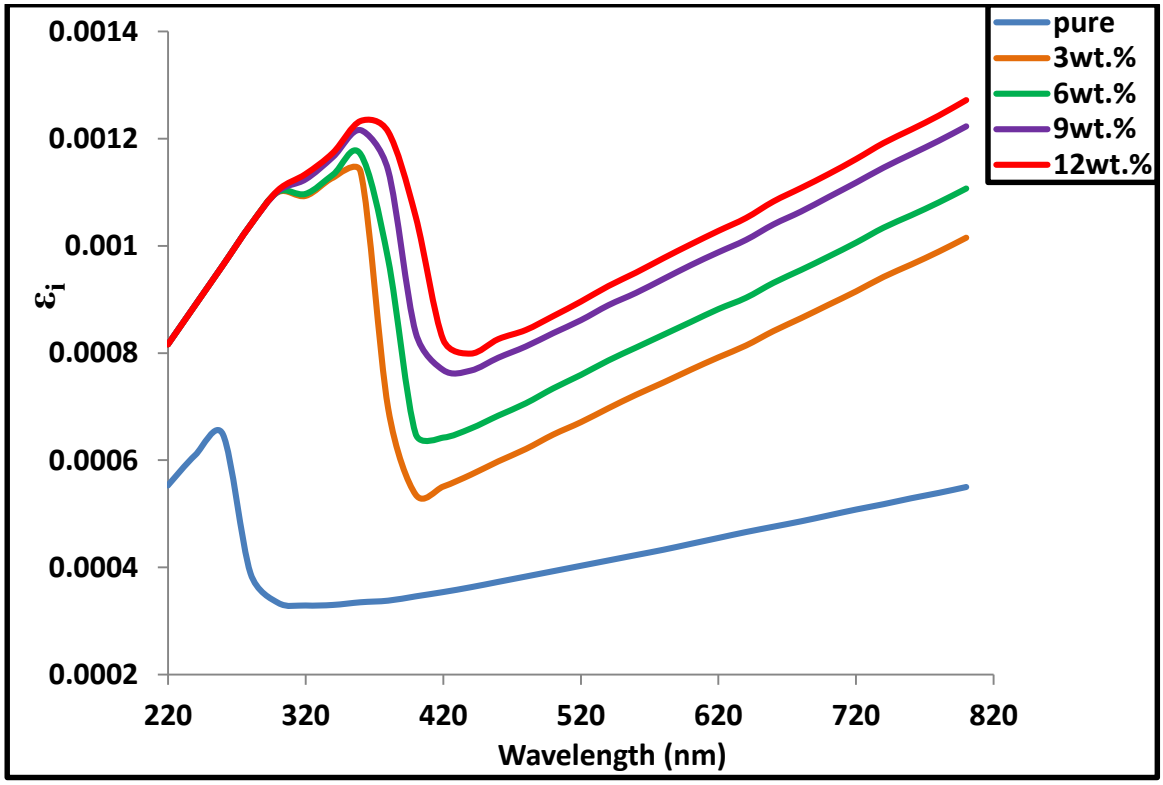

Figure (4.27): Imaginary part of dielectric constant variation for (PS:PMMA)/$BaTiO_3$ nanocomposite blend with wavelength.

4.4.8 Optical Energy Gaps of The (Allowed and Forbidden) Indirect Transition

The allowed and forbidden energy band gap of indirect transition can be found based on the equation (2.24) when the value of (r = 2) that means an allowed indirect transitions, but when the value of (r = 3) this indicates forbidden indirect transition. Figure (4.28) shows the variations of absorbance edge $(\alpha h\upsilon)^{1/2}$ for (PS:PMMA)/$BaTiO_3$ nanocomposite blend versus photon energy. By plotting a line from the upper side of the curve in direction axis (x) in value ($(\alpha h\upsilon)^{1/2}$ = zero) to get the allowed energy band gap of indirect transition[137]. With increase $BaTiO_3$ nanoparticles weight ratio, the values of allowed energy band gap for (PS:PMMA)/$BaTiO_3$ nanocomposite blend are decrease. Because of creation of localized states in the forbidden energy band gap [138-141]. In addition to attribute to oxygen vacancies of $BaTiO_3$ nanoparticles which due to form non-stoichiometry [142].

Figure (4.29) shows the variations of absorbance edge $(\alpha h\upsilon)^{1/3}$ for (PS:PMMA)/$BaTiO_3$ nanocomposite blend versus photon energy. With increase $BaTiO_3$ nanoparticles weight ratio the values of forbidden energy band gap for (PS:PMMA)/$BaTiO_3$ nanocomposite blend are decrease, this attributed to creation new levels and the transition of electrons between the tails of localized of the new levels made by the $BaTiO_3$ nanoparticles additive [137]. These results are in agreement with [75,116,129,131].

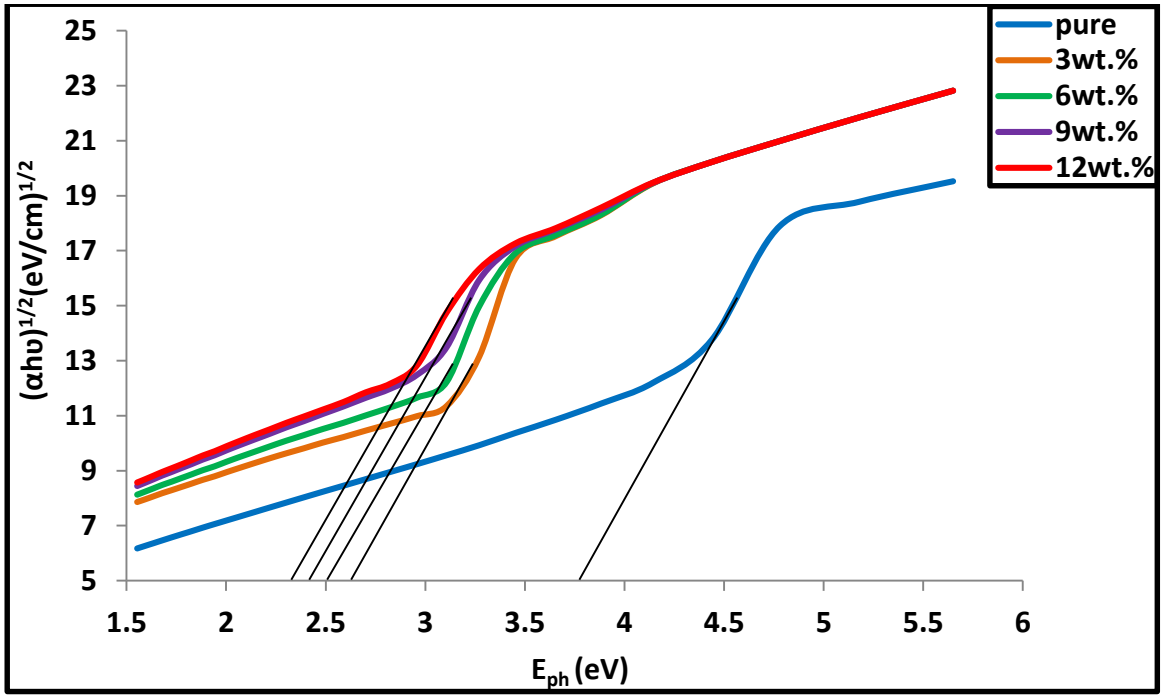

Figure (4.28): Relation between photon energy and $(\alpha h\upsilon)^{1/2}$ for (PS:PMMA)/$BaTiO_3$ nanocomposite blend.

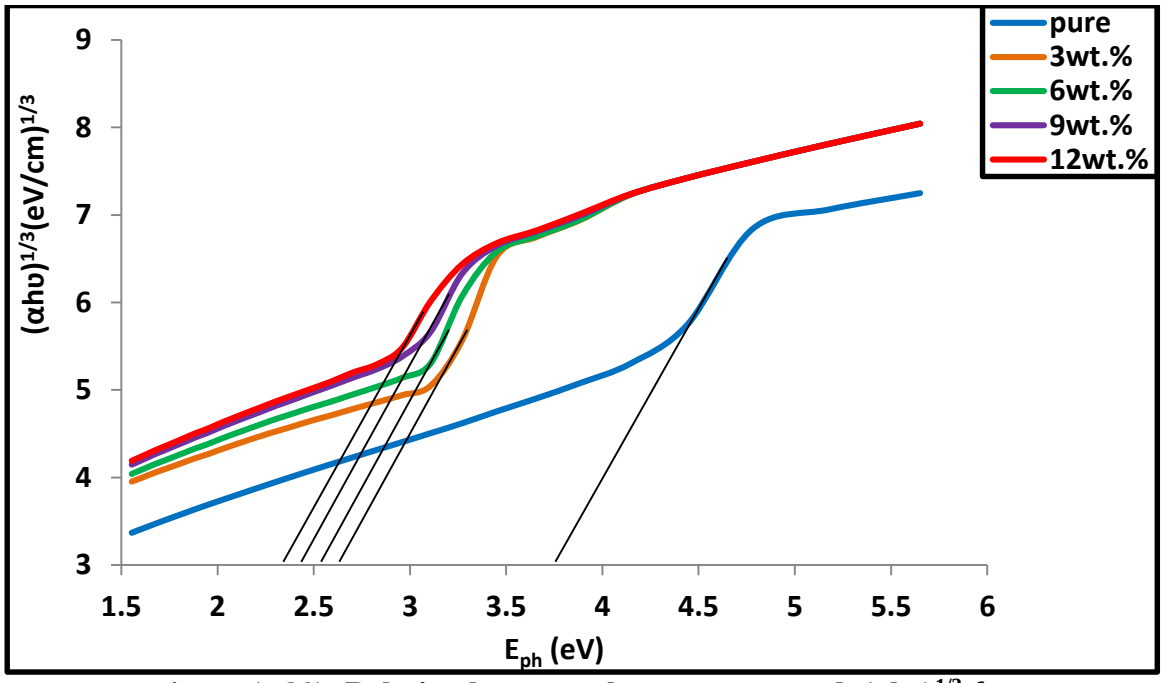

Figure (4.29): Relation between photon energy and $(\alpha h\upsilon)^{1/3}$ for (PS:PMMA)/$BaTiO_3$ nanocomposite blend.

Values of optical energy band gap for the allowed and forbidden indirect transition for (PS:PMMA)/$BaTiO_3$ nanocomposite blend have been getting in Table (4.6), these values decrease with increasing $BaTiO_3$ nanoparticles

weight ratio this attribute to creation of localized states in the band gap as a result of compositional disorder [143].

Table (4.6): Values of optical energy gap for allowed and forbidden indirect transition for (PS:PMMA)/$BaTiO_3$ nanocomposite blend.

$BaTiO_3$ NPs wt.%	$E_g(eV)$	
	Allowed	Forbidden
0	3.78	3.75
3	2.62	2.625
6	2.5	2.520
9	2.42	2.437
12	2.32	2.333

The increase of the weight ratio of $BaTiO_3$ nanoparticles lead to decrease values of optical energy gap for the allowed and forbidden indirect transition for (PS:PMMA)/$BaTiO_3$ nanocomposite blend as shown in Figure (4.30).

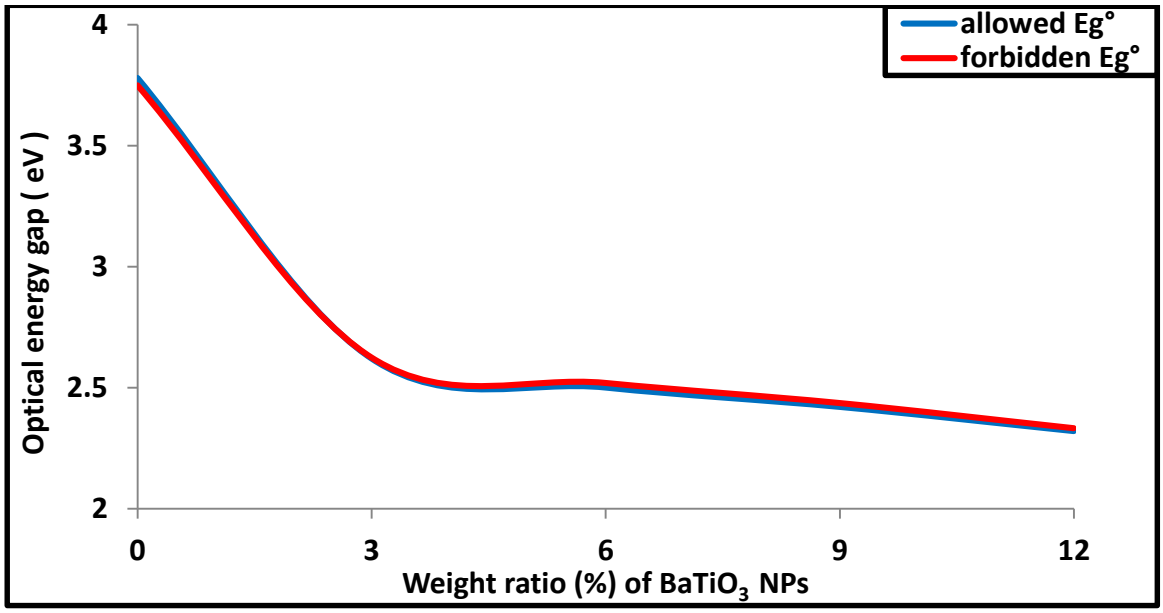

Figure (4.30): Relation between weight ratio of $BaTiO_3$ NPs and optical energy gap for (PS:PMMA)/$BaTiO_3$ nanocomposite blend.

Adding $BaTiO_3$ nanoparticles to (PS:PMMA) poly blend, i.e. doping, can induce a decrease in the band gap due to compositional changes, can also create localized states in the band gap, which will lead to a shift in the

absorption edge towards a lower photon energy, and a decrease in the optical energy gap [144].

4.4.9 Optical Conductivity

The optical conductivity can be calculated from the equation (2.25). Figure (4.31) shows the optical conductivity variation with wavelength for (PS:PMMA)/$BaTiO_3$ nanocomposite blend. The optical conductivity is increase for (PS:PMMA)/$BaTiO_3$ nanocomposite blend due to $BaTiO_3$ nanoparticles are increase which leads to increase the absorption coefficient [145,146]. In addition to; This increase due to the creation of new levels in the band gap, lead to ease of passage charge carriers from the valence to the conduction band, as a result decreasing in the band gap and the conductivity increase [147]. These results are in agreement with [116,130,131].

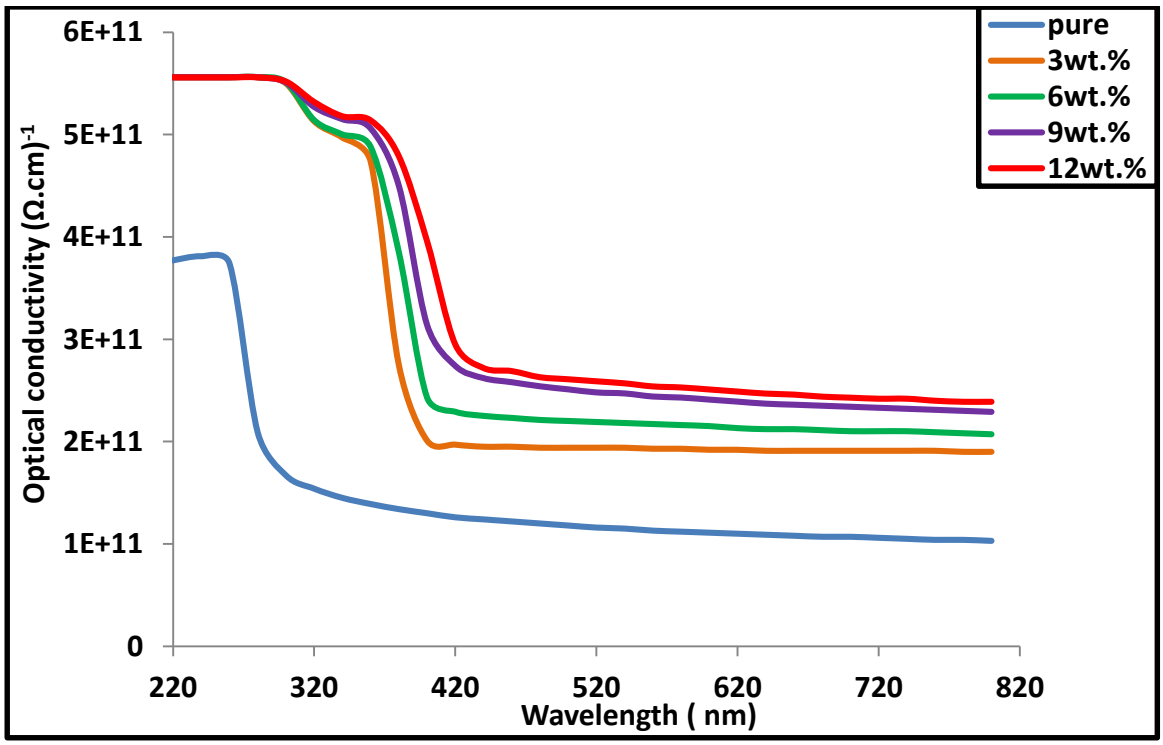

Figure (4.31): Optical conductivity variation for (PS:PMMA)/$BaTiO_3$ nanocomposite blend with wavelength.

4.5 Piezoelectric Sensor Application

Figure (4.32) shows the variation of resistance for (PS:PMMA)/$BaTiO_3$ nanocomposite blend versus weight ratio of $BaTiO_3$ nanoparticles at low applied load (80 bar). From the Figure we note that the resistance decrease due to the (PS:PMMA) poly blend exhibit high polarization and ability to align or orient the molecular dipoles with applied load. Where the orientation and space charge polarization of molecular dipoles is responsible for piezoelectricity in the nanocomposite. Where the (PS:PMMA)/$BaTiO_3$ nanocomposite blend are more flexible [148].

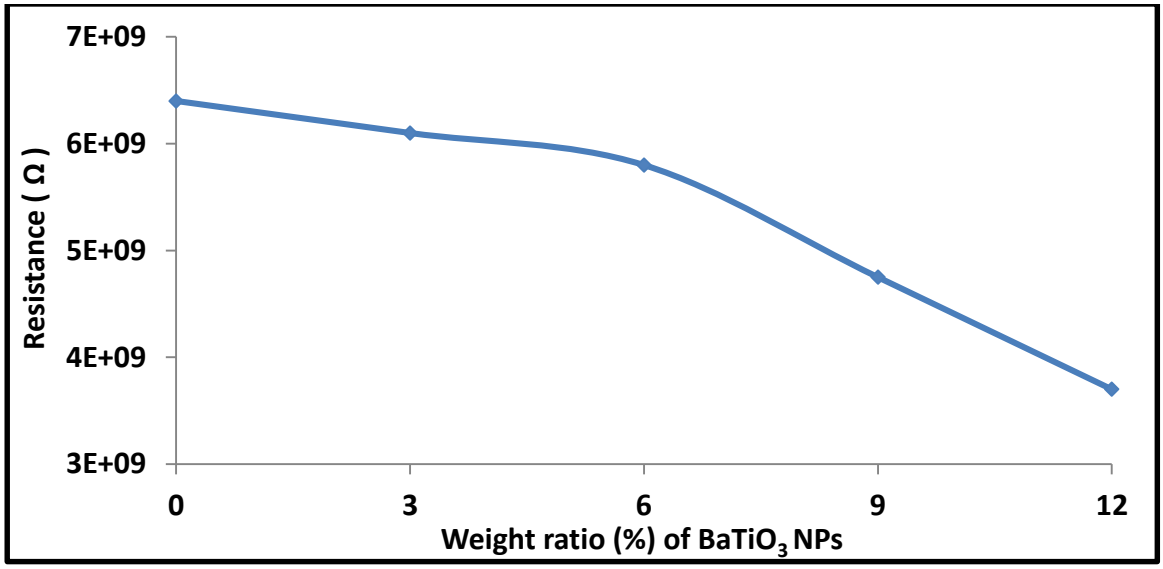

Figure (4.32): Influence of $BaTiO_3$ NPs weight ratio for (PS:PMMA) poly blend on resistance at low applied load (80bar).

Figure (4.33) shows the variation of resistance for (PS:PMMA)/$BaTiO_3$ nanocomposite blend versus weight ratio of $BaTiO_3$ nanoparticles at high applied load (160 bar). Its noted that resistance slowly decrease with increasing of $BaTiO_3$ nanoparticles additive due to that only each Oxygen atom have the same distance to the Barium atom, and the distances are all the same between the oxygen atoms. The change in the position of the atoms due to mechanical stress leads to the formation of net dipole moments that causes polarization and an electric field respectively [149].

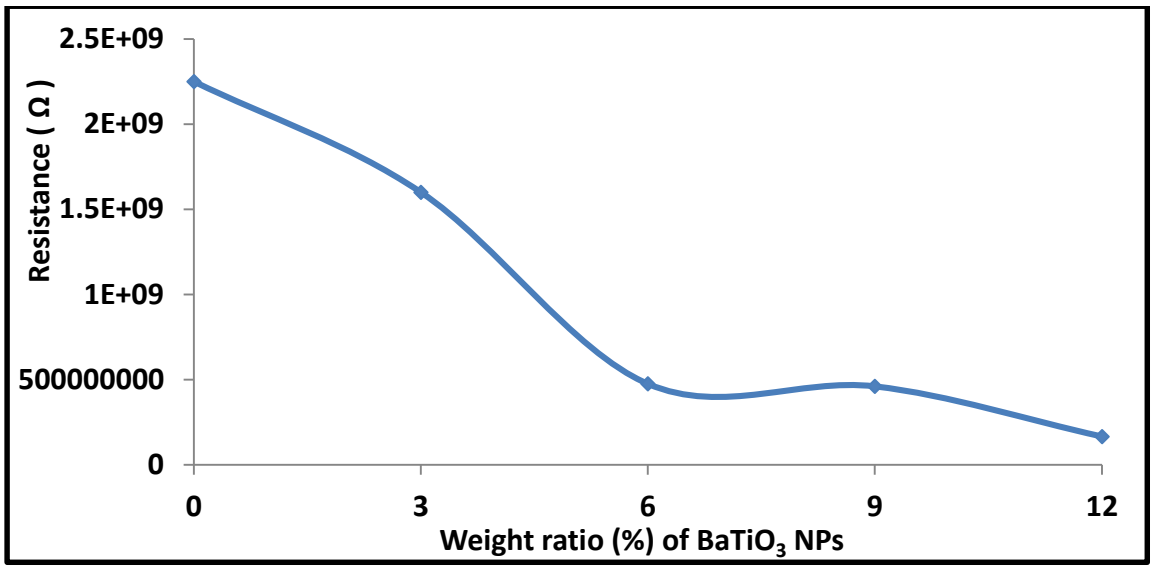

Figure (4.33): Influence of $BaTiO_3$ NPs weight ratio for (PS:PMMA) poly blend on resistance at high applied load (160bar).

Figure (4.34) shows the variation of resistance for (PS:PMMA)/$BaTiO_3$ nanocomposite blend versus applied load. By increase mechanical stress the electrical resistance for (PS:PMMA)/$BaTiO_3$ nanocomposite blend will be decrease. This is due to the geometry of the atomic structure of $BaTiO_3$ nanoparticles changes and the ions in the structure separated to form dipole moment then the electrical dipoles appear. In addition to oxygen vacancies for (PS:PMMA) poly blend form localized levels below the conduction band. This means the mobility of charge carriers and the hopping of ions from the cluster. Then the current increase due to the internal stress increasing, indicate that the resistance will be decrease [150].

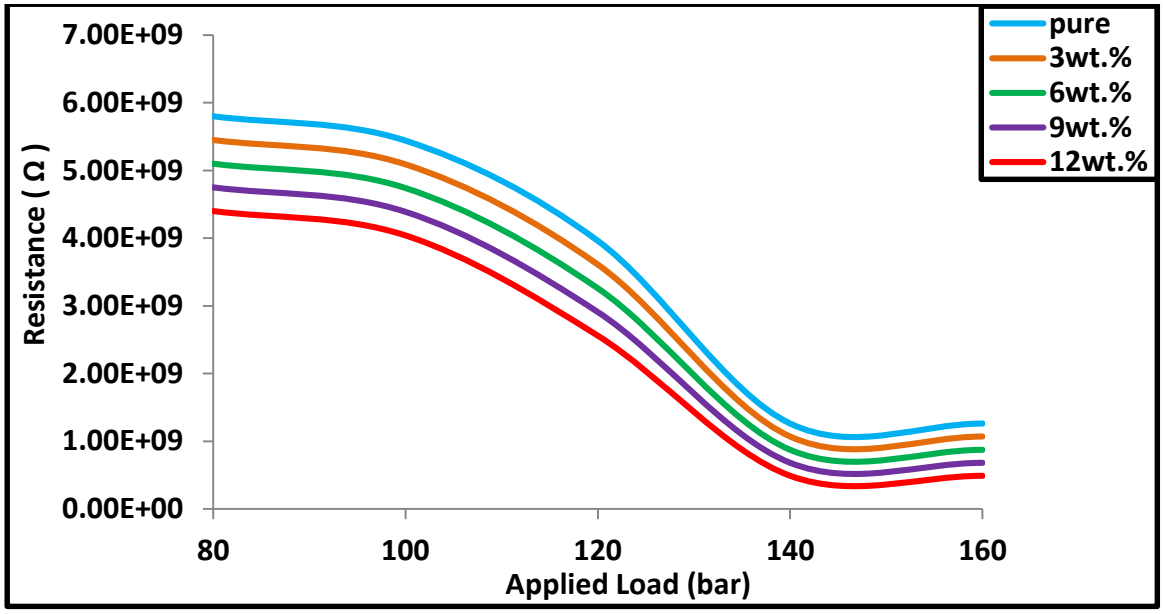

Figure (4.34): Variation of resistance for (PS:PMMA)/$BaTiO_3$ nanocomposite blend with applied load.

4.6 Antibacterial Activity Application

The antibacterial activity of (PS:PMMA)/$BaTiO_3$ nanocomposite blend was tested against Staphylococcus aureus and Enterococcus faecalis as gram positive bacteria and Enterobacter cloacae and Escherichia coli as gram negative bacteria. The inhibitory activity was measured based on the diameter of the clear inhibition zone. If there was no surrounding clear zone, it was assumed that there was no inhibitory zone. The zones of inhibition around pieces of (PS:PMMA) poly blend, and (PS:PMMA)/$BaTiO_3$ nanocomposite blend for bacterial culture are shown in Figure (4.35) while numerical values of inhibition zone diameter were compiled in Table (4.7) and presented in Figure (4.36).

The results exhibited very high toxicity against gram negative bacteria, lower toxicity against gram positive bacteria. The presence of $BaTiO_3$ nanoparticles from the (PS:PMMA)/$BaTiO_3$ nanocomposite blend explains the antimicrobial properties found in the prepared nanocomposites. In addition to this, the antimicrobial properties that have been exhibited in our results are similar with [151] who reported that small size nanoparticles may pass through cell membranes generating cell malfunction [152].

The positive charge on the nanoparticles is crucial for its antimicrobial activity through the electrostatic attraction between the negative charge on the cell membrane of microorganism and positively charged nanoparticles [153-155].

When the attraction is established, the nanoparticles will penetrate the cell membrane and bound with the electron donor functional groups such as phosphates, thiols, and indoles which contain sulfur and phosphorous compounds. All of these compounds are a presence in DNA or ribosomes. Thus the DNA function will be disrupted and the DNA cannot replicate. As a result, the microbial cell will not grow and eventually die [156].

A typical characteristic of any metal nanoparticle is begin able of reducing or removing microorganisms through two essential mechanisms: (a) the free metal ion toxicity that arises from dissolving metals from the surface of nanoparticles [157], and (b) releasing reactive oxygen species (ROS) and Barium ions [158].

The toxicity of ROS to bacteria is attributed to their high reactivity and oxidizing property. Numerous studies have considered ROS generation as the major cause of nanotoxicity [159]. The toxicity of these species involves the destruction of cellular components such as lipids, DNA, and proteins, as a result of their internalization into the bacteria cell membrane [160].

Generated ROS species, that is, hydrogen peroxide (H_2O_2), OH^-(hydroxyl radicals), O_2^{-2}(peroxide) and Barium ions from $BaTiO_3$ nanoparticles bind to the negative surface of the cell membranes, leading to disruption of the cells followed by leakage of inner cellular material that causes cell death [158].

The antibacterial activity of $BaTiO_3$ nanoparticles from (PS:PMMA)/$BaTiO_3$ nanocomposite blend given in the Table (4.7) showed higher activity against the pathogenic Enterobacter cloacae and Escherichia coli (24mm). The activity was limited against Staphylococcus aureus

(18mm). The higher activity was followed by Enterococcus faecalis (22mm). From this study, we revealed that the $BaTiO_3$ nanoparticles from (PS:PMMA)/$BaTiO_3$ nanocomposite blend showed good activity against both the gram positive and gram negative bacteria. Also it showed activity against cocci cells and rod cells.

Gram positive bacteria (Staphylococcus aureus and Enterococcus faecalis) is less susceptible than gram negative bacteria (Enterobacter cloacae and Escherichia coli) on $BaTiO_3$ nanoparticles. This is due to the gram positive bacteria possess a thick cell wall containing many layers of peptidoglycan. In contrast, gram negative bacteria have a relatively thin cell wall consisting of a few layers of peptidoglycan. Thus, a higher weight ratio of $BaTiO_3$ nanoparticles is required to kill Staphylococcus aureus and Enterococcus faecalis compared to Enterobacter cloacae and Escherichia coli [161].

It can be concluded that the (PS:PMMA)/$BaTiO_3$ nanocomposite blend that has been prepared is an effective agent against gram positive and gram negative bacteria (which is our case), taking into account that the $BaTiO_3$ nanoparticles are uniformly dispersed in the (PS:PMMA) poly blend. These results are in agreement with [162,163].

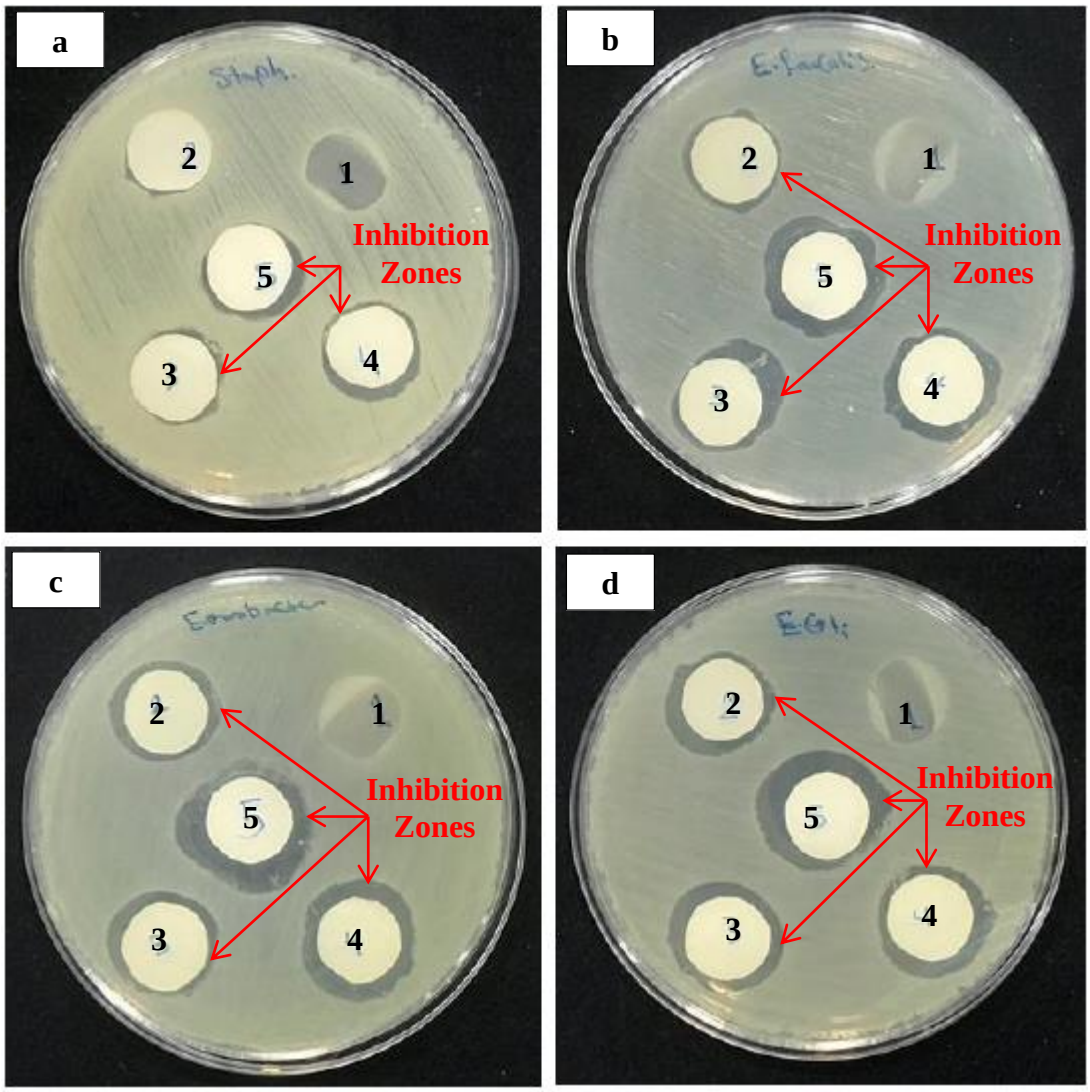

Figure (4.35): Antibacterial activity for (PS:PMMA)/$BaTiO_3$ nanocomposite blend against (a) Staphylococcus aureus (b) Enterococcus faecalis (c) Enterobacter cloacae (d) Escherichia coli. Numbers (1,2,3,4,5) refers to (0,3,6,9,12) wt.% of $BaTiO_3$ NPs respectively.

Table (4.7): Antibacterial activity of $BaTiO_3$ NPs from (PS:PMMA)/$BaTiO_3$ nanocomposite blend against pathogen.

$BaTiO_3$ wt.%	Inhibition Zone Diameter (mm)			
	Staphylococcus aureus	Enterococcus faecalis	Enterobacter cloacae	Escherichia coli
0	0	0	0	0
3	0	16	18	18
6	17	19	19	20
9	18	20	22	22
12	18	22	24	24

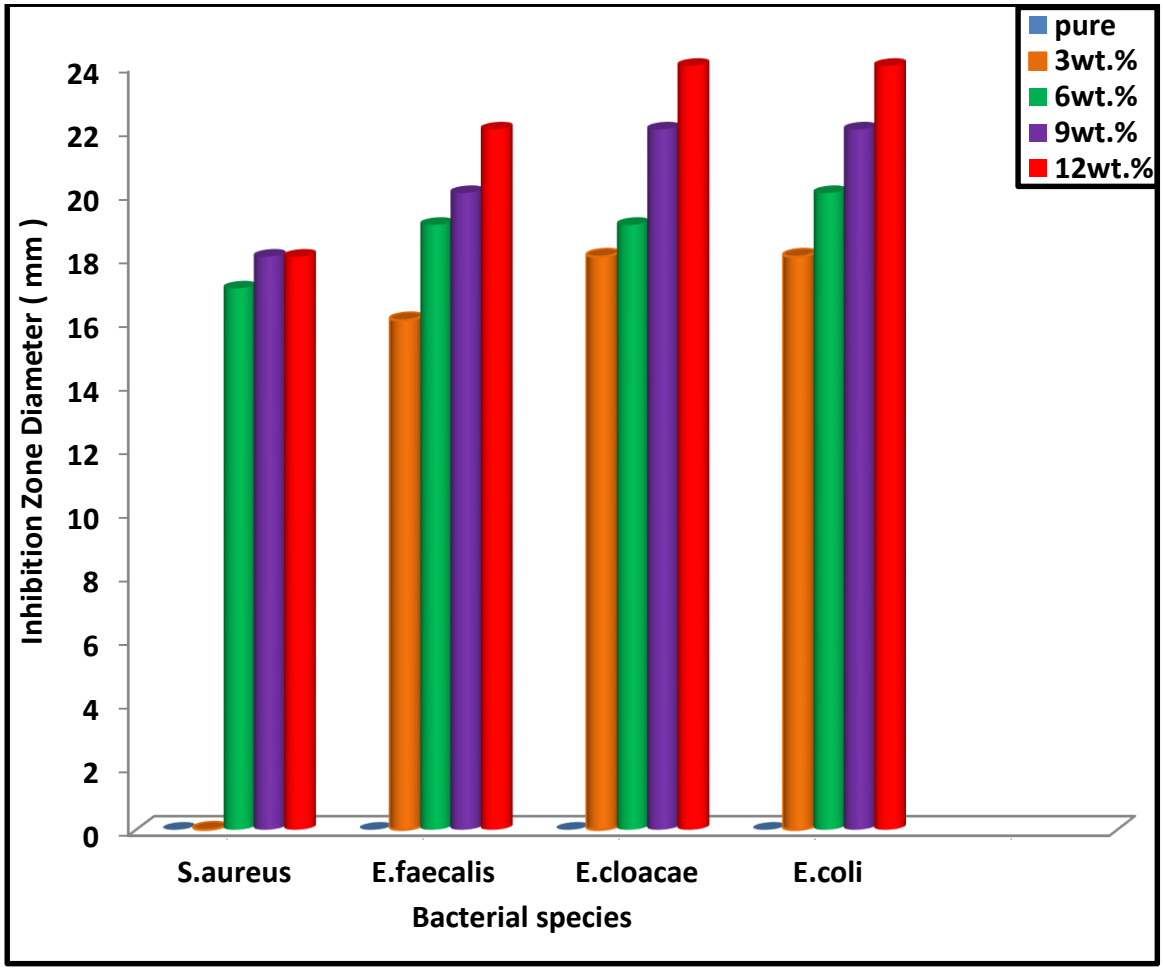

Figure (4.36): Diagram for the antibacterial activity.

4.7 Conclusions

After preparing (PS:PMMA) poly blend and (PS:PMMA)/$BaTiO_3$ nanocomposite blend by solution casting technique and make measurements and depending on the results presented in this work, we can conclude that:

1. The distribution of $BaTiO_3$ nanoparticles additives are improved at (9,12) wt.% weight ratios by form path network inside the (PS:PMMA) poly blend.
2. Increasing the applied field frequency lead to decreasing dielectric constant and dielectric loss for prepared nanocomposite films while A.C electrical conductivity increase considerably. On the other hand, dielectric constant, dielectric loss, and A.C electrical conductivity increase with increasing $BaTiO_3$ nanoparticles weight ratio.
3. The optical parameters increase while transmittance and energy gap decrease with increasing additive weight ratios for (PS:PMMA)/$BaTiO_3$ nanocomposite blends. These nanocomposites have high absorbance in the ultraviolet and visible light regions.
4. For piezoelectric application, the electrical resistance decrease with increasing of $BaTiO_3$ nanoparticles additives weight ratio and applied load for the (PS:PMMA)/$BaTiO_3$ nanocomposite blend. Therefore, these nanocomposites have high sensitivity for mechanical stress.
5. (PS:PMMA)/$BaTiO_3$ nanocomposite blend exhibited higher inhibition zone diameter for gram negative bacteria and lower inhibition zone diameter for gram positive bacteria. Inhibition zone diameter increase with increasing of $BaTiO_3$ nanoparticles additives weight ratio. $BaTiO_3$ nanoparticles was good antimicrobial agent.

4.8 Suggestions for Future Work

Suggestions for work can be outlined through this study and in accordance with the obtained results and conclusions as follows :

1. Studying the influence of $BaTiO_3$ nanoparticles on the mechanical and thermal properties of (PS:PMMA) poly blend and used as pyroelectric materials.
2. Studying the influence of temperature on the dielectric properties of (PS:PMMA)/$BaTiO_3$ nanocomposite blend.
3. Studying the influence of temperature, frequency and relative humidity on the capacitance of (PS:PMMA)/$BaTiO_3$ nanocomposite blend as humidity sensors application.
4. Studying the influence of dye on optical and electrical properties of (PS:PMMA) poly blend and used as smart windows application.

[1]L. Filipponi, and D. S. Sutherland, 2012, "Nanotechnologies: principles, applications, implications and hands-on activities", Luxembourg: Directorate General for Research and Innovation Industrial Technologies (NMP) European Union.

[2]A. Ruhal, J. S. Rana, P. Ruhal, A. Kumar, and M. Ruhil, 2013, "Antimicrobial nanocomposite of silver and gelatin nanofibers for medical applications", International Journal for Technological Research in Engineering, Vol. 1, No. 4, PP. 177-182.

[3]Y. C. Cao, W. Wei, J. Liu, Q. You, F. Liu, Q. Lan, C. Zhang, C. Liu, and J. Zhao, 2015, "The preparation of graphene reinforced poly(vinyl alcohol) antibacterial nanocomposite thin film", International Journal of Polymer Science, Vol. 2015, PP. 1-7.

[4]N. S. Mustafa, M. A. Ali Omer, M. E. M. Garlnabi, and H. A. Ismail, 2016, "Reviewing of general polymer types, properties and application in medical field", International Journal of Science and Research (IJSR), Vol. 5, No. 8, PP. 212-221.

[5]E. S. Guerra, and E. V. Lima, 2013, "Handbook of polymer synthesis, characterization, and processing", John Wiley & Sons, Inc., Hoboken, New Jersey.

[6]S. Tomar, L. Singh, and V. Sharma, 2016, "Miraculous adjuvants: The pharmaceutical polymers", International Research Journal of Pharmacy, Vol. 7, No. 7, PP. 10-18.

[7]M. R. Ahmed, 2016, "Effect of recycling in post-consumer polystyrene cups", Degree Thesis, Plastics Technology, Arcada.

[8]J. Brandrup, E. H. Immergut, and E. A. Grulke, 1975, "Physical constants of polystyrene" and "Physical constants of poly(methyl methacrylate)" and "Solubility parameter values", in Polymer Handbook, 2nd. Edition, John Wiley, New York.

[9]S. Khangkham, 2012, "Catalytic degradation of poly(methyl methacrylate) by zeolite and regeneration of coked zeolite by ozonation", Chemical and Environmental Engineering, Ph.D. Thesis, INP Toulouse, France.

[10]Y. G. SUU, 2008, "Studies on mechanical properties of poly (methyl methacrylate) and poly (methyl methacrylate) - modified natural rubber blend", MSc. Thesis, Semantic Scholar.

[11]C. E. Carraher Jr., 2017, "Introduction to polymer chemistry", 4th. Edition, CRC Press (Taylor & Francis group).

[12]O. Matar, 2017, "Synthesis and characterisation of barium titanate nanoparticles for second harmonic generation applications", Ph.D. Thesis, The University of Leeds.

[13]P. Barik, 2012, "Structure and properties of doped nano barium titanate", Ph.D. Thesis, Visva-Bharati University, India.

[14]F. A. Ismail, R. A. M. Osman, M. S. Idris, S. Taking, and Z. A. Z. Jamal, 2017, "Dielectric and microstructural properties of $BaTiO_3$ and $Ba_{0.9925}Er_{0.0075}TiO_3$ ceramics", The European Physical Journal Conferences, Vol. 162, No. 4.

[15]N. Bouropoulos, G. Psarras, N. G. Moustakas, A. Chrissanthopoulos, and S. Baskoutas, 2008, "Optical and dielectric properties of ZnO-PVA nanocomposites", Physica Status Solidi (A) Applications and Materials, Vol. 205, No. 8, PP. 2033-2037.

[16]K. Vimala, Y. M. Mohan, K. Varaprasad, N. N. Redd, S. Ravindra, N. S. Naidu, and K. M. Raju, 2011, "Fabrication of curcumin encapsulated chitosan-PVA silver nanocomposite films for improved antimicrobial activity", Journal of Biomaterials and Nanobiotechnology (JBNB), Vol. 2, No. 1, PP. 55-64.

[17]J. Q. Qi, T. Peng, Y. M. Hu, L. Sun, Y. Wang, W. P. Chen, L. T. Li, C. W. Nan, and H. L. W. Chan, 2011, "Direct synthesis of ultrafine

tetragonal $BaTiO_3$ nanoparticles at room temperature", Nanoscale Research Letters (a Springer Open Journal), Vol. 6, No. 1.

[18]S. Raja, D. Bheeman, R. Rajamani, S. Pattiyappan, S. Sugamaran, and C. S. Bellan, 2014, "Synthesis, characterization and remedial aspect of $BaTiO_3$ nanoparticles against bacteria", Nanomedicine and Nanobiology, American Scientific Publishers, Vol. 1, No. 2, PP. 1-5.

[19]R. G. Kadhim, 2015, "Study the electrical and structural properties of (PMMA-TiO_2) nanocomposites", Chemistry and Materials Research, Vol. 7, No. 9, PP. 37- 48.

[20]S. S. Kumbhar, M. A. Mahadik, P. K. Chougule, V. S. Mohite, Y. M. Hunge, K. Y. Rajpure, A. V. Moholkar, and C. H. Bhosale, 2015, "Structural and electrical properties of barium titanate ($BaTiO_3$) thin films obtained by spray pyrolysis method", Materials Science, Vol. 33, No. 4, PP. 852-861.

[21]V. N. Reddy, K. C. Babu Naidu, and T. Subbarao, 2016, "Structural, optical and ferroelectric properties of $BaTiO_3$ ceramics", Journal of Ovonic Research, Vol. 12, No. 4, PP. 185-191.

[22]M. Singh, B. C. Yadav, A. Ranjan, M. Kaur, and S. K. Gupta, 2017, "Synthesis and characterization of perovskite barium titanate thin film and its application as LPG sensor", Sensors and Actuators B Chemical, Vol. 241, PP. 1170-1178.

[23]G. G. Carbone, A. Serra, A. Buccolieri, and D. Manno, 2019, "A silver nanoparticle-poly(methyl methacrylate) based colorimetric sensor for the detection of hydrogen peroxide", Heliyon, Vol. 5, No. 11.

[24]D. Hassan, and A. H. Ah-yasari, 2019, "Fabrication and studying the dielectric properties of (polystyrene-copper oxide) nanocomposites for piezoelectric application", Bulletin of Electrical Engineering and Informatics, Vol. 8, No. 1, PP. 52-57.

[25]M. F. H. Al-Kadhemy, R. A. Al-Mousawi, and F. J. Kadhum, 2020, "Effects of adding coumarin dye on physical properties of blend (PC-PS) film", Iraqi Journal of Science, Vol. 61, No. 7, PP. 1633-1644.

[26]A. A. Bani-Salameh, A. A. Ahmad, A. M. Alsaad, I. A. Qattan, and I. A. Aljarrah, 2021, "Synthesis, optical, chemical and thermal characterizations of PMMA-PS/CeO_2 nanoparticles thin film", Polymers, Basel, Vol. 13, No. 7, PP. 1-16.

[27]A. J. Yu, 1971, "The Concept of Compatibility in Poly blends", Platzer; Multicomponent Polymer Systems, Advances in Chemistry; American Chemical Society: Washington, DC.

[28]R. J. Aitken, K. S. Creely, and C. L. Tran, 2004, "Nanoparticles: an occupational hygiene review", HSE Research Report 274, London.

[29]W. S. Khan, N. N. Hamadneh, and W. A. Khan, 2016, "Polymer nanocomposites – synthesis techniques, classification and properties", chapter 4 in Science and applications of Tailored Nanostructures. Semantic Scholar, PP. 50-67.

[30]B. Singh, S. Chauhan, and G. Verma, 2020, "Nanocomposites-a review", Journal of Chemistry and Chemical Sciences, Vol. 5, No. 9, PP. 506-510.

[31]K. Y. Lau, and M. A. M. Piah, 2011, "Polymer nanocomposites in high voltage electrical insulation perspective: a review", Malaysian Polymer Journal, Vol. 6, No. 1, PP. 58-69.

[32]L. M. Manocha, J. Valand, N. Patel, A. Warrier, and S. Manocha, 2006, "Nanocomposites for structural applications", Indian Journal of Pure and Applied Physics, Vol. 44, No. 2, PP. 135-142.

[33]M. B. Ahmad, K. Shameli, W. M. Z. W. Yunus, N. A. Ibrahim, and M. Darroudi, 2010, "Synthesis and characterization of silver/clay/starch bionanocomposites by green method", Australian Journal of Basic and Applied Sciences, Vol. 4, No. 7, PP. 2158-2165.

[34]R. A. Hule, 2007, "Polymer nanocomposites for biomedical applications", MRS Bulletin, Vol. 32, No. 4, PP. 354-358.

[35]C. J. Wu, A. K. Gaharwar, P. J. Schexnailder, and G. Schmidt, 2010, "Development of biomedical polymer-silicate nanocomposites: a materials science perspective", Materials (Basel), Vol. 3, No. 5, PP. 2986-3005.

[36]W. Gacitua, A. Ballerini, and J. Zhang, 2005, "Polymer nanocomposites: synthetic and natural fillers a review", Maderas: Ciencia y Tecnologia, Vol. 7, No. 3, PP. 159-178.

[37]R.V. Kurahatti, A.O. Surendranathan, S. A. Kori, N. Singh, A.V. Ramesh Kumar, and S. Srivastava, 2010, "Defence applications of polymer nanocomposites", Defence Science Journal, Vol. 60, No. 5, PP. 551-563.

[38]D. D. L. Chung, 2002, "Composite materials: functional materials for modern technologies", Springer-Verlag London Ltd, UK.

[39]M. Sen, 2020, "Nanocomposite materials", reviewed chapter, in book: Nanotechnology and the environment, Intech Open Science, London.

[40]L. Dong, 2009, "Dielectric properties of colloidal suspensions", Ph.D. Thesis, Helsinki University of Technology, Espoo, Finland.

[41] Y. N. Aljammal, R. Z. Al-Falih, and Z. B. AL-Dabbagh, 2010, "Study of electrical properties of poly methyl methacrylate (PMMA) under different frequencies and temperatures", Journal of Education and Science, Vol. 23, No. 3, PP. 107-128.

[42]H.N. Chandrakala, R. Bommulu, Shivakumaraiah, J. H. Lee, and S. Hatna, 2013, "Polyvinyl alcohol/carbon coated zinc oxide nanocomposites: Electrical, optical, structural and morphological characteristics", Journal of Alloys and Compounds, Vol. 580, PP. 392-400.

[43]B. K. P. Scaife, 1998, "Principles of dielectrics", Oxford Science Publications, Oxford.

[44]H. Frohlich, 1958, "Theory of dielectrics: Permittivity and dielectric loss", Oxford Science Publications, Oxford.

[45]C. J. F. Bottcher, 1952, "Theory of electric polarization", Elsevier Publishing Company, Amsterdam.

[46]R. J. Botsco, R.W. Cribbs, R. J. King, and R. C. McMaster, 1986, "Microwave methods and applications in nondestructive testing", in Nondestructive Testing Handbook, 2nd. Edition, Vol. 4, American Society Nondestructive Testing.

[47]S. Pal, 2013, "Studies of structural, microstructural and electrical properties of barium titanate modified lead iron niobate", MSc. Thesis, National Institute of Technology, Rourkela.

[48]A.H.M. Areef Billah, 2014, "Investigation of multiferroic and photocatalytic properties of Li doped $BiFeO_3$ nanoparticles prepared by ultrasonication", MSc. Thesis, Bangladesh University of Engineering and Technology, Department of Physics, Dhaka, Bangladesh.

[49]S. Kumar, 2010, "Infrared spectroscopy: method development and ligand binding studies", Licentiate thesis, Stockholm University, Stockholm, Sweden.

[50]A. B. D. Nandiyanto, R. Oktiani, and R. Ragadhita, 2019, "How to read and interpret FTIR spectroscope of organic material", Indonesian Journal of Science & Technology, Vol. 4, No. 1, PP. 97-118.

[51]B. C. Smith, 2011, "Fundamentals of Fourier transform infrared spectroscopy", 2nd. Edition, CRC press (Taylor & Francis group).

[52]F. J. M. Stehr, 2017, "Fourier transform infrared spectroscopy (FTIR) for detection and quantification of milk components for cattle health monitoring", M.Sc. Thesis, Norwegian University of Life Sciences.

[53]G. Husnain, and M. Madhuku, 2017, "Metal ions implantation-induced effects in GaN thin films", Chapter 2 from the book Ion Implantation-Research and Application, Published by INTECH (open science/open minds).

[54]R. Das, Md. E. Ali, and S. B. A. Hamid, 2014, "Current applications of X-ray powder diffraction- a review", Reviews on Advanced Materials Science, Vol. 38, No. 2, PP. 95-109.

[55]B. Sannakki, and A. Gandhe, 2013, "Dielectric properties of PMMA and its composites with ZrO_2", Physics Procedia, Vol. 49, PP. 15-26.

[56]R. P. Suvarna, K . R. Rao, and K. Subbarangaiah, 2002, "A simple technique for a.c. conductivity measurements", Bulletin of Materials Science, Vol. 25, No. 7, PP. 647-651.

[57]A. H. Mohaisen, 2009, "Study of electrical conductivity for amorphous and semi crystalline polymers filled with lithium fluoride additive", MSc. Thesis, AL-Mustansiriya University, College of Science.

[58]J. James, 2019, "Refractive index engineering using polymer nanocomposites", Ph.D. Thesis, University of Southern Brittany (UbS), Lorient, France.

[59]A. M. Diez-Pascual, 2019, "Nanoparticle reinforced polymers", Polymers, Basel, Vol. 11, No. 4.

[60]I. Roppolo, M. Sangermano, and A. Chiolerio, 2016, "Optical properties of polymer nanocomposites", Functional and Physical Properties of Polymer Nanocomposites, Vol. 31, PP. 139-157.

[61]A. Gupta, S. Das, C. J. Neal, and S. Seal, 2016, "Controlling the surface chemistry of cerium oxide nanoparticles for biological applications", Journal of Materials Chemistry B, Vol. 4, PP. 3195-3202.

[62]M. A. Omar, 1975, "Elementary solid state physics: Principles and Applications", 4^{th} Edition, Addison-Wesley Publishing Company, London.

[63]J. A. Dean, 1992, "Lange's handbook of chemistry", 14th Edition, McGraw Hill, Inc., New York.

[64]J. I. Pankove, 1971, "Optical process in semiconductors", Dover Publishing, Inc., New York.

[65]S. Hossain, 2019, "Optical properties of polymers and their applications", MSc. Thesis, New Jersey Institute of Technology.

[66]D. A. Neamen, 1992, "Semiconductor physics and devices Basic Principles", 3rd. Edition, University of New Mexico, Irwin, USA.

[67]D. L. Greenaway, and G. Harbeke, 1966, "Optical Properties and Band Structure of Semiconductors", Pergamon press, New York.

[68]W. Klopffer, 1984, "Introduction to polymer spectroscopy", Springer.

[69]A. J. Kareem, M. A. Habeeb, K. Abd-Ali, 2015, "Effect of adding (PEG-cellulose derivatives) on optical properties of cosmetics face powders", Research & Reviews on Polymer (RRPL), Vol. 6, No. 2, PP. 71-82.

[70]H. N. Najeeb, G. A. Ali, A. K. Kodeary, and J. Ali, 2013, "Doping effect on optical constants of poly-vinyl chloric (PVC)", Academic Research International, Vol. 4, No. 3, PP. 56-62.

[71]T. E. Jenkins, 1995, "Semiconductor science : growth and characterization techniques", Prentice Hall, New York.

[72]J. Ballato, S. Foulger, and D. W. Smith, 2003, "Optical properties of perfluorocyclobutyl polymers", Journal of the Optical Society of America B, Vol. 20, No. 9, PP.1838-1843.

[73]V. M. Radivojevic, S. Rupcic, M. Srnovic, and G. Bensic, 2018, "Measuring the dielectric constant of paper using a parallel plate capacitor", International Journal of Electrical and Computer Engineering Systems, Vol. 9, No. 1. PP. 1-10.

[74]G. I. Torgovnikov, 1993, "Dielectric properties of wood and wood-based materials", 1st. Edition, Springer Series in Wood Science, Verlag, PP. 135-159.

[75]V. S. Sangawar, and M. C. Golchha, 2013, "Evolution of the optical properties of polystyrene thin films filled with zinc oxide nanoparticles", International Journal of Scientific and Engineering Research, Vol. 4, No. 6, PP. 2700-2705.

[76]V. Illingworth, 2000, "The Penguin Dictionary of Physics (Penguin Dictionary)", 3rd. Edition, Longman Group Ltd., P. 3.

[77]J. Mistrik, S. Kasap, H. E. Ruda, C. Koughia, and J. Singh, 2017, "Chapter 3: Optical properties of electronic materials: fundamentals and characterization", Springer Handbook of Electronic and Photonic Materials.

[78]R. M. Abdullah, S. B. Aziz, S. M. Mamand, A. Q. Hassan, S. A. Hussein, and M. F. Z. Kadir, 2019, "Reducing the crystallite size of spherulites in PEO-based polymer nanocomposites mediated by carbon nanodots and Ag nanoparticles", Nanomaterials, Vol. 9, No. 6.

[79]G. K. M. Thutupalli, and S. G. Tomlin, 1976, "The optical properties of thin films of cadmium and zinc selenides and tellurides", IOP Science, Journal of Physics D: Applied Physics, Vol. 9, No. 11, PP. 1639-1646.

[80]S. B. Aziz, 2017, "Morphological and optical characteristics of chitosan (1-x): Cuox ($4 \leq x \leq 12$) based polymer nanocomposites: optical dielectric loss as an alternative method for Tauc's model", Nanomaterials, Basel, Vol. 7, No. 12.

[81]S. B. Aziz, R. B. Marif, M.A. Brza, A. N. Hassan, H. A. Ahmad, Y. A. Faidhalla, and M. F. Z. Kadir, 2019, "Structural, thermal, morphological and optical properties of PEO filled with biosynthesized Ag nanoparticles: new insights to band gap study", Results in Physics, Vol. 13.

[82]D. S. Muhammed, M. A. Brza, M. M. Nofal, S. B. Aziz, S. A. Hussen, and R. T. Abdulwahid, 2020, "Optical dielectric loss as a novel approach to specify the types of electron transition: XRD and UV-Vis as a nondestructive techniques for structural and optical characterization of PEO based nanocomposites", Materials, Vol. 13, No. 13.

[83]S. B. Aziz, M. A. Brza, M. M. Nofal, R. T. Abdulwahid, S. A. Hussen, A. M. Hussein, and W. O. Karim, 2020, "A comprehensive review on optical properties of polymer electrolytes and composites", Materials, Basel, Switzerland, Vol. 13, No. 17.

[84]T. C. Sabari Girisun, and S. Dhanuskodi, 2009, "Linear and nonlinear optical properties of tris thiourea zinc sulphate single crystals", Crystal Research and Technology, Vol. 44, No. 12, PP. 1297-1302.

[85]D. Vatansever, E. Siores, and T. Shah, 2012, "Chapter 10: Alternative resources for renewable energy: piezoelectric and photovoltaic smart structures", Global Warming - Impacts and Future Perspective, 263-290.

[86]M. C. Glasser, P. Li, J. Ryu, and S. Hong, 2018, "Chapter 7: Piezoelectric materials for medical applications", Piezoelectricity - Organic and Inorganic Materials and Applications, PP. 125-145.

[87]M. Pohanka, 2017, "The piezoelectric biosensors: principles and applications, a review", International Journal of Electrochemical Science, Vol. 12, No. 1, PP. 496-506.

[88]M. L. K. Sienkiewicz, 2016, "Concept, implementation and analysis of the piezoelectric resonant sensor/ actuator for measuring the aging process of human skin", Ph.D. Thesis, Toulouse University, France.

[89]C. Covaci, and A. Gontean, 2020, "Piezoelectric energy harvesting solutions: a review", Sensors, Vol. 20, No. 12, PP. 1-37.

[90]M. G. Jimenez, 2018, "Ultrasonic pulse generation by a piezoelectric transducer at cryogenic temperatures", B.Sc. Thesis, Politecnica University, Catalunya.

[91]V. Rathod, S. Janotkar, N. Daundkar, A. Mahajan, and A. Chaple, 2018, "Power generation using piezoelectric material", International Research Journal of Engineering and Technology (IRJET), Vol. 5, No. 2, PP. 87-90.

[92]J. M. Minnerath, J. M. Roland, L. C. Rossi, S. R. Weishalla, and M. M. Wolf, 2009, "A comparison of heat versus methanol fixation for gram staining bacteria", Bioscene, Vol. 35, No. 2, PP. 36-41.

[93]E. Schaechter, 2014, "The gram stain: its persistence and its quirks" in Small Things Considered, American Society For Microbiology.

[94]N. Pukhrambam, 2019, "Comparison of original gram stain and its modification in the gingival plaque samples", Journal of Bacteriology & Mycology: Open Access, Vol. 7, No. 1, PP. 1-3.

[95]K. C. Huang, R. Mukhopadhyay, B. Wen, Z. Gitai, and N. S. Wingreen, 2008, "Cell shape and cell wall organization in gram negative bacteria", The National Academy of Sciences of the USA, Vol. 105, No. 49, PP. 19282–19287.

[96]S. Berezin, Y. Aviv, H. Aviv, E. Goldberg, and Y. R. Tischler, 2017, "Replacing a century old technique- modern spectroscopy can supplant gram staining", Scientific Reports, Springer, Vol. 7.

[97]M. Shahriar, and M. F. Kadir, 2013, "Effect of proteinase - k on DNA extraction from gram positive strains", in book, LAMBERT Academic Publishing (LAP).

[98]S. S. Gabriela, F. R. Daniela, and B. T. Helia, 2016, "Copper nanoparticles as potential antimicrobial agent in disinfecting root canals. Asystematic review", International Journal of Odontostomatology, Vol. 10, No. 3, PP. 547-554.

[99]D. Adamovic, B. Ristic, and F. Zivic, 2018, "Review of existing biomaterials-method of material selection for specific applications in

orthopedics", Biomaterials in Clinical Practice, Springer, Cham, PP. 47-99.

[100]L. Wang, C. Hu, and L. Shao, 2017, "The antimicrobial activity of nanoparticles: present situation and prospects for the future", International Journal of Nanomedicine, Dove press, Vol. 12, PP. 1227-1249.

[101]G. Jian, Y. Jiao, Q. Meng, Z. Wei, J. Zhang, C. Yan, K. Sik Moon, and C. Ping Wong, 2020, "Enhanced dielectric constant and energy density in a $BaTiO_3$/polymer-matrix composite sponge", Communications Materials, Vol. 1, No. 91.

[102]J. Y. Han, and C. W. Bark, 2015, "Tunable band gap of iron-doped lanthanum-modified bismuth titanate synthesized by the thermal decomposition of a secondary phase", Journal of the Korean Physical Society, Vol. 66, No. 9.

[103]Z. F. Li, 2010, "Synthesis and characterization of conducting polymer nanostructures and their application in sensors", Ph.D. Thesis, Missouri University of Science and Technology.

[104]W. Liu, Z. Xie, Y. Lu, M. Gao, W. Zhang, and L. Gao, 2019, "Fabrication and excellent electroresponsive properties of ideal PMMA@$BaTiO_3$ composite particles", Journal The Royal Society of Chemistry Advances, Vol. 9, No. 22, PP. 12404-12414.

[105]G. Vijayakumari, N. Selvakumar, K. Jeyasubramanian, and R. Mala, 2013, "Investigation on the electrical properties of polymer metal nanocomposites for physiological sensing applications", Physics Procedia, Vol. 49, PP. 67-78.

[106]C. Y. Abasi, D. Wankasi, and E. D. Dikio, 2018, "Adsorption study of lead(II) ions on poly(methyl methacrylate) waste material", Asian Journal of Chemistry, Vol. 30, No. 4, PP. 859-867.

[107]A. J. Abed AL-Jabar, M. A. Ahmed Al-dujaili, and I. A. Disher, 2017, "Preparation of barium titanates with different particle size distribution using modified pechini method", Journal of Babylon University, Engineering Sciences, Vol. 25, No. 1.

[108]E.M. Abdelrazek, A.M. Hezma, A. El-khodary, and A.M. Elzayat, 2016, "Spectroscopic studies and thermal properties of PCL/PMMA biopolymer blend", Egyptian Journal of Basic and Applied Sciences, Vol. 3, No. 1, PP. 10-15.

[109]L. Ding, Q. Xin, X. Zhou, J. Qiao, H. Li, and H. Wang, 2013, "Electrochemical behavior of nanostructured nickel phthalocyanine (NiPc/C) for oxygen reduction reaction in alkaline media", Journal of Applied Electrochemistry, Vol. 43, No. 1, PP.43-51.

[110]A. D. Bhagwat, S. S. Sawant, and C. M. Mahajan, 2016, "Facile Rapid Synthesis of Polyaniline (PANI) Nanofibers", Journal of Nano– and Electronic physics , Vol. 8, No. 1.

[111]W. Cai, T. Rao, A. Wang, J. Hu, J. Wang, J. Zhong, and W. Xiang, 2015, "A simple and controllable hydrothermal route for the synthesis of monodispersed cube-like barium titanate nanocrystals", Ceramics International, Vol. 41, No. 3, PP. 4514-4522.

[112]Y.T. Ravikiran, M.T. Lagare, M. Sairam, N.N. Mallikarjuna, B. Sreedhar, S. Manohar, A.G. MacDiarmid, and T.M. Aminabhavi, 2006, "Synthesis, characterization and low frequency AC conduction of polyaniline/niobium pentoxide composites", Synthetic Metals, Vol. 156, No. (16-17), PP. 1139-1147.

[113]N. J. Pinto, A. A. Acosta, G. P. Sinha, and F. M. Aliev, 2000, "Dielectric permittivity study on weakly doped conducting polymers based on polyaniline and its derivatives", Synthetic Metals, Vol. 113, No. (1-2), PP. 77-81.

[114]B. Hussein, 2011, "The D.C and A.C electrical properties of (PMMA-Al_2O_3) composites", European Journal of Scientific Research, Vol. 52, No. 2, PP. 236-242.

[115]D. Hassan, and A. H. Ah-yasari, 2019, "Fabrication and studying the dielectric properties of (polystyrene-copper oxide) nanocomposites for piezoelectric application", Bulletin of Electrical Engineering and Informatics, Vol. 8, No. 1, PP. 52-57.

[116]A. Hashim, M. A. Habeeb**,** and Q. M. Jebur, 2019, "Structural, dielectric and optical properties for (polyvinyl alcohol-polyethylene oxide-manganese oxide) nanocomposites", Egyptian Journal of Chemistry, Vol. 62, Special Issue (Part 2), PP. 735-749.

[117]R. G. Kadhim , M. A. Habeeb, and Q. M. Jebur, 2017, "Dielectric and optical properties for (poly vinyl alcohol-carboxymethyl cellulose-copper oxide) nanocomposites and their applications", Journal of Chemical and Pharmaceutical Sciences, Vol. 10, No.1, PP. 732-739.

[118]M. A. Habeeb, 2013, "Effect of nanosilver particles on thermal and dielectric properties of (PVA-PVP) films", International Journal of Applied and Natural Sciences (IJANS), Vol. 2, No. 4, PP. 103-108.

[119]B. A. Abu Saleh, Y. Ramadin, A. M. Zihlif, and Z. M. Elimat, 2016, "Optical and electrical properties of polystyrene composites containing ultrafine iron particles", Journal of Thermoplastic Composite Materials, Vol. 29, No. 2, PP. 204-218.

[120]S. G. Rathod, R. F. Bhajantri, V. Ravindrachary, T. Sheela, P. K. Pujari, J. Naik, and B. Poojary, 2015, "Pressure sensitive dielectric properties of TiO_2 doped PVA/CN-Li nanocomposite", Journal of Polymer Research, Springer, Vol. 22, No. 2, PP. 1-14.

[121]S.A. Zavyalov, A.N. Pivkina, and J. Schoonman, 2002, "Formation and characterization of metal-polymer nanostructured composites", Solid State Ionics, Vol. 147, No. (3-4), PP.415-419.

[122]G. Schmidt, and M. M. Malwitz, 2003, "Properties of polymer-nanoparticle composites", Current Opinion in Colloid and Interface Science, Vol. 8, PP. 103-108.

[123]H. M. Zidan, A. Tawansi, and M. Abu-Elnader, 2003, "Miscibility, optical and dielectric properties of UV-irradiated poly(vinyl acetate)/ poly(methyl methacrylate) blends", Physica B, Vol. 339, No. 2-3, PP. 78-86.

[124]M. Abdelaziz, 2012, "Optical and dielectric properties of poly(vinyl acetate)/ lead oxide composites", Journal of Materials Science: Materials in Electronics, Vol. 23, No. 7, PP. 1378-1386.

[125]E. M. Abdelrazek, and I. S. Elashmawi, 2008, "Characterization and physical properties of $CoCl_2$ filled polyethyl-methacrylate films", Polymer Composites, Vol. 29, No. 9, PP. 1036-1043.

[126]A. Wasan, T. Mohammed, and K. Tagreed, 2011, "The MR affect on optical properties for poly (vinyl alcohol) films", Journal of Baghdad for Science, Vol. 8, PP. 543-550.

[127]H. H. A. B. Al-Shammari, 2011, "Preparation of polymer composites ((PVA-ZnO), (PVA-$CuSO_{4.5}H_2O$)) and studying some of its electrical and optical properties", M.S. thesis, University of Babylon.

[128]P. U. Asogwa, 2011, "Band gap shift and optical characterization of PVA-capped PbO thin films: effect of thermal annealing", Chalcogenide Letters, Vol. 8, No. 3, PP. 163-170.

[129]H. Hakim, N. H. Al- Garah, and A. Hashim, 2015, "The Effect of Aluminum Oxide Nanoparticles on Optical Properties of (Polyvinyl alcohol-Polyethylene glycol) Blend", Journal of Industrial Engineering Research, Vol. 1, No. 4, PP. 94-98.

[130]T. S. Soliman, and S. A. Vshivkov, 2019, "Effect of Fe nanoparticles on the structure and optical properties of polyvinyl alcohol nanocomposite films", Journal of Non-Crystalline Solids, Vol. 519.

[131]F. A. Mustafa, 2013, "Optical properties of NaI doped polyvinyl alcohol films", Physical Sciences Research International, Vol. 1, No. 1. PP. 1-9.

[132]M. Dahshan, 2002, "Introduction to material science and engineering", 2nd. Edition.

[133]A. H. Ahmad, A. M. Awatif, and N. Zeid Abdul-Majied, 2007, "Doping effect on optical constants of poly methyl methacrylate (PMMA)", The Journal of Engineering Technology, Vol. 25, PP. 558-568.

[134]E. F. Reisa , A. P. Lagea , R. C. Leitea , L. G. Heneineb , W. L. Vasconcelosc , and Z. I. P. Lobatoa, 2006, "Synthesis and characterization of poly (vinyl alcohol) hydrogels and hybrids for rMPB70 protein adsorption", Journal of Materials Research, Vol. 9, No. 2.

[135]S.B. Aziz, H.M. Ahmed, A.M. Hussein, A.B. Fathulla, R.M. Wsw, and R.T. Hussein, 2015, "Tuning the absorption of ultraviolet spectra and optical parameters of aluminum doped PVA based solid polymer composites", Journal of Materials Science: Materials in Electronics, Vol. 26, PP. 8022-8028.

[136]S. B. Aziz, S. Hussein, A. M. Hussein, and S. R. Saeed, 2013, "Optical characteristics of polystyrene based solid polymer composites: effect of metallic copper powder", International Journal of Metals, Vol. 2013, No. 4.

[137]A. Hashim, M. A. Habeeb, A. Hadi, Q. M. Jebur, and W. Hadi, 2017, "Fabrication of novel (PVA-PEG-CMC-Fe_3O_4) magnetic nanocomposites for piezoelectric applications", Sensor Letters, Vol. 15, No. 12, PP. 998-1002.

[138]A. Hashim, and A. Hadi, 2017, "Novel lead oxide polymer nanocomposites for nuclear radiation shielding applications", Ukrainian Journal of Physics, Vol. 62, No. 11.

[139]A. Hashim, and A. Hadi, 2018, "Structural, electrical and optical properties of (biopolymer blend/ titanium carbide) nanocomposites for low cost humidity sensors", Journal of Materials Science: Materials in Electronics, Vol. 29, PP. 11598-11604.

[140]A. Hashim, and A. Hadi, 2018, "Synthesis of novel (polymer blend-ceramics) nanocomposites: structural, optical and electrical properties for humidity sensors", Journal of Inorganic and Organometallic Polymers and Materials, Vol. 28, No. 4.

[141]A. Hashim, and A. Jassim, 2017, "Novel of (PVA-ST-PbO_2) bio nanocomposites: Preparation and properties for humidity sensors and radiation shielding applications", Sensor Letters, Vol. 15, No. 12.

[142]C. Pecharroman, and F. J. Gordillo-vazquez, 2003, "Optical properties of binary composite materials with two nonlinear components", Journal of Modern Optics, Vol. 50, No. 12, PP. 1857-1871.

[143]F. H. Abd El-kader, N. A. Hakeem, I. S. Elashmawi, and A. M. Ismail, 2013, "Structural, optical and thermal characterization of ZnO nanoparticles doped in PEO/PVA blend films", Australian Journal of Basic and Applied Sciences, Vol. 7, No. 10, PP. 608-619.

[144]N. Kumar, A. Kaushal, C. Bhardwaj, and D. Kaur, 2010, "Effect of La doping on structural, optical and magnetic properties of $BiFeO_3$ thin films deposited by pulsed laser deposition technique", Optoelectronics and Advanced Materials-Rapid Communications, Vol. 4, No. 10, PP. 1497-1502.

[145]M. Zhang, Y. Gao, Y. Zhan, X. Ding, M. Wang, and X. Wang, 2018, "Preparing the degradable, flame-retardant and low dielectric constant nanocomposites for flexible and miniaturized electronics with

poly(lactic acid), nano ZIF-8@GO and resorcinol di(phenyl phosphate)", Materials, Vol. 11, No. 9.

[146]F. L. Rashid, A. Hadi, N. H. Al-Garah, and A. Hashim, 2018, "Novel phase change materials, MgO nanoparticles, and water based nanofluids for thermal energy storage and biomedical applications", International Journal of Pharmaceutical and Phytopharmacological Research, Vol. 8, No. 1.

[147]R. Ambrosio, A. Carrillo, M. L. Mota, K. Torre, R. Torrealba, M. Moreno, H. Vazquez, J. Flores, and I. Vivaldo, 2018, "Polymeric nanocomposites membranes with high permittivity based on PVA - ZnO nanoparticles for potential applications in flexible electronics", Polymers, Vol. 10, No. 12.

[148]M. G. Kang, W. S. Jung, C. Y. Kang, and S. J. Yoon, 2016, "Recent progress on PZT based piezoelectric energy harvesting technologies", Journal of Actuators, Vol. 5, No. 5, PP. 1-17.

[149]S. Paria, S. K. Karan, R. Bera, A. K. Das, A. Maitra, and B. B. Khatua, 2016, "A facile approach to develop highly stretchable PVC/$ZnSnO_3$ piezoelectric nanogenerator with high output power generation for powering portable electronic devices", Industrial and Engineering Chemistry Research, Vol. 55, No. 40, PP. 10671-10680.

[150]N. Sanguanwong, 2012, "Effects of titanium dioxide on properties of polyvinyl alcohol with and without surfactant", M.Sc. Thesis, Silpakorn University, Department of Chemical Engineering.

[151]J. R. Morones, J. L. Elechiguerra, A. Camacho, K. Holt, J. B. Kouri, J. T. Ramirez, and M. J. Yacaman, 2005, "The bactericidal effect of silver nanoparticles", Nanotechnology, Vol. 16, No. 10, PP. 2346-2353.

[152]O. Choi, K. K. Deng, N. J. Kim, L. Ross Jr., R. Y. Surampalli, and Z. Hu, 2008, "The inhibitory effects of silver nanoparticles, silver ions,

and silver chloride colloids on microbial growth", Water Research, Vol. 42, No. 12, PP. 3066–3074.

[153]T. Hamouda, A. Myc, B. Donovan, A. Y. Shih, J. D. Reuter, and J. R. Baker Jr., 2000, "A novel surfactant nanoemulsion with a unique non-irritant topical antimicrobial activity against bacteria, enveloped viruses and fungi", Microbiological Research, Vol. 156, No. 1, PP. 1-7.

[154]I. Sondi, B. Salopek-Sondi, S. D. Skapin, S. Segota, I. Jurina, and B. Vukelic, 2011, "Colloid-chemical processes in the growth and design of the bio-inorganic aragonite structure in the scleractinian coral cladocora caespitosa", Journal of Colloid and Interface Science, Vol. 354, No. 1, PP. 181-189.

[155]P. Dibrov, J. Dzioba, K. K. Gosink, and C. C. Hase, 2002, "Chemiosmotic mechanism of antimicrobial activity of Ag^{+} in vibrio cholera", Antimicrobial Agents and Chemotherapy, Vol. 46, No. 8, PP. 2668-2670.

[156]G. Franci, A. Falanga, S. Galdiero, L. Palomba, M. Rai, G. Morelli, and M. Galdiero, 2015, "Silver nanoparticles as potential antibacterial agents", Molecules, Vol. 20, No. 5, PP. 8856-8874.

[157]M. A. Sani, H. Hamishehkar, A. Khezerlou, M. Maleki, M. A. Lalabadi, V. Bagheri, P. Safaei, T. Azimi, M. Hashemi, and A. Ehsani, 2020, "Kinetics analysis and susceptibility coefficient of the pathogenic bacteria by titanium dioxide and zinc oxide nanoparticles", Advanced Pharmaceutical Bulletin, Vol. 10, No. 1, PP. 56-64.

[158]P. P. Mahamuni, P. M. Patil, M. J. Dhanavade, M. V. Badiger, P. G. Shadija, A. C. Lokhande, and R. A. Bohara, 2019, "Synthesis and characterization of zinc oxide nanoparticles by using polyol chemistry for their antimicrobial and antibiofilm activity", Biochemistry and Biophysics Reports, Vol. 17, PP. 71-80.

[159]H. Zhang, X. Lv, Y. Li, Y. Wang, and J. Li, 2009, "P25-graphene composite as a high performance photocatalyst", ACS Nano, Vol. 4, No. 1, PP. 380-386.

[160]K. R. Raghupathi, R. T. Koodali, and A. C. Manna, 2011, "Size-dependent bacterial growth inhibition and mechanism of antibacterial activity of zinc oxide nanoparticles", Langmuir, Vol. 27, No. 7, PP. 4020-4028.

[161]C. T. Handoko, A. Huda, M. D. Bustan, B. Yudono, and F. Gulo, 2017, "Green synthesis of silver nanoparticle and its antibacterial activity", RASAYAN J. Chem.(RJC), Vol. 10, No. 4, PP. 1137-1144.

[162]M. A. Awad, W. K. Mekhamer, N. M. Merghani, A. A. Hendi, K. M. O. Ortashi, F. Al-Abbas, and N. E. Eisa, 2015, "Green synthesis, characterization, and antibacterial activity of silver/polystyrene nanocomposite", Journal of Nanomaterials, Vol. 2015, No. 8, PP. 1-6.

[163]S. K. Taha, H. K. Oudah, A. A. Halob, M. K. Khalaf, and S. N. Mazhir, 2018, "Antibacterial activity and mechanism of the silver nanoparticle in gram positive and negative bacteria", Iraqi Journal of Physics, Vol. 16, No. 39, PP. 124-134.